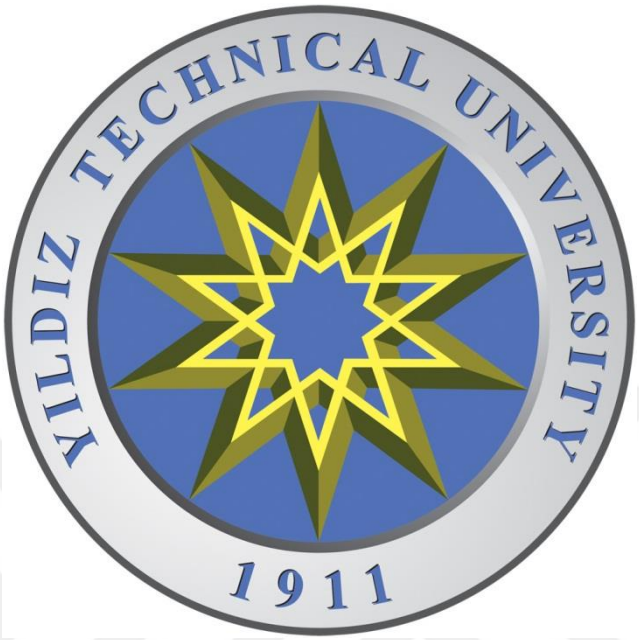

GRADUATE SCHOOL OF NATURAL AND APPLIED SCIENCES

$LiCu_{0.5}Mn_{1.5}O_4$ and $LiNi_{0.25}Cu_{0.25}Mn_{1.5}O_4$ SPINEL ELECTRODES FOR LITHIUM-ION BATTERIES

JULY, 2016

REPUBLIC OF TURKEY
YILDIZ TECHNICAL UNIVERSITY
GRADUATE SCHOOL OF NATURAL AND APPLIED SCIENCES

$LiCu_{0.5}Mn_{1.5}O_4$ and $LiNi_{0.25}Cu_{0.25}Mn_{1.5}O_4$ SPINEL ELECTRODES FOR LITHIUM-ION BATTERIES

ÖZNİL BUDAK

MSc. THESIS
DEPARTMENT OF CHEMICAL ENGINEERING
PROGRAM OF CHEMICAL ENGINEERING

ADVISER
PROF. DR. ZEYNEP SEMA BAYKARA

İSTANBUL - KARLSRUHE, 2016

REPUBLIC OF TURKEY

YILDIZ TECHNICAL UNIVERSITY

GRADUATE SCHOOL OF NATURAL AND APPLIED SCIENCES

$LiCu_{0.5}Mn_{1.5}O_4$ and $LiNi_{0.25}Cu_{0.25}Mn_{1.5}O_4$ SPINEL ELECTRODES FOR LITHIUM-ION BATTERIES

A thesis submitted by Öznil BUDAK in partial fulfilment of the requirements for the degree of **MASTER OF SCIENCE** is approved by the committee on 27.07.2016 in Department of Chemical Engineering, Chemical Engineering Program.

Thesis Adviser

Prof. Dr. Sema Z. BAYKARA

Yıldız Technical University

Approved by the Examining Committee

Prof. Dr. Sema Z. BAYKARA

Yıldız Technical University _____

Prof. Dr. Mahir Arıkol

Boğaziçi University _____

Doç. Dr. Dilek Kılıç Apar

Yıldız Technical University _____

This study was financially supported by BMBF (Federal Ministry of Education and Research) within the DESIREE (Defect spinels as high – energy and high performance materials for electrochemical energy storage) project (Grant No: 03SF0477B).

ACKNOWLEDGEMENTS

The first year of this MSc study was carried out at Yıldız Technical University, which is regarded as one of the leading universities in Turkey, in Chemical Engineering. For that year, I would like to thank my supervisor Prof. Dr. Sema Z. Baykara for giving me a chance to work in the project ´Hydrogen production from H_2S decomposition in micro–structured proton–conducting solid oxide membrane reactors´ which is supported by the Black Sea ERA.NET 2010 Pilot Joint Call (Project No: BS-ERA.NET: 028) acronymed as H_2S-PROTON, TUBITAK-MAG (Project No: 111M801). Her guidance helped me throughout this thesis study.

The second year of this work was carried out at the Institute of Organic Chemistry (Karlsruhe Institute of Technology) and Institute of Applied Materials (IAM) – Energy Storage Systems (ESS). The financial supports for this work by Federal Ministry of Education and Research are gratefully acknowledged. I would like to express my sincere gratitude to Prof. Dr. rer. nat. Helmut Ehrenberg who is the head of IAM – ESS department for giving me the chance to carry out this MSc study in his group. I am always thinking that I was very lucky because I had co – supervisors; Dr. Natalia Bramnik, Dr. Aiswarya Bhaskar and Dr. Nilüfer Kızıltaş-Yavuz all the time with me, who taught me a lot, answered all my questions, guided me perfectly, helped me find a way to go further with my research especially, when I was feeling being stuck at some points and moreover, they are perfect friends.This study has benefitted from beamtime allocation by HASYLAB at PETRA III beamline P02.1 in Hamburg, Material Science and Powder Diffraction (MSPD) beamline at ALBA in Barcelona and XAS beamline at ANKA in Karlsruhe.I wish to thank Dr. Michael Knapp and Dr. Murat Yavuz for providing support and giving useful comments on X – ray diffraction measurements.I would like to thank Dr. Ditty Dixon for XANES measurements, analyses of the data and useful comments. I also wish to thank Dr. Sylvio Indris and Dr. Maximilian Kaus for the NMR measurements. Additionally, I would like to thank Michael Lang and Lukas Pfaffmann for the SEM experiments.All colleagues in IAM – ESS are gratefully acknowledged, especially Geethu Balachandran, Heike Stöffler and Florian Sigel for their friendship and love. With their help, Last but not least, I would like to thank my parents, my sister and my best friend, Sevin Özbek, and whom I missed a lot, for their kind support, love, patience and confidence in me.

July, 2016

Öznil BUDAK

TABLE OF CONTENTS

Page

ACKNOWLEDGEMENTS iv

TABLE OF CONTENTS v

LIST OF SYMBOLS viii

LIST OF ABBREVIATIONS ix

LIST OF FIGURES x

LIST OF TABLES xiii

ABSTRACT xiv

ÖZET xvi

CHAPTER 1

INTRODUCTION AND AIM OF THE WORK 1

CHAPTER 2

FUNDAMENTALS 3

2.1 Overview of Batteries 3
2.2 Significant Descriptions for Batteries 4
2.3 Lithium-ion Batteries (LIBs) 5
2.3.1 Negative Electrodes for LIBs 7
2.3.2 Positive Electrodes for LIBs 8
2.3.3 Electrolytes for LIBs 11
2.3.4 Separators for LIBs 11

CHAPTER 3

EXPERIMENTAL 12

3.1 Synthesis of the Materials 12
3.2 X-Ray Diffraction (XRD) 14
3.3 Inductively Coupled Plasma – Optical Emission Spectroscopy (ICP – OES) . 16
3.4 Scanning Electron Microscopy (SEM) 16
3.5 X-Ray Absorption Spectroscopy (XAS) 16
3.6 Nuclear Magnetic Resonance Spectroscopy (NMR) 17
3.7 Electrochemical Experiments 17
3.7.1 Electrode Preparation 17
3.7.2 Test Cells Preparation 18
3.7.3 Electrochemical Technique 19

CHAPTER 4

RESULTS AND DISCUSSION 21

4.1 $LiCu_{0.5}Mn_{1.5}O_4$ High Voltage Spinel Cathode Material 21
4.1.1 Results of Annealed $LiCu_{0.5}Mn_{1.5}O_4$ in Air Cathode Materials 21
4.1.1.1 The influence of Annealing Time on Structural Characteristic 21
4.1.1.2 Elemental Analysis 23
4.1.1.3 Nuclear Magnetic Resonance (NMR) Spectroscopic Studies of LCuMO Cathode Material 24
4.1.1.4 Morphology Studies on Influence of the Annealing Time 26
4.1.1.5 Cycling Voltammetry 27
4.1.1.6 The Influence of Annealing Time on the Cycling Stability and Electrochemical Characterization 28
4.1.1.7 In Situ Investigations 31
4.1.1.8 The Influence of Annealing Temperature on Structural Characteristic 34
4.1.1.9 The Influences of Annealing Temperature on the Cycling Stability and Electrochemical Characterization 36
4.1.1.10X – Ray Absorption Near Edge Structure (XANES) Analysis of the Annealed LCuMO at Varying Temperature 38
4.1.2 Results of Annealed $LiCu_{0.5}Mn_{1.5}O_4$ under O_2 Cathode Materials 39
4.1.2.1 Structural Characterization 39
4.1.2.2 Electrochemical Characterization 41
4.1.3 Structural Characterization of the $LiCu_{0.5}Mn_{1.5}O_4$ Samples Annealed under Argon 44
4.2 $LiNi_{0.25}Cu_{0.25}Mn_{1.5}O_4$ High Voltage Spinel Cathode Material 45
4.2.1 Results of Annealed $LiNi_{0.25}Cu_{0.25}Mn_{1.5}O_4$ in Air Cathode Materials 45
4.2.1.1 Structural Characterization 45
4.2.1.2 Morphology Studies 47
4.2.1.3 Cycling Voltammetry 48
4.2.1.4 Electrochemical Characterization 49
4.2.2 Results of Annealed $LiNi_{0.25}Cu_{0.25}Mn_{1.5}O_4$ under O_2 Cathode Materials . 52
4.2.2.1 Structural Characterization 52
4.2.2.2 Electrochemical Characterization 54

4.2.3 Structural Characterization Studies on Annealed $LiNi_{0.25}Cu_{0.25}Mn_{1.5}O_4$ under Ar Cathode Materials 57

CHAPTER 5

CONCLUSION 59

REFERENCES 61

CURRICULUM VITAE 64

LIST OF SYMBOLS

a	The ratio of the activities of products and reactants
C – Rate	Charge and discharge rate
d	Spacing between scattering planes in the lattice
E^{o}	The standard cell potential
E	Cell potential (for the Nernst equation)
E^{o}_{anode}	Anode standard electrode potential
E^{o}_{cathode}	Cathode standard electrode potential
F	The Faraday constant
I	The amount of current
M	The molecular weight
N_A	The Avogadro constant
q	Charge
Q	Charge capacity of a cell
$Q_{specific}$	Specific capacity of a cell
$Q_{theoretical}$	The theoretical specific capacity
R	The gas constant
T	Temperature
t	Time
λ	Wavelength of the beam
θ	The angle between incoming beam and the scattering plane of the crystal

LIST OF ABBREVIATIONS

CV	Cycling Voltammetry
ccp	Cubic – close – packed
DMC	Dimethyl Carbonate
EC	Ethylene Carbonate
GCPL	Galvanostatic Cycling
ICP – OES	Inductively Coupled Plasma – Optical Emission Spectroscopy
LCuMO	$LiCu_{0.5}Mn_{1.5}O_4$
LCuMO–600°C–air	$LiCu_{0.5}Mn_{1.5}O_4$ sample annealed at 600 °C for 4 h in air
LCuMO–750°C–air	$LiCu_{0.5}Mn_{1.5}O_4$ sample annealed at 750 °C for 4 h in air
LCuMO–900°C–air	$LiCu_{0.5}Mn_{1.5}O_4$ sample annealed at 900 °C for 4 h in air
LCuMO–600°C–O_2	$LiCu_{0.5}Mn_{1.5}O_4$ sample annealed at 600 °C for 4 h under O_2
LCuMO–750°C–O_2	$LiCu_{0.5}Mn_{1.5}O_4$ sample annealed at 750 °C for 4 h under O_2
LCuMO–900°C–O_2	$LiCu_{0.5}Mn_{1.5}O_4$ sample annealed at 900 °C for 4 h under O_2
LIB	Lithium Ion Battery
LIBs	Lithium-ion Batteries
LNCuMO	$LiNi_{0.25}Cu_{0.25}Mn_{1.5}O_4$
LNCuMO–600°C–air	$LiNi_{0.25}Cu_{0.25}Mn_{1.5}O_4$ sample annealed at 600 °C for 4 h in air
LNCuMO–750°C–air	$LiNi_{0.25}Cu_{0.25}Mn_{1.5}O_4$ sample annealed at 750 °C for 4 h in air
LNCuMO–900°C–air	$LiNi_{0.25}Cu_{0.25}Mn_{1.5}O_4$ sample annealed at 900 °C for 4 h in air
LNCuMO–600°C–O_2	$LiNi_{0.25}Cu_{0.25}Mn_{1.5}O_4$ sample annealed at 600 °C for 4 h under O_2
LNCuMO–750°C–O_2	$LiNi_{0.25}Cu_{0.25}Mn_{1.5}O_4$ sample annealed at 750 °C for 4 h under O_2
LNCuMO–900°C–O_2	$LiNi_{0.25}Cu_{0.25}Mn_{1.5}O_4$ sample annealed at 900 °C for 4 h under O_2
LNMO	$LiNi_{0.5}Mn_{1.5}O_4$
MAS NMR	Magic Angle Spinning Nuclear Magnetic Resonance
MSPD	Materials Science of Powder Diffraction Beamline
NiMH	Nickel Metal Hydride
NMP	N-methyl-2-pyrorolidone
NMR	Nuclear Magnetic Resonance
PE	Polyethylene
PP	Polypropylene
PVdF	Polyvinylidenefluoride
RF	Radiofrequency
SEM	Scanning Electron Microscopy
S.G.	Space group
XANES	X – Ray Absorption Near Edge Structure
XAS	X-Ray Absorption Spectroscopy
XRD	X – Ray Diffraction

LIST OF FIGURES

Page

Figure 1.1 Structure of $LiCu_{0.5}Mn_{1.5}O_4$ (*Fd3m*) 2
Figure 2.1 Schematic representation of movement of electrons and lithium ions during a) charging and b) discharging in a lithium ion cell [1] 6
Figure 2.2 Electrochemical characteristics and simplified crystal structures of LIB cathode material [7] 8
Figure 2.3 Section from the Li – Mn – O phase diagram at room temperature [11] 9
Figure 3.1 (a) Reaction scheme of the Pechini sol-gel process [21] and (b) complied photographs from the synthesis of $LiCu_{0.5}Mn_{1.5}O_4$ 13
Figure 3.2 Overview of X-ray diffraction experiment setup at ALBA 15
Figure 3.3 Parts of *in situ* coin cell 15
Figure 3.4 Overview of coated materials on the alumina foil (a), coating machine (b), pressing step (c) and the electrodes obtained after pressing with 8 tons/cm^2 (d) 18
Figure 3.5 Schematic drawing of CR2032 type half test cell 19
Figure 3.6 Overview of the potentiostat setup 19
Figure 4.1 Rietveld refinement of diffraction patterns of LCuMO annealed at 600^oC in air of as prepared a) 4 h b) 12 h c) 24 h materials measured in 0.5 mm capillaries 22
Figure 4.2 ^{63}Cu MAS NMR spectra of the LCuMO annealed at 600^oC for 4 h in air 24
Figure 4.3 ^7Li MAS NMR spectra of $LiMn_2O_4$ and the cathode material LCuMO annealed at 600^oC for 4 h in air 25
Figure 4.4 ^7Li MAS NMR spectra of the cathode material LCuMO annealed at 600^oC 4 h in air with fit peaks 26
Figure 4.5 SEM images of a) LCuMO – precursor, b) the LCuMO annealed at 600^oC 4 h in air, c) the LCuMO annealed at 600^oC 12 h in air, d) the LCuMO annealed at 600^oC 24 h in air 27
Figure 4.6 The Cycling voltammogram of 1st and 5th cycles of the cathode materials LCuMO annealed at 600 ^oC for 4 h at a scan rate of 0.15 mV s^{-1} in a voltage range 3 – 5.3 V 28
Figure 4.7 Cell potential vs. specific discharge capacity curves of 1st discharge of the cathode materials LCuMO annealed at 600 ^oC in air for 4 h (black), 12 h (red) and 24 h (blue) 29
Figure 4.8 Cell voltage vs. Li content in the material curves of 1st cycle of the cathode materials LCuMO annealed at 600 ^oC in air of as prepared a) 4 h, b) 12 h and c) 24 h 30
Figure 4.9 Specific discharge capacity vs. cycle number plots of the cathode materials LCuMO annealed at 600 ^oC in air for 4, 12 and 24 h 31

Figure 4.10 Voltage profile corresponding to the in situ synchrotron diffraction patterns for the cathode material LCuMO annealed at 600 ^{o}C for 4 h in air 2 – 5 V cycled at C/5 charge – discharge rate 32
Figure 4.11 Selected 2θ regions of in situ synchrotron diffraction patterns of the cathode material LCuMO annealed at 600 ^{o}C for 4h in air..... 33
Figure 4.12 a) Cell parameters of the cubic spinel system vs. Li content in the cathode material LCuMO annealed at 600 ^{o}C 4 h in air, b) Cell potential vs. Li content in the cathode material cycled at the charge – discharge rate of C / 5 in a voltage range 2 – 5 V..... 34
Figure 4.13 Rietveld refinement of diffraction patterns of as prepared a) LCuMO–600°C–air, b) LCuMO–750°C–air and c) LCuMO–900°C–air samples measured in 0.5 mm capillaries 35
Figure 4.14 Cell potential vs. specific discharge capacity of 1st discharge of cathode materials LCuMO–600°C–air, LCuMO–750°C–air and LCuMO–900°C–air 37
Figure 4.15 a) Specific discharge capacity vs. cycle number plots of cathode materials LCuMO–600°C–air, LCuMO–750°C–air and LCuMO–900°C–air cycled at C/3.5 rate between 3 – 5.1 V, b) Coulombic efficiencies vs. cycle number plots for the cycling mentioned in a)..... 37
Figure 4.16 XANES of Mn K – edge, for LCuMO–600°C–air, LCuMO–750°C–air and LCuMO–900°C–air samples, as well as for the reference material MnO_2 38
Figure 4.17 XANES of Cu K – edge, for LCuMO–600°C–air, LCuMO–750°C–air and LCuMO–900°C–air samples, as well as for the reference materials Cu_2O and CuO..... 39
Figure 4.18 Rietveld refinement of diffraction patterns of as prepared a) LCuMO–600°C–O_2, b) LCuMO–750°C–O_2 and c) LCuMO–900°C–O_2 samples measured in 0.5 mm capillaries 40
Figure 4.19 Cell potential vs. specific discharge capacity of 1st discharge of cathode materials LCuMO–600°C–O_2, LCuMO–750°C–O_2 and LCuMO–900°C–O_2 42
Figure 4.20 Cell voltage vs. Li content in the material curves of 1st cycle of as prepared a) LCuMO–600°C–O_2, b) LCuMO–750°C–O_2 and c) LCuMO–900°C–O_2 43
Figure 4.21 a) Specific discharge capacity vs. cycle number plots of LCuMO–600°C–O_2, LCuMO–750°C–O_2 and LCuMO–900°C–O_2 cathode materials cycled at C/3.5 rate between 3 – 5.1 V, b) Coulombic efficiencies vs. cycle number plots for cycling mentioned in a)..... 43
Figure 4.22 XRD patterns of the LCuMO annealed at 600 ^{o}C, 750 ^{o}C and 900 ^{o}C for 4 h under Argon atmosphere cathode materials 45
Figure 4.23 Rietveld refinement of diffraction patterns of as prepared cathode materials a) LNCuMO–600°C–air, b) LNCuMO–750°C–air and c) LNCuMO–900°C–air measured in 0.5 mm capillaries..... 46
Figure 4.24 SEM images of as prepared a) LNCuMO–precursor, b) LNCuMO–600°C–air and c) LNCuMO–750°C–air powders..... 48
Figure 4.25 Cycling voltammograms of 1st and 5th cycles of cathode material LNCuMO–600°C–air with the scan rate of 0.15 mVs^{-1} in a voltage range 3 – 5.3 V.. 49
Figure 4.26 Cell voltage vs. specific discharge capacity of 1st discharge of cathode materials LNCuMO– 600°C–air, LNCuMO– 750°C–air and LNCuMO–900°C–air 50

Figure 4.27 Cell voltage vs. Li content in the material curves of 1st cycle of as prepared a) LNCuMO–600°C–air, b) LNCuMO–750°C–air and c) LNCuMO–900°C–air 51
Figure 4.28 a) Specific discharge capacity vs. cycle number plots of cathode materials LNCuMO–600°C–air, LNCuMO–750°C–air and LNCuMO–900°C–air cycled at C / 3.5 rate between 3 – 5.1 V, b) Coulombic efficiency vs. cycle number plots for cycling mentioned in a) 52
Figure 4.29 Rietveld refinement of diffraction patterns of as prepared cathode materials a) LNCuMO–600°C–O_2, b) LNCuMO–750°C–O_2 and c) LNCuMO–900°C–O_2 measured in 0.5 mm capillaries 53
Figure 4.30 Cell voltage vs. specific discharge capacity of 1st discharge of cathode materials LNCuMO–600°C–O_2, LNCuMO–600°C–O_2 and LNCuMO–600°C–O_2 55
Figure 4.31 Cell voltage vs. Li content in the material curves of 1st cycle of as prepared a) LNCuMO–600°C–O_2, b) LNCuMO–750°C–O_2 and c) LNCuMO–900°C–O_2 56
Figure 4.32 a) Specific discharge capacity vs. cycle number plots of cathode materials LNCuMO–600°C–O_2, LNCuMO–750°C–O_2 and LNCuMO–900°C–O_2 cycled at C / 3.5 rate between 3 – 5.1 V, b) Coulombic efficiency vs. cycle number plots for cycling mentioned in a) 56
Figure 4.33 XRD patterns of the cathode materials LNCuMO annealed at 600 °C, 750 °C and 900 °C for 4 h under Argon atmosphere 58

LIST OF TABLES

Page

Table 2.1 Advantages and disadvantages of LIBs [3] 7
Table 2.2 Mn valance and crystallographic structures of the spinels on the tie line between $Li_4Mn_5O_{12}$ and $LiMn_2O_4$ [12] 9
Table 4.1 Rietveld refinement results of LCuMO annealed at 600 ^{o}C in air samples 23
Table 4.2 Results of ICP – OES analyses of LCuMO annealed at 600 ^{o}C for 4 h 23
Table 4.3 Rietveld refinement results based on in situ synchrotron diffraction of the LCuMO annealed at 600 ^{o}C for 4 h in air cathode material 33
Table 4.4 Rietveld refinement results of LCuMO–600°C–air, LCuMO–750°C–air and LCuMO–900°C–air samples 36
Table 4.5 Rietveld refinement results of LCuMO–600°C–O_2, LCuMO–750°C– O_2 and LCuMO–900°C–O_2 samples 41
Table 4.6 Rietveld refinement result of the LCuMO annealed at 600 ^{o}C for 4 h under Argon atmosphere cathode material 44
Table 4.7 Rietveld refinement results of LNCuMO–600°C–air, LNCuMO–750°C–air and LNCuMO–900°C–air samples 47
Table 4.8 Rietveld refinement results of LNCuMO–600°C–O_2, LNCuMO–750°C–O_2 and LNCuMO–900°C–O_2 samples 54
Table 4.9 Rietveld refinement result of the LNCuMO annealed at 600 ^{o}C for 4 h under Argon atmosphere cathode material 57

ABSTRACT

$LiCu_{0.5}Mn_{1.5}O_4$ and $LiNi_{0.25}Cu_{0.25}Mn_{1.5}O_4$ SPINEL ELECTRODES for LITHIUM-ION BATTERIES

Öznil BUDAK

Department of Chemical Engineering

MSc. Thesis

Adviser: Prof. Dr. Sema Zeynep BAYKARA

In this study, developing and improving appropriate high voltage spinel $LiCu_{0.5}Mn_{1.5}O_4$ (LCuMO) and $LiNi_{0.25}Cu_{0.25}Mn_{1.5}O_4$ (LNCuMO) cathode materials for Lithium - ion batteries were aimed. These cathode materials were synthesized using a citric acid assisted Pechini sol - gel method. Three different calcination temperatures (600 ^{o}C, 750 ^{o}C and 900 ^{o}C) and atmospheres (air, O_2 and Ar) were used to synthesize the materials. The impact of the annealing time on the LCuMO cathode material prepared at 600 ^{o}C was studied. The structure and morphology of the obtained materials were investigated using X - ray and synchrotron powder diffraction techniques, X- ray Absorption Spectroscopy (XAS), Nuclear Magnetic Resonance (NMR) as well as Scanning Electron Microscopy (SEM). Moreover, electrochemical performance as well as underlying electrochemical mechanism were investigated.

LCuMO and LNCuMO materials have cubic spinel structure with the space group $Fd\bar{3}m$ where part of Cu atoms exist on the 8a tetrahedral sites normally occupied by Li. Depending on synthesis conditions, the samples contain different ratios of CuO and Li_2MnO_3 as impurities. ^{7}Li MAS NMR confirmed the presence of Cu ions in the spinel lattice. The X – ray diffraction revealed that Cu atoms patially fill the 8a tetrahedral sites normally occupied by Li. The results of XANES for the annealed LCuMO in air samples revealed that Cu and Mn in the samples predominantly exist as Cu^{2+} and Mn^{4+}.

Electrochemical characterization was performed in different voltage ranges in the half-cells containing lithium as both counter and reference electrodes. The cyclic voltammetry revealed different oxidation-reduction peaks, which were attributed to the Mn^{3+} / Mn^{4+} (4V region) or the Cu^{2+} / Cu^{3+} or the Ni^{2+} / Ni^{4+} redox couples. Upon galvanostatic

cycling, strong capacity fading was observed. The annealed LCuMO in air samples have better capacity retention after 100 cycles at C / 3.5 (60.3 %) than all the other samples. Moreover, the coulombic efficiency increases with the increasing annealing temperature.

In situ synchrotron diffraction revealed that lithium extraction in the 5 V region proceeds via solid solution mechanism. The insertion of the second Li into $LiCu_{0.5}Mn_{1.5}O_4$ at around 3 V region is associated with two phase reaction for the LCuMO samle annealed at 600 ^{o}C for 4 h in air (from the cubic phase to tetragonal phase).

Key words: Cathode metarials, Lithium - ion batteries, high voltage electrode, $LiCu_{0.5}Mn_{1.5}O_4$ spinel electrode, $LiNi_{0.25}Cu_{0.25}Mn_{1.5}O_4$ spinel electrode

ÖZET

LİTYUM-İYON PİLLERİ için $LiCu_{0.5}Mn_{1.5}O_4$ ve $LiNi_{0.25}Cu_{0.25}Mn_{1.5}O_4$ SPİNEL ELEKTROTLARI

Öznil BUDAK

Kimya Mühendisliği Anabilim Dalı

Yüksek Lisans Tezi

Tez Danışmanı: Prof. Dr. Sema Zeynep BAYKARA

Bu çalışmada, Lityum - iyon pilleri için yüksek voltaj spinel $LiCu_{0.5}Mn_{1.5}O_4$ (LCuMO) ve $LiNi_{0.25}Cu_{0.25}Mn_{1.5}O_4$ (LNCuMO) katot malzemelerinin geliştirilmesi ve iyileştirilmesi amaçlanmıştır. Bu katot malzemeler sitrik asit destekli Pechini sol - jel metodu ile sentezlenmiştir. Malzemelerin sentezi için üç farklı kalsinasyon sıcaklığı (600 $^{\circ}$C, 750 $^{\circ}$C ve 900 $^{\circ}$C) ve atmosferi (hava, O_2 ve Ar) seçilmiştir. Tavlama süresinin 600 $^{\circ}$C´de hazırlanmış LCuMO katot malzemesi üzerindeki tavlama etkisi incelenmiştir. Elde edilen malzemelerin yapıları ve morfolojileri X-ışını ve sinkrotron toz parçacık kırınımı teknikleri, X-ışını absorplama spektroskopisi (XAS), Nükleer Manyetik Rezonans (NMR) yanısıra taramalı elektron mikroskobu (SEM) kullanılarak incelenmiştir. Ayrıca, elektrokimyasal performans ve bu performansın altında yatan elektrokimyasal mekanizma da incelenmiştir.

LCuMO ve LNCuMO malzemeleri, Cu atomlarının bir kısmının, normalde Li tarafından işgal edildiği 8a tetrahedral pozisyonunda da var olabildiği, uzay grubu $Fd\bar{3}m$ ile kübik spinel yapıya sahiptirler. Sentez koşullarına bağlı olarak, örnekler farklı oranlarda CuO ve Li_2MnO_3 kirliliği içermektedir. ^{7}Li MAS NMR, Cu iyonlarının spinel kafes içerisinde olduğunu doğrulamıştır. XRD ile normalde Li tarafından işgal edilen 8a tetrahedral pozisyonunun Cu atomları tarafından da kısmen doldurulduğu tespit edilmiştir. XANES sonuçları, hava ortamında tavlanmış LCuMO örneklerindeki Cu ve Mn´in büyük çoğunlukla Cu^{2+} ve Mn^{4+} olarak var olduğunu ispatlamıştır.

Elektrokimyasal karakterizasyon, farklı voltaj serilerinde lityumun karşıt ve referans elektrot olarak kullanıldığı yarım - hücre pilleri ile yürütülmüştür. Çevrim voltametresi ile farklı yükseltgenme-indirgenme pikleri tespit edilmiş ve bunlar Mn^{3+} / Mn^{4+} (4 V bölgesi), Ni^{2+} / Ni^{4+} ve/veya Cu^{2+} / Cu^{3+} redoks çiftleri ne dayandırılmıştır. Galvanostatik

çevrim ile, güçlü kapasite kaybı tespit edilmiştir. Hava ortamında tavlanmış LCuMO örnekleri diğer örneklere göre, C / 3.5´da 100 çevrimden sonra daha iyi kapasite retansiyonuna (% 60.3) sahiptir. Bununla birlikte, coulomb verimi sıcaklığın artmasıyla birlikte artmaktadır.

In situ sinkrotron kırınımı, 5 V bölgesinde lityum ekstraksiyonunun katı çözelti mekanizması ile devam ettiğini ortaya koymuştur. Hava ortamında 600 ˚C´de 4 saat tavlanmış LCuMO örneği için, 3 V civarındaki $LiCu_{0.5}Mn_{1.5}O_4$ içerisine ikinci lityum eklenmesi iki faz reaksiyonu (kübik fazdan tetragonal faza) ile ilişkilendirilmiştir.

Anahtar Kelimeler: Katot malzemeler, Lityum iyon pilleri, yüksek voltaj elektrot, $LiCu_{0.5}Mn_{1.5}O_4$ spinel elektrot, $LiNi_{0.25}Cu_{0.25}Mn_{1.5}O_4$ spinel elektrot

CHAPTER 1

INTRODUCTION and AIM of the WORK

The world population increases day by day, our energy requirement also increases. Nowadays, fossil fuels are the major energy sources that are being used in the world. However, their over – consumption leads to serious environmental issues such as air pollution, CO_2 emission, acid rain, global warming etc. Therefore, the concerns over the environmental pollution have led to increasing interest in renewable energies such as solar and wind. However, these renewable energy sources are uncontrollable and intermittent, which require reliable electrical or thermal energy storage systems for stable and consistent power delivery. Among electrical energy storage systems, rechargeable batteries are the most promising candidates because of their high energy density and high energy efficiency. The latest and highest performance rechargeable battery system to meet the energy storage requirement is Lithium Ion Battery (LIB), which has been most rapidly developed and widely used in numbers of mobile consumer electronics, such as cellular phones, cameras, laptops, tablets, and power tools, due to their high energy density, high power capacity and performance. While acceptable for the applications in mobile consumer electronics, the relatively high cost and limited earth abundance of the transition metals used in Li content cathode materials become grand challenges for the transportation and stationary applications. In order to overcome the challenges of the performance and cost, new materials and concepts are necessary for the development and commercialization of the next generation rechargeable batteries.

The Lithium-ion Batteries (LIBs) store electrochemical energy through the reversible intercalation and deintercalation of Li^+ ions into/from a transition metal oxide as the cathode material and natural or synthetic graphite as the anode material. In order to improve the performance of LIBs, researches have been focusing on the cathode materials. Mn – based spinel materials which are member of the cathode materials for the

LIBs are potential candidates for high energy density battery applications due to their high operating voltage and relatively high capacity [1].

The substituted manganese spinels $LiM_xMn_{2-x}O_4$ (M = Cr, Fe, Co, Ni, Cu) are attractive candidates for the development of advanced positive electrodes for the LIBs. Among them, $LiNi_{0.5}Mn_{1.5}O_4$ (LNMO) received most attention due to the high operation voltage and high theoretical capacity [1]. In the spinel structure of LNMO (S.G. $Fd\bar{3}m$) the lithium ions are located on the tetrahedral site (8a) and the electrochemically active Ni^{2+} ions occupy the octahedral site (16d) [2]. In contrast to LNMO, $LiCu_{0.5}Mn_{1.5}O_4$ is prone to cation disorder (see Figure 1.1). The presence of transition metals on the tetrahedral site can have a strong impact onto the lithium transport, and, therefore, on the electrochemical performance. The elucidation of the interplay between the cation distribution and the electrochemical performance is, therefore, very important for the development of Cu-based spinel electrode materials.

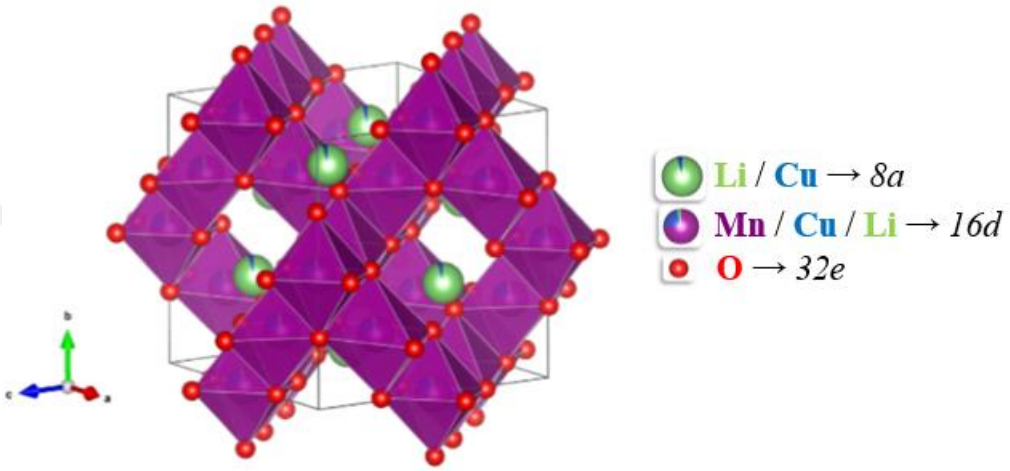

Figure 1.1 Structure of $LiCu_{0.5}Mn_{1.5}O_4$ ($Fd\bar{3}m$)

In this study, a comparative investigation of $LiCu_{0.5}Mn_{1.5}O_4$ and $LiNi_{0.25}Cu_{0.25}Mn_{1.5}O_4$ spinels as cathode materials for LIBs is reported focusing on the structural characterization and correlation of the structural parameters with cycling behaviour.

CHAPTER 2

FUNDAMENTALS

2.1 Overview of Batteries

A battery is a device consisting of one or more electrochemical cells (galvanic cell) for converting the chemical energy into electric energy using electrochemical oxidation – reduction (redox) reactions. An electrochemical cell consists of four main parts: the anode (negative electrode, where the oxidation reactions occur during discharge), the cathode (positive electrode, where the reduction reactions occur during discharge), the electrolyte (ionic conductor, which provides a required environment for charge (ions) transferring between the anode and cathode) and the separator (which prepares the way to separate the anode and cathode mechanically to prevent internal short-circuiting and is permeable to the electrolyte in order to maintain the ionic conductivity).

The anode, which plays a role as a reducing agent, should have high coulombic output (Ah/g), good conductivity, stability and low cost. The cathode, which plays a role as an oxidizing agent, should have a useful working voltage and be stable when in contact with the electrolyte. The electrolyte which plays a role as an ionic conductor should be nonreactive with the electrodes, should have little change in properties with changing temperature, safety in handling and low cost [3].

The batteries are classified as primary (non - rechargeable) or secondary (rechargeable) batteries. The primary batteries are not intended to be recharged, hence, are discharged and discarded. The secondary batteries are capable of recharging since the electrochemical reactions occurring in the cell are reversible. The secondary batteries, e.g. lead – acid, Nickel Cadmium (NiCd), Nickel Metal Hydride (NiMH), Lithium-ion Batteries, are characterized by high power density, high discharge rate, flat discharge curves and good low temperature performance [3, 4].

2.2 Significant Descriptions for Batteries

In this section, important definitions for batteries are presented.

The standard cell voltage (ΔE^{o} or U^{o}, in V) can be calculated from the difference between standard electrode potential of the anode and cathode which is shown in equation (2.1).

$$\Delta E^{o} = E^{o}_{\text{cathode}} - E^{o}_{\text{anode}} = U^{o} \tag{2.1}$$

At non – standard conditions, Nernst equation, which is displayed by equation (2.2), is used to calculate the cell potentials (E, in V). According to Nernst equation, R is the gas constant (8.314 $Jmol^{-1}K^{-1}$), T is the temperature, n is the number of electrons involved in the reaction, F is the Faraday constant, E^{o} is the standard cell potential and a is the ratio of the activities of products to those of reactants.

$$E = E^{o} - \frac{R \times T}{n \times F} \cdot \ln a \tag{2.2}$$

Faraday constant (shown by the symbol F), which is demonstrated by equation (2.3), is the magnitude of electric charge per mole of electrons. According to that equation, e is the magnitude of the charge of an electron (~1.602×10^{-19} J) and N_A is the Avogadro constant (~6.02×10^{23} mol^{-1}).

$$F = e \cdot N_A \tag{2.3}$$

Open circuit voltage is defined as the generated voltage of a cell when it is not connected to a circuit. As for closed circuit voltage is identified the voltage of a cell which is connected to a circuit and producing current into it.

Charge (q, in Ampere – hour), as shown in equation (2.4), is the amount of current (I, in Ampere) transferred in a unit of time (t).

$$q = I \cdot t \tag{2.4}$$

Charge capacity of a cell (Q, Ah), which is expressed in equation (2.5), is defined as the total amount of charge available from a cell.

$$Q = \int_{t_1}^{t_2} I(t) \cdot dt \tag{2.5}$$

Specific capacity of a cell ($Q_{specific}$, $mAhg^{-1}$) is defined as the capacity per mass of reactants.

The theoretical specific capacity ($Q_{theoretical}$, $mAhg^{-1}$) of an electrochemical cell, based only on the active materials participating in the electrochemical reaction, is calculated from the equivalent weight of the reactants. The theoretical specific capacity of a cell can be calculated by Faraday's law which is presented in equation (2.6). According to that equation, n is the number of charge carrier, F is the Faraday constant and M is the molecular weight of the active materials used in the electrode.

$$Q_{theoretical} = \frac{n \cdot F}{3600 \cdot M} \tag{2.6}$$

C – Rate (charge and discharge rate) is used to identify the time frame for a cycle which describes a complete charging and discharging process of a cell or battery. Hence, C/2 and 2C for example stand for a current theoretically allowing a full discharge in 2 h and ½ h, respectively.

2.3 Lithium-ion Batteries (LIBs)

Lithium-ion batteries (LIBs), which belong to the family of rechargeable (secondary) batteries, were demonstrated by John Goodenough and Koichi Mizushima in 1979 as a cell with voltage in the 4V range, using lithium cobalt oxide ($LiCoO_2$) as the positive electrode and lithium metal as the negative electrode [5]. The first commercial rechargeable lithium ion battery (LIB) using $LiCoO_2$ as the cathode and carbon as the anode was released in 1991 [6]. A typical commercial lithium ion battery consists of a graphite anode, an organic electrolyte and a transition metal oxide cathode.

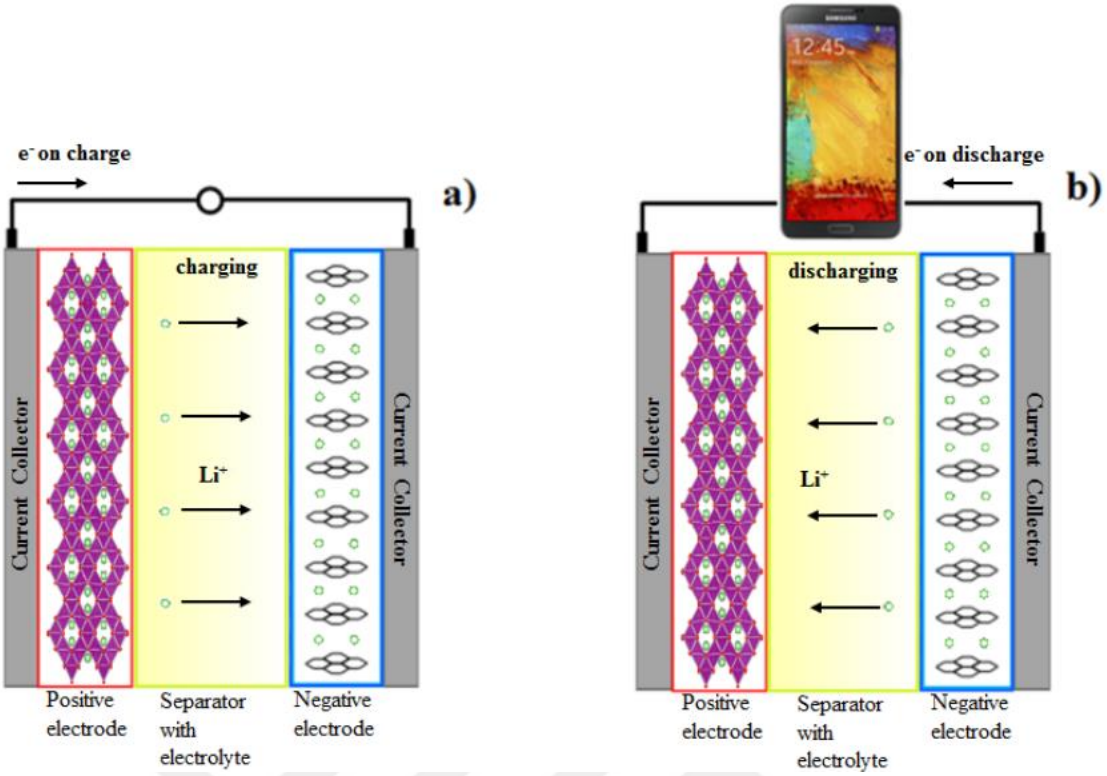

Figure 2.1 Schematic representation of movement of electrons and lithium ions during a) charging and b) discharging in a lithium ion cell [1]

The working principle of LIBs is shown in Fig. 2.1 which illustrates the movement of electrons and lithium ions during charging and discharging process in a lithium ion cell. When the current collector part of the cell connects with an external load, the negative electrode material undergoes oxidation releasing electrons and lithium ions during the discharging process. The generated lithium ions progress to the positive electrode via the electrolyte and the electrons flow from the negative electrode to the positive electrode. The discharge process happens spontaneously. The anode and cathode are described according to the discharge process. Therefore, during the discharge process, the anode is the negative electrode and the cathode is the positive electrode [3]. When the cell connects with a power supply, the flow of the lithium ions and electrons occur in the reverse way. The charge process occurs only with the external force.

Lithium-ion batteries have a whole lot of application area (such as mobile phones, laptops, video cameras, electronic devices, electrical vehicles, electromobility etc.) and many advantages and some disadvantages, relative to other types of batteries (Table 2.1).

Table 2.1 Advantages and disadvantages of LIBs [3]

Advantages	**Disadvantages**
Sealed cells; no maintenance required	Moderate initial cost
Long cycle life	Degrades at high temperature
Broad temperature range of operation	Need for protective circuitry
Long shelf life and discharge rate	Capacity loss or thermal runaway when overcharged
Rapid charge capability	Venting and possible thermal runaway when crushed
High rate and high power discharge capability	Cylindrical designs typically offer lower power density than NiCd or NiMH
High coulombic and energy efficiency	
High specific energy and energy density	
No memory effect	

2.3.1 Negative Electrodes for LIBs

The first battery based on the principle of lithium intercalation into the electrode material was developed in the late 1970´s by John Goodenough and Koichi Mizushima. Metallic lithium was used as the first anode material. The advantage of using lithium metal in LIB is that lithium metal is the lightest metal among all metals and it has high specific capacity. However, metallic lithium is expensive and causes capacity loss because of dendrite formation and there are safety issues [1]. Although metallic lithium cannot be used for commercial batteries due to the safety requirements, it is often used as an anode in half – cells in the electrochemical testing of cathode materials [7]. Due to these disadvantages, researchers focused on using lithium intercalation into carbon at the negative electrode instead of metallic lithium [3].

Depending on carbon content, the negative electrodes for LIBs could be mainly classified as carbonaceous or non – carbon based materials. Graphite and non – graphitic carbon anodes, which include mainly hard carbon, could be exemplified as the carbonaceous materials. Binary or ternary lithium metal alloys such as tin, silicon, lead, antimony, aluminum and bismuth, and titanium containing compounds such as titanium spinel

($Li_4Ti_5O_{12}$) and titanium dioxide (TiO_2) could be given as examples of the non – carbon based materials for LIBs [7].

2.3.2 Positive Electrodes for LIBs

The positive electrode for a LIB must have high free energy of reaction with lithium, high lithium ion diffusivity, good electronic conductivity, must be insoluble in the electrolyte and should have low cost. Furthermore, it should incorporate large quantities of lithium and the incorporating process should be reversible [3].

The positive electrode materials for LIBs could be mainly distinguished into three major classes: phosphate – based materials, layered type oxides and spinel type oxides [7]. The electrochemical characteristics and simplified crystal structures of Li ion battery cathode materials are presented in Figure 2.2.

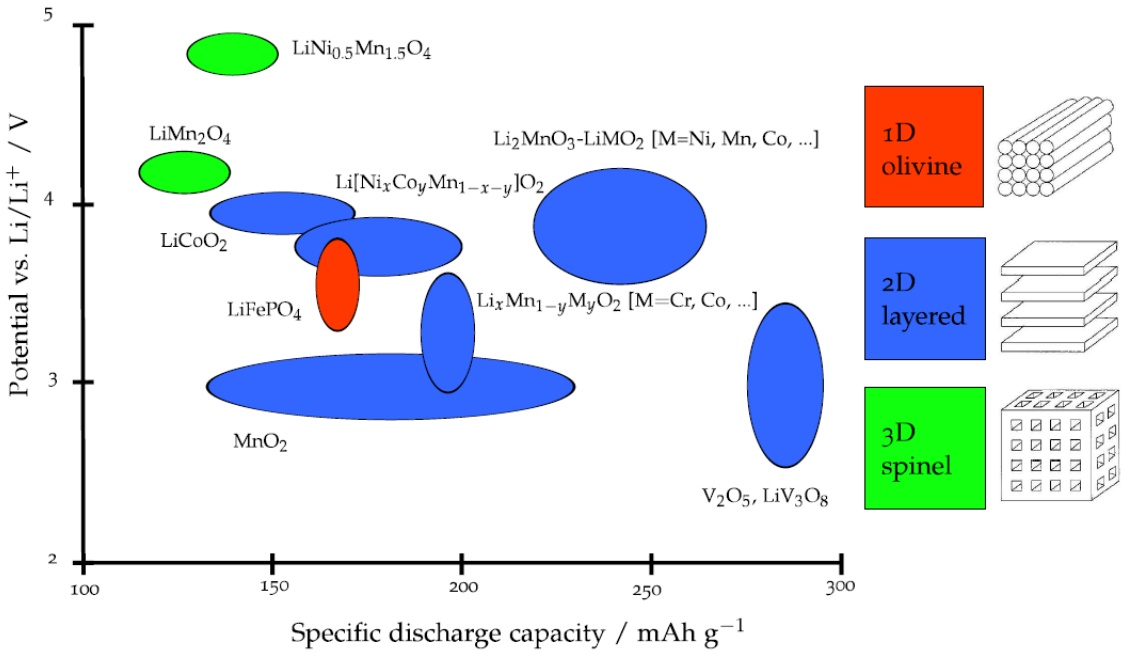

Figure 2.2 Electrochemical characteristics and simplified crystal structures of LIB cathode material [7]

The phosphate – based materials with similar structure to the mineral olivine can have a general formula Li*M*PO_4, where *M* can be Fe, Mn, Co, Ni etc. Among them, $LiFePO_4$ is an attractive candidate for electrodes for LIBs. Recently commercialized $LiFePO_4$ is environmentally friendly and can be potentially inexpensive. However, the synthesis of high-performance $LiFePO_4$ requires special approaches to overcome low electronic and ionic conductivity [9].

The layered type oxides can be represented by a general formula LiMO_2, where M can be one or more transition metals. $LiCoO_2$, which is a member of this type of cathode materials and belongs to the $R\bar{3}m$ space group, exhibits a very good cycleability as a cathode material in lithium ion commercial batteries [7]. However, this material has high toxicity and low natural abundance [10].

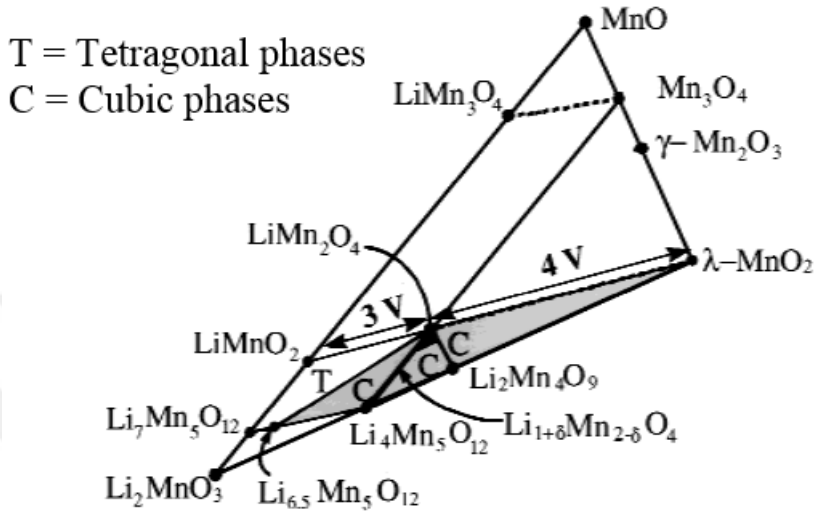

Figure 2.3 Section from the Li – Mn – O phase diagram at room temperature [11]

The spinel type oxides exist in many different stoichiometric compositions which reside on the tie line between Mn_3O_4 and $Li_4Mn_5O_{12}$ in the Li – Mn – O phase diagram (Fig. 2.3). On the tie line between $Li_4Mn_5O_{12}$ and $LiMn_2O_4$ whose Mn valance and crystallographic structures of the spinels are shown in Table 2.2 [12] are attractive spinel compounds for rechargeable LIBs [11].

Table 2.2 Mn valance and crystallographic cubic structures of the spinels on the tie line between $Li_4Mn_5O_{12}$ and $LiMn_2O_4$ [12]

Composition	**Mn valence**	**Crystallographic structure (a in Å)**
$LiMn_2O_4$	3.5	Cubic spinel ($Fd\bar{3}m$) a = 8.2476(2)
$Li_{1+x}Mn_{2-x}O_4$	3.5 – 4	Cubic spinel ($Fd\bar{3}m$) a ≅ 8.21 – 8.24
$Li_2Mn_4O_9$	4	Cubic spinel ($Fd\bar{3}m$) a = 8.162
$Li_4Mn_5O_{12}$	4	Cubic spinel ($Fd\bar{3}m$) a = 8.1616(5)

The spinel $LiMn_2O_4$ is a very promising class of cathode material for LIBs due to its low toxicity and cost, high natural abundance of Mn, high reversible capacity [13], good electrochemical and safety properties [3]. Based on the annealing temperature, two different crystallographic modifications exist for $LiMn_2O_4$: cation – ordered spinel ($P4_332$ space group) and cation – disordered spinel ($Fd\bar{3}m$ space group) [11]. In the cation – disordered $LiMn_2O_4$ spinels, a cubic – close – packed (ccp) array of oxygen ions occupy the 32e position, Mn ions are located in the 16d site and Li in the 8a site. Moreover, unmodified cation – disordered $LiMn_2O_4$ spinels exhibit an unacceptably high capacity fading due to the Jahn – Teller distortion, dissolution of manganese and lattice instability [14]. Researches have shown that partial substitution of a transition metal for Mn, yielding $LiM_xMn_{2-x}O_4$ (where M = Co, Cr, Ni, Fe, Ti and Zn) is recognized as an approach for improving the cathodic stability of the spinel lattice [15]. This makes the substituted manganese spinels attractive candidates for improving advanced cathode materials for LIBs.

This thesis is mainly focused on synthesis and optimization of $LiCu_{0.5}Mn_{1.5}O_4$ and $LiNi_{0.25}Cu_{0.25}Mn_{1.5}O_4$ spinels as high – voltage cathode materials for rechargeable LIBs. Some parts of research were focused on synthesizing these materials by solid–state, ultrasonic spray pyrolysis and sol – gel methods [15 – 18]. Out of these, the sol – gel synthesis is more attractive as it is a low – temperature synthesis method which results in high homogeneity of the products and provides a good control over the stoichiometry [7]. Due to these advantages, sol – gel method was preferred in this work. Yair et al. have reported that it is difficult to synthesize single phase lithium – copper – manganese – oxide spinel compounds with a predetermined composition because the stability and relatively low reactivity of CuO appears to restrict the complete incorporation of copper into the spinel structure.

The lithium can be extracted from the $LiCu_{0.5}Mn_{1.5}O_4$ spinel structure in two main potential regions: around 4 V and 5 V, attributing to the oxidation of Mn^{3+} to Mn^{4+} and Cu^{2+} to Cu^{3+}, respectively [15, 16, 19]. The $LiNi_{0.25}Cu_{0.25}Mn_{1.5}O_4$ spinel also shows two main potential regions (4 and 5 V regions) to extract the lithium, 5 V region assigns to the Ni^{2+} / Ni^{4+} and Cu^{2+} / Cu^{3+} redox couples [19, 20].

Although the reversible capacity of the $LiCu_{0.5}Mn_{1.5}O_4$ spinel (~72 mAh/g) is less than the reversible capacity of the $LiNi_{0.25}Cu_{0.25}Mn_{1.5}O_4$ (~120 mAh/g) spinel, the

$LiCu_{0.5}Mn_{1.5}O_4$ spinel electrodes are significantly more stable to electrochemical cycling than the $LiNi_{0.25}Cu_{0.25}Mn_{1.5}O_4$ spinel electrodes [19].

2.3.3 Electrolytes for LIBs

Electrolyte is an indispensable element of the battery, which enables the electrode reactions and affects the performance of the battery. Four types of electrolytes have been used in LIBs: liquid electrolytes, gel electrolytes, polymer electrolytes and ceramic electrolytes [3]. The standard electrolyte used in the current LIBs is a solution of $LiPF_6$ salt dissolved in a mixture of ethylene carbonate (EC) and other linear carbonates with little variation in the salt concentration and solvent ratio [4]. The reasons to select $LiPF_6$ salt might be listed as follows:

- It offers high ionic conductivity (~ 10 mS/cm at room temperature).
- It participates in the formation of stable SEI (Solid Electrolyte Interface) on the graphite surface.
- It passivates Al current collector at high potentials.
- It is stable over a wide electrochemical window.

In this study, 1 M $LiPF_6$ in ethylene carbonate (EC):dimethyl carbonate (DMC) (1:1 w/w) was used as the electrolyte.

2.3.4 Separators for LIBs

The separator is a porous membrane that absorbs the liquid electrolyte and physically isolates the cathode and anode to prevent the short – circuit inside the cell. The separator currently used in LIBs is typically a microporous polyethylene (PE) or polypropylene (PP) membrane, which might exist in a single layer or a multilayer structure with variations in porosity, pore size, thickness and mechanical strength [4].

In this work, two pieces of Celgard® trilayer PP/PE/PP which were soaked in the electrolyte for minimum 8 hours were used as a separator for preparation of each half test cell.

CHAPTER 3

EXPERIMENTAL

3.1 Synthesis of the Materials

In this work, $LiCu_{0.5}Mn_{1.5}O_4$ and $LiNi_{0.25}Cu_{0.25}Mn_{1.5}O_4$ spinel materials were synthesized by a citric acid assisted Pechini sol-gel process. The Pechini process is based on three basic reactions; formation of metal chelates, esterification and polymerization [4]. The reaction scheme of this process with some photos which were taken in due course of synthesis is illustrated in Fig 3.1. After the reaction steps, obtained powder can be calcined to get pure phase oxides [21].

In the first step of the process, citric acid (VWR Prolabe, 96 %) was mixed with ethylene glycol (Alfa Aesar, 99 %) in a 1:4 molar ratio for the synthesis of $LiCu_{0.5}Mn_{1.5}O_4$ precursor. The resulting homogeneous mixture was heated to 90 ^{O}C, the metal acetates $LiCH_3COO{\cdot}2H_2O$ (Alfa Aesar, 99 %), $Cu(CH_3COO)_2{\cdot}H_2O$ (Alfa Aesar, 98+ %), $Mn(CH_3COO)_2{\cdot}4H_2O$ (Sigma-Aldrich, 99 %) were added into the citric acid – ethylene glycol mixture and dissolved by stirring. In the next step, the temperature was increased at a heating rate of 25 ^{O}C/h to 140 ^{O}C to initiate the esterification. The esterification reaction occurs between the hydroxyl groups of ethylene glycol and carboxylic acid group of citric acid [4]. The mixture was transferred into a porcelain bowl at the last step of the process, when the mixture started to take gel form. The temperature was then increased to 180 ^{O}C to evaporate the excess ethylene glycol from the gel. The acquired gel was pre-calcined at 400 ^{O}C for 5 h at a heating rate of 5 ^{O}C/min in an oven to remove the carbon and was ground in a mortar to obtain the initial precursors.

The whole process was also carried out synthesizing $LiNi_{0.25}Cu_{0.25}Mn_{1.5}O_4$ spinel material using stoichiometric amount of Nickel (II) acetate tetrahydrate, $Ni(CH_3COO)_2{\cdot}4H_2O$ (Alfa Aesar, 98+ %).

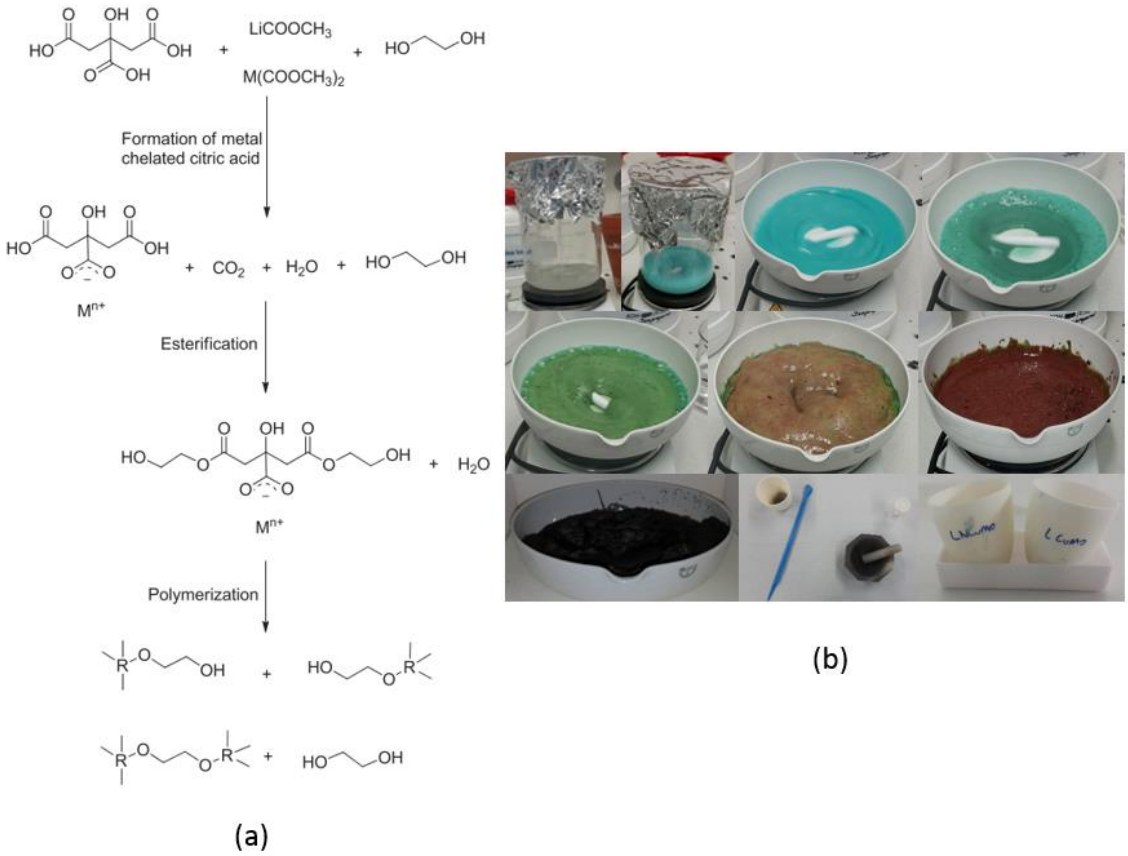

Figure 3.1 (a) Reaction scheme of the Pechini sol-gel process [21] and (b) complied photographs from the synthesis of $LiCu_{0.5}Mn_{1.5}O_4$

The ground powder precursor of $LiCu_{0.5}Mn_{1.5}O_4$ was divided into eleven samples which were treated at different annealing temperatures, time and atmosphere. The three samples of precursor of $LiCu_{0.5}Mn_{1.5}O_4$ were annealed at 600 ^{O}C for 4, 12 and 24 h in air to study the effect of the annealing time on the material. The other samples of the acquired precursor of $LiCu_{0.5}Mn_{1.5}O_4$ were annealed at 750 and 900 ^{O}C for 4 h in air, under O_2 and Ar.

The powdered precursors of $LiNi_{0.25}Cu_{0.25}Mn_{1.5}O_4$ were annealed at 600, 750 and 900 ^{O}C for 4 h under air, O_2 and Ar.

All the calcinations were performed in the oven at a heating rate of 5 ^{O}C/min using alumina crucibles and all samples were cooled down to room temperature without obvious temperature control. After every annealing step, the samples were ground and bottled.

3.2 X-Ray Diffraction (XRD)

An atom consists of a nucleus which is surrounded by electrons grouped in shells or orbitals. Irradiating an atom with X-ray photons or electrons with enough energy can throw out an electron from the atom. This puts the atom in an unstable state with a higher energy. The unstable atom emits a characteristic X-ray radiation to return to the stable state again. Each atom has its own energy levels, the emitted radiation is specific to that atom. The working principles of XRD experiments are based on measuring that characteristic X – ray radiation.

Usually different sources of X – rays are used, such as X – ray tubes and synchrotron. X–ray tubes are laboratory or conventional X – ray sources where electrons are accelerated from a heated filament towards a metal anode target (cobalt, copper, molybdenum, silver etc.) [1]. After the electrons strike the target, they lose some of their energy as characteristic radiation which produces a diffraction pattern of regularly spaced spots known as reflection.

Calculation of the characteristic radiation from measured data is attributed to Bragg´s law which is shown in the equation (4.1). According to that law, d is the spacing between scattering planes in the lattice, θ is the angle between incoming beam and the scattering plane of the crystal and λ is wavelength of the incoming beam [22].

$$2d \cdot \sin\theta = n \cdot \lambda \tag{4.1}$$

Some of the ex situ experiments were carried out with the high resolution powder diffraction beamline (P02.1) at PETRA-III, DESY, using synchrotron radiation with an energy of 60 keV (λ = 0.20726 Å) and with STOE STADIP diffractometer (Mo-$K_{\alpha 1}$ radiation, λ = 0.70932 Å) in Debye Scherrer mode for powdered samples. Glass capillaries with a diameter of 0.55 mm for ex situ experiments were filled with the ground samples.

In this study, the *in situ* diffraction experiments were performed at the Materials Science of Powder Diffraction Beamline (MSPD) at ALBA, using synchrotron radiation with an energy of 30 keV (λ = 0.42477 Å) and 9 min of the exposure time. In Figure 3.2 an overview of *in situ* experiment setup from ALBA is given. It should be noted that the term of *"in situ"* is generally used in the literature which actually means carrying out the XRD measurement from the cell during charging and discharging in this study.

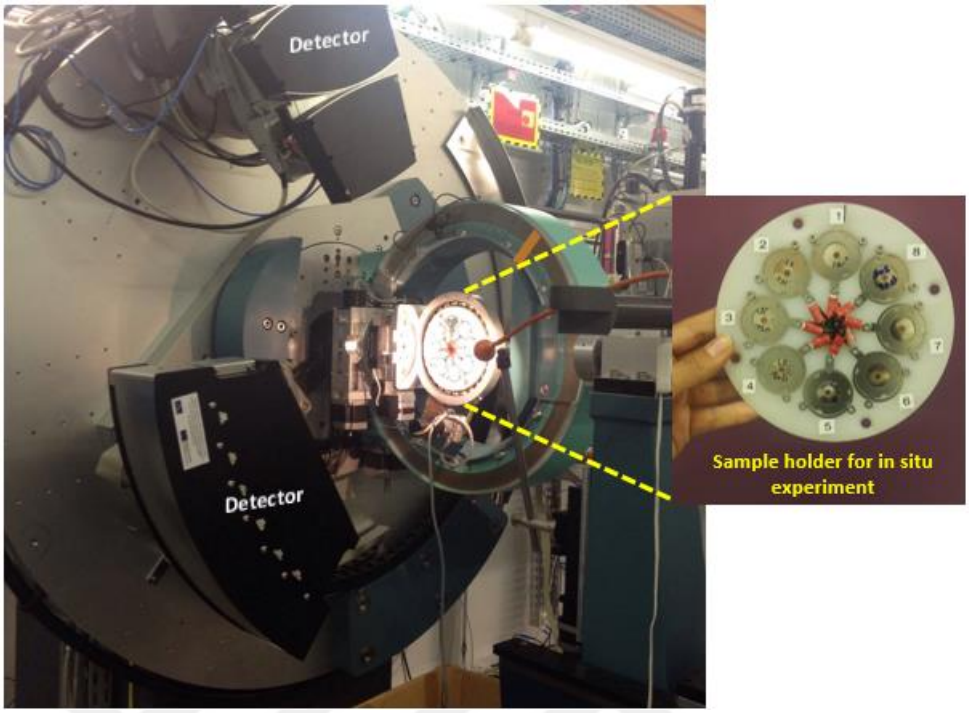

Figure 3.2 Overview of X-ray diffraction experiment setup at ALBA

CR2032 type coin cells which have been suitably designed for in situ investigations were used (Fig. 3.3). That design has a hole in the middle of the cell housing which allows the beam to pass through the sample. The cells were built in an Ar filled glove box with thin lithium foil (Alfa Aesar, 0.12 mm thickness) as anode, 200 µL LP30 (Selectipur®, 1 M $LiPF_6$ in ethylene carbonate (EC) : dimethyl carbonate (DMC) (1:1 w/w) as electrolyte and two pieces of Celgard® trilayer PP/PE/PP (soaked in the electrolyte minimum 8 hours) as separator.

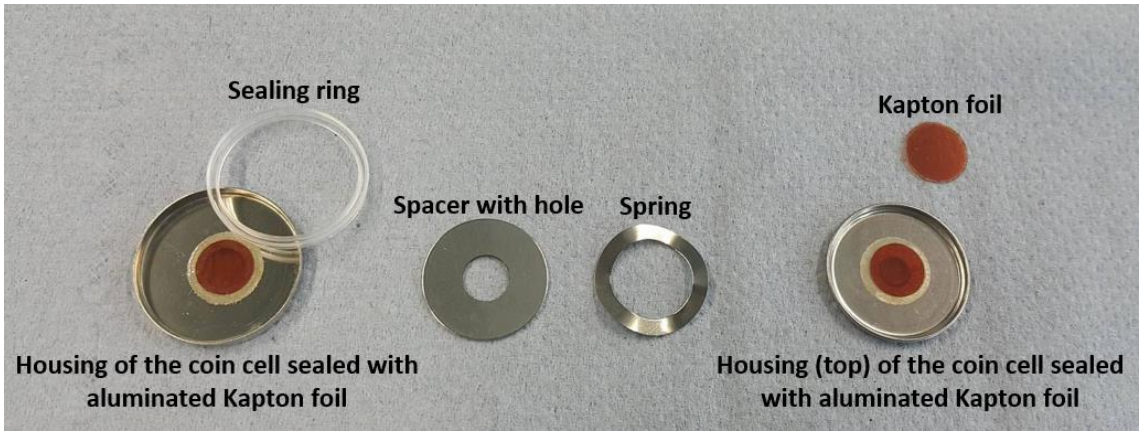

Figure 3.3 Parts of *in situ* coin cell

3.3 Inductively Coupled Plasma – Optical Emission Spectroscopy (ICP – OES)

The determination of elemental concentration was performed by ICP – OES using OPTIMA 43000V, Perkin-Elmer. The sample was dissolved in an acid in order to perform the analysis. In order to check the reproducibility of the measurements, the dissolved sample in acid was divided into three portions and they were analyzed independently. The final result is reported as an average of the three analyses.

3.4 Scanning Electron Microscopy (SEM)

An electron beam is produced by a filament (which is made of tungsten, LaB_6 etc.) or a field emission gun, then the produced electron beam passes through some system apertures and electromagnetic lenses to accelerate and focus on the sample. The electrons of the electron beam hit the sample surface, penetrate into the sample and scatter as electrons and X – rays of the sample. These scattered electrons which could be secondary electrons or backscattered electrons are collected by a suitable detector and then monitored by the microscope operator.

In this study, SEM measurements were carried out by using FE – SEM MERLIN microscope (ZEISS) with primary energy of 10 keV. Before acquiring SEM images, a small portion of the ground powder samples were spread onto a conductive carbon tape, which later were mounted on a specimen holder. The spot size and acceleration voltage were varied for different measurements to obtain better images. The images were taken in secondary electron mode.

3.5 X-Ray Absorption Spectroscopy (XAS)

XAS which is an element specific spectroscopic characterization method which is usually carried out at large synchrotron facilities, where tunable and intense radiation sources are often accessible [24]. The working principle of the XAS measurements are based on the absorption which can be used for studying oxidation states as well as local coordination of an absorbing atom [1].

In this work, XAS measurements were performed for $LiCu_{0.5}Mn_{1.5}O_4$ annealed at 600, 750 and 900 ^{O}C and $LiNi_{0.25}Cu_{0.25}Mn_{1.5}O_4$ annealed at 900 ^{O}C for 4 h in air. XAS measurements on Mn and Cu K-edge were carried out at the XAS beamline, ANKA, Karlsruhe. XAS spectra on electrodes were recorded in transmission geometry for both

Mn and Cu K edges. The spectra were processed using the Demeter software package based on IFEFFIT and FEFF [23]. The X-ray absorption near edge (XANES) spectra of all four samples at the Mn and Cu edges were compared with reference materials to obtain the oxidation states.

3.6 Nuclear Magnetic Resonance Spectroscopy (NMR)

Solid state MAS (Magic Angle Spinning) NMR spectroscopy is an element specific spectroscopic method that can be used on a large number of elements in order to investigate local structures around these elements as well as dynamics of ions in condensed matter [1].

In this study, ^{7}Li and ^{63}Cu MAS NMR was performed on a Bruker Avance 200 MHz spectrometer (B_0 = 4.7 T) using 2.5 mm zirconia rotors in a dry nitrogen atmosphere. An aqueous 1 M LiCl solution was used as the reference for chemical shift of ^{7}Li (0 ppm). Cu(I)Cl was used to reference the ^{63}Cu spectra (0 ppm). The experiments were performed at 298 K and a spinning speed of 30 kHz with a rotor synchronized Hahn-echo sequence ($\pi/2$-τ-π-τ-acquisition).

3.7 Electrochemical Experiments

3.7.1 Electrode Preparation

All of the working electrodes in this study were prepared as a mixture including 80 % (w/w) of active material, 10 % (w/w) super C 65 carbon (TIMCAL) and 10 % (w/w) polyvinylidenefluoride (Solef PVdF 6020 binder, Solvay). Carbon black was used to increase the conductivity of the active material and PVdF was used as a binder to keep the active material and the carbon black together.

Required amount of the active material and the carbon black were mixed by means of acetone in a mortar until the mixture became homogenous. The mixture was put in an oven which was at 80 ^{O}C to evaporate the acetone from the mixture. Afterwards, the mixture was ground and weighed. Stoichiometric amount of PVdF-NMP (N-methyl-2-pyrorolidone, Sigma-Aldrich) solution involving 5 % (w/w) PVdF was added onto the active material-carbon black mixture and was stirred at least 4 hours. Extra NMP was supplemented to adjust the viscosity of the mixture during stirring. The slurry obtained was coated on a special aluminum foil at wet thickness of 120 µm and 300 µm. The coated

foils were dried at 80 ^{O}C overnight and then punched with a diameter of 12 mm. Some of the obtained electrodes were not pressed and the other electrodes were pressed at different pressures which were 4, 6 and 8 tons/cm^2. Photographs of the coating and the pressing steps are shown in Figure 3.4. The electrodes were then dried at 80 ^{O}C for overnight in a vacuum oven in a glove box filled with Argon. The dried electrodes were then weighed and the final weight of the electrodes was recorded. The electrodes with wet thickness of 120 and 300 µm were approximately 1.5 and 4.5 mg, respectively.

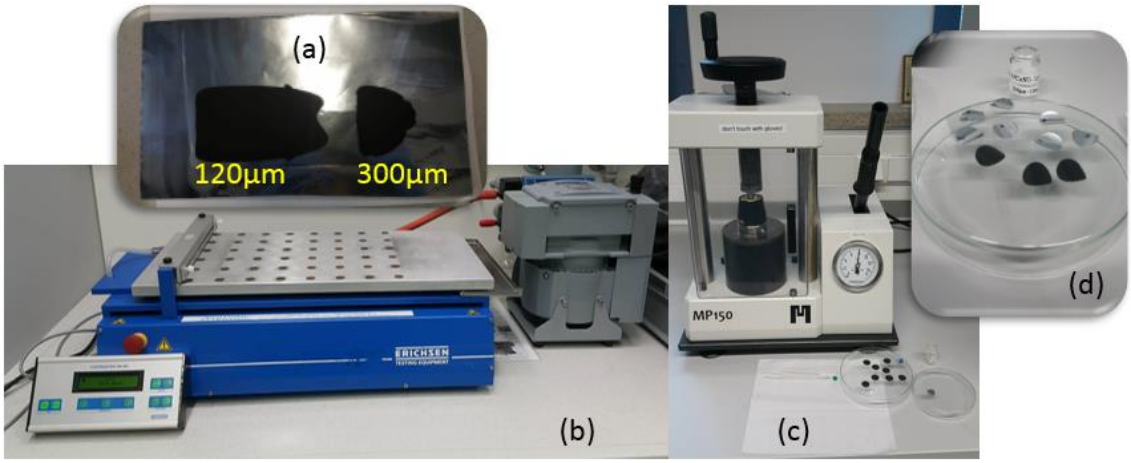

Figure 3.4 Overview of coated materials on the alumina foil (a), coating machine (b), pressing step (c) and the electrodes obtained after pressing with 8 tons/cm^2 (d)

3.7.2 Test Cells Preparation

Electrochemical experiments were carried out by using CR2032 type coin cell which were built in an Ar filled glove box with thin Li foil (Alfa Aesar, 0.12 mm thickness and 12 mm diameter) as anode, 200 µL LP30 (Selectipur®, 1 M $LiPF_6$ in ethylenecarbonate (EC) : dimethylcarbonate (DMC) = 1:1 w/w) as electrolyte and two pieces of Celgard® trilayer PP/PE/PP (soaked in the electrolyte minimum 8 hours) as separator for each half test cell. The schematic drawing of the half test cell is illustrated in Figure 3.5.

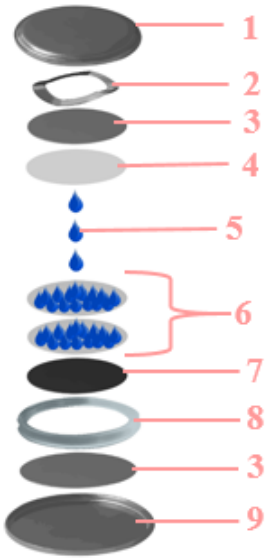

1. Housing of coin cell (top)
2. Spring
3. Spacer
4. Lithium Foil
5. Electrolyte
6. Separator
7. Working electrode
8. Plastic sealing ring
9. Housing of coin cell

Figure 3.5 Schematic drawing of CR2032 type half test cell

3.7.3 Electrochemical Technique

Electrochemical cycling experiments were carried out by using VMP3 and BCS (Bio - Logic Science Instruments) multichannel potentiostat (Figure 3.6) which was controlled by computer with the help of a software EC-Lab (Bio-Logic Science Instruments). All electrochemical experiments were performed at room temperature.

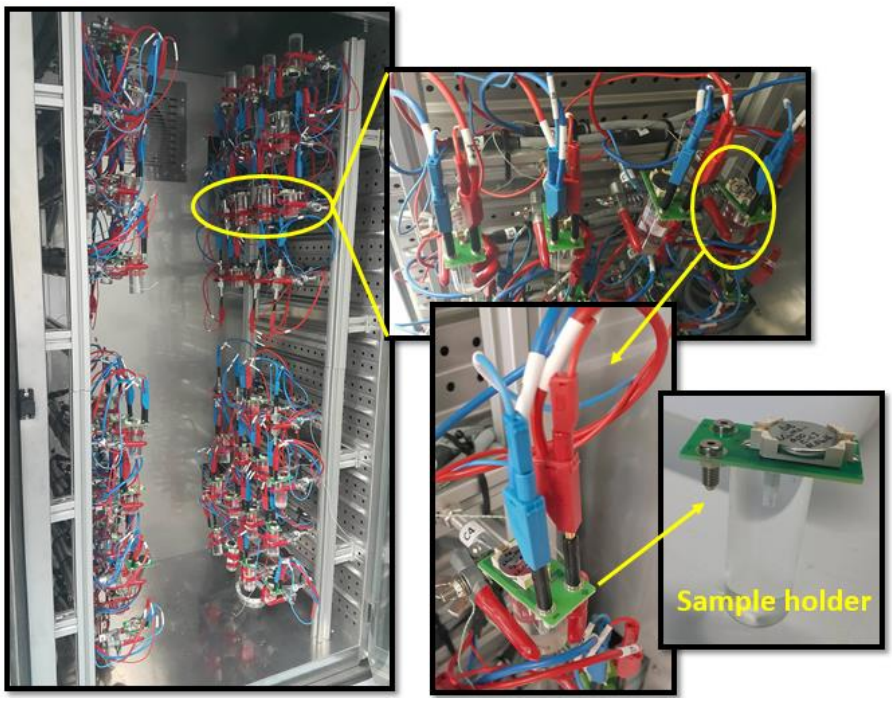

Figure 3.6 Overview of the potentiostat setup

Cycling Voltammetry (CV) technique provides information about the electrochemically active regions of the working electrode during scanning of the potential between two given values at a fixed rate. CV technique is usually performed with 3 – electrodes: working, reference and counter electrodes. In this study, lithium was used as a counter and reference electrode and the results of CV experiments recorded the potential of the working electrode against reference electrode. A scan rate of 0.15 mV/s was constantly used.

Galvanostatic Cycling (GCPL) technique is used to provide information about potential changes of the working electrode against the reference electrode keeping the current constant. In this study, GCPL technique was applied in order to investigate the cycling stability of the working electrode. The current rate was kept constant (C/3.5) during the charging and discharging processes. Furthermore, the range of potential limit was applied as 3 – 5.1 V.

CHAPTER 4

RESULTS AND DISCUSSION

4.1 $LiCu_{0.5}Mn_{1.5}O_4$ High Voltage Spinel Cathode Material

4.1.1 Results of Annealed $LiCu_{0.5}Mn_{1.5}O_4$ in Air Cathode Materials

In this study, for the $LiCu_{0.5}Mn_{1.5}O_4$ (LCuMO) cathode material annealed in air, three different annealing temperatures: 600, 750 and 900 ^{o}C were chosen; and to understand the influence of the annealing time on the LCuMO, three different time periods: 4, 12 and 24 h were used. The results obtained for the cathode materials are given and discussed in the following sections.

4.1.1.1 The influence of Annealing Time on Structural Characteristic

$LiCu_{0.5}Mn_{1.5}O_4$ (LCuMO) powders annealed at 600 ^{o}C in air for 4, 12 and 24 h, for which Rietveld refinement patterns are presented in Figure 4.1, have a cubic spinel phase (Space Group (SG) $Fd\bar{3}m$). In addition to the main phase, the samples contain almost same ratio of CuO (SG *C12/c1*), respectively; fractions of CuO phase are 7.2, 7.1 and 7.2 % obtained for 4, 12 and 24 h (see Table 4.1).

In the diffraction patterns of the lithium manganese spinels, the 220 reflection is usually not visible due to low scattering ability of lithium. The presence of this reflection in the diffraction patterns (see Fig. 4.1) indicates that some Cu atoms exist on the 8a tetrahedral sites normally occupied by Li [15]. Therefore, all the Rietveld analyses in this study were performed with a structural model based on a partial occupation on the 8a site by Cu atoms. In all the diffraction patterns shown in this work, the observed data are shown as points in red, the calculated profiles are shown as black lines, the corresponding difference between observed data and calculated profile are data shown as blue lines and the calculated Bragg positions of reflections are shown as vertical green marks.

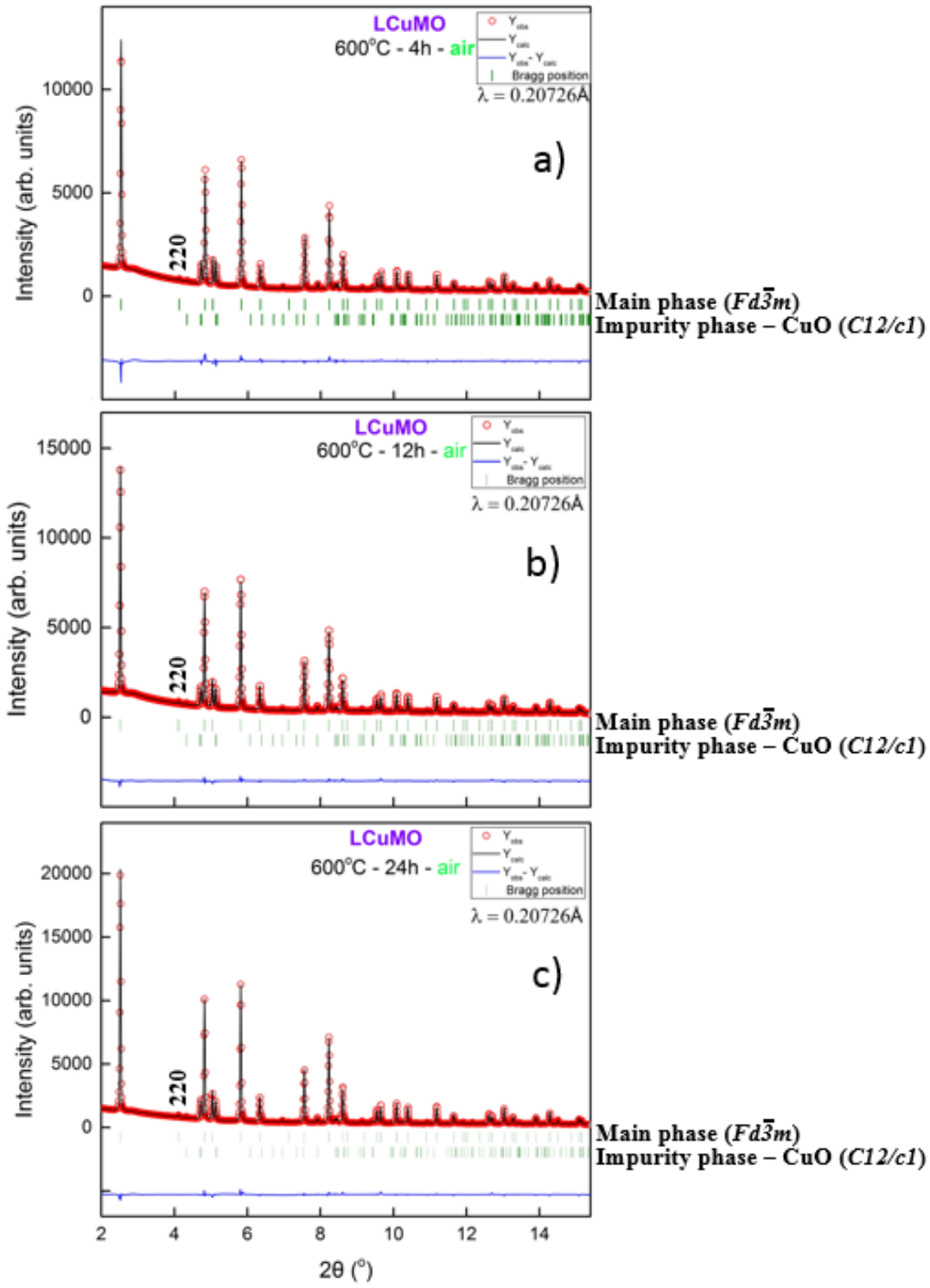

Figure 4.1 Rietveld refinement of diffraction patterns of LCuMO annealed at 600°C in air of as prepared a) 4 h b) 12 h c) 24 h materials measured in 0.5 mm capillaries

In Table 4.1 the Rietveld refinement results of annealed LCuMO at 600 °C in air samples show that, the annealing time changes have a passive impact on the structural characteristics of the samples. It might be concluded that prolongation annealing at 600 °C does not affect the structural parameters.

Table 4.1 Rietveld refinement results of LCuMO annealed at 600 ^{o}C in air samples

Annealing time of samples [h]	Atomic site	x=y=z	a [Å]	Volume [Å^3]	Fraction of impurity phase [%]	Cu on the tetrahedral site (8a) [%]	Overall temperature factor (B_{ov})	R_{wp} [%]
4	Li_{8a} Cu_{8a} Mn_{16d} Cu_{16d} Li_{16d} O_{32e}	0.125 0.125 0.500 0.500 0.500 0.2636(5)	8.1810(3)	547(3)	7.2	3.6	0.70	7.90
12	Li_{8a} Cu_{8a} Mn_{16d} Cu_{16d} Li_{16d} O_{32e}	0.125 0.125 0.500 0.500 0.500 0.2627(2)	8.1806(1)	547(1)	7.1	2.5	0.62	5.60
24	Li_{8a} Cu_{8a} Mn_{16d} Cu_{16d} Li_{16d} O_{32e}	0.125 0.125 0.500 0.500 0.500 0.2630(3)	8.1815(2)	547(2)	7.2	2.8	0.63	7.21

4.1.1.2 Elemental Analysis

The chemical composition of the LCuMO sample which was annealed at 600 ^{o}C for 4 h was analysed by ICP – OES and the results are shown in Table 4.2. The observed values were calculated assuming that Li has complete stoichiometry and the obtained result shows that the stoichiometry of the sample calculated from the ICP – OES analysis is in good agreement with the stoichiometric amounts of lithium, copper and manganese taken for the synthesis.

Table 4.2 Results of ICP – OES analyses of LCuMO annealed at 600 ^{o}C for 4 h

Sample	Ratio of Li: Transition Metals (expected)	Ratio of Li: Transition Metals (observed)	Ratio of Transition Metals Cu : Mn (observed)
LCuMO - 600°C – 4h	0.5	0.5027	0.493(2) : 1.498(7)

4.1.1.3 Nuclear Magnetic Resonance (NMR) Spectroscopic Studies of LCuMO Cathode Material

Figure 4.2 shows ^{63}Cu MAS NMR spectra of the cathode material LCuMO annealed at 600 ^{o}C for 4 h in air. The Cu in the LCuMO and CuO structures should be in 2+ state ($3d^9$) and that makes it a paramagnetic substance. Therefore, taking the MAS NMR measurement directly is not possible. At around 2290 ppm the peak of CuO and LCuMO cathode material belongs to RF (Radiofrequency) coil which is made of Cu.

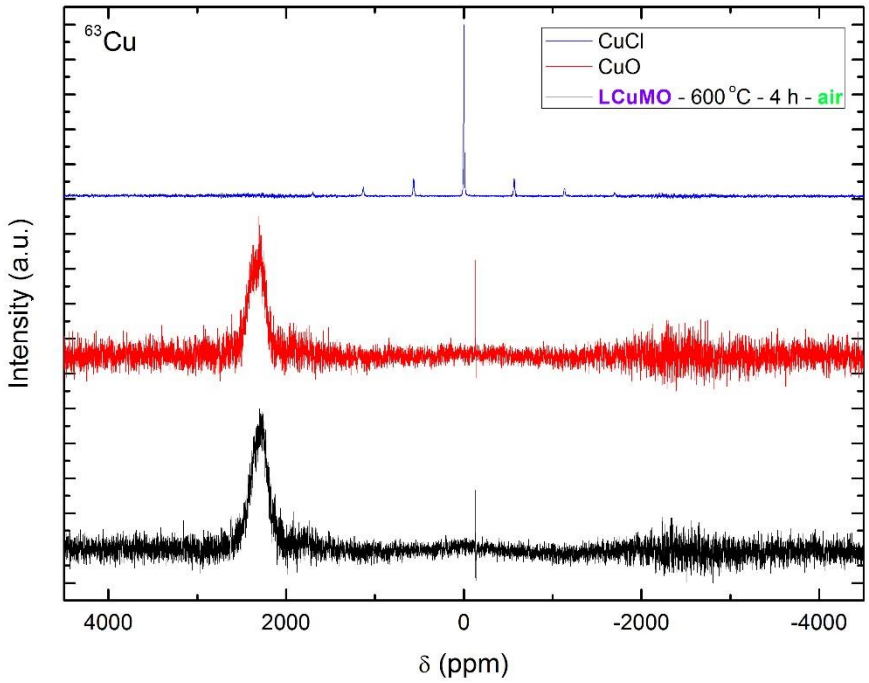

Figure 4.2 ^{63}Cu MAS NMR spectra of the LCuMO annealed at 600 ^{o}C for 4 h in air

In Figure 4.3, ^{7}Li MAS NMR spectra of $LiMn_2O_4$ and cathode material LCuMO annealed at 600 ^{o}C for 4 h in air cathode material are shown and the spinning sidebands of LCuMO are marked with asterisk. LCuMO spectrum compared to undoped $LiMn_2O_4$ spectrum exhibits an overall chemical shift of ~ 265 ppm. This shifting confirms that the local environment of Li is changed due to the presence of Cu ions.

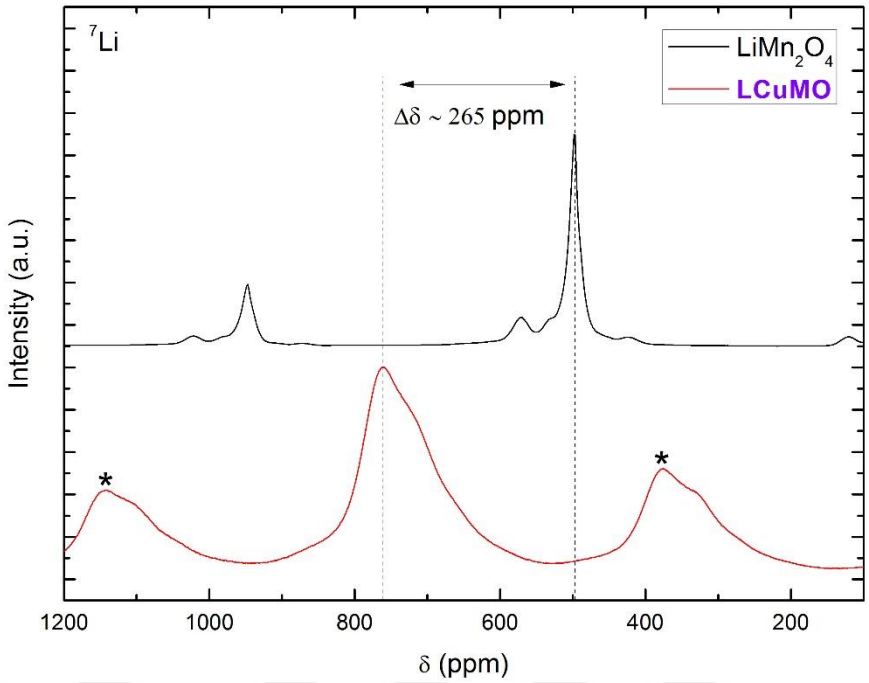

Figure 4.3 ^{7}Li MAS NMR spectra of $LiMn_2O_4$ and the cathode material LCuMO annealed at 600 ^oC for 4 h in air

In the spectrum of the cathode material LCuMO annealed at 600 ^oC for 4 h in air (Figure 4.4), one broad peak is observable in the range between 575 and 950 ppm. A satisfactory fit was achieved by using Gaussian function yielding an NMR shift of 761 ppm. The observed complex line shape which is fitted with 4 peaks located at 663, 720, 765 and 868 ppm. In this case, 12 transition metal ions around the Li ion can be occupied by different ratios of Cu^{2+} and Mn^{4+}. The most probable local environment options for Mn/Cu-O-Li bonds are 9 Mn^{4+} and 3 Cu^{2+}, however other environments can also exist. In summary ^{7}Li MAS NMR spectroscopy confirms that the Cu ions are successfully incorporated into the spinel lattice of $LiMn_2O_4$.

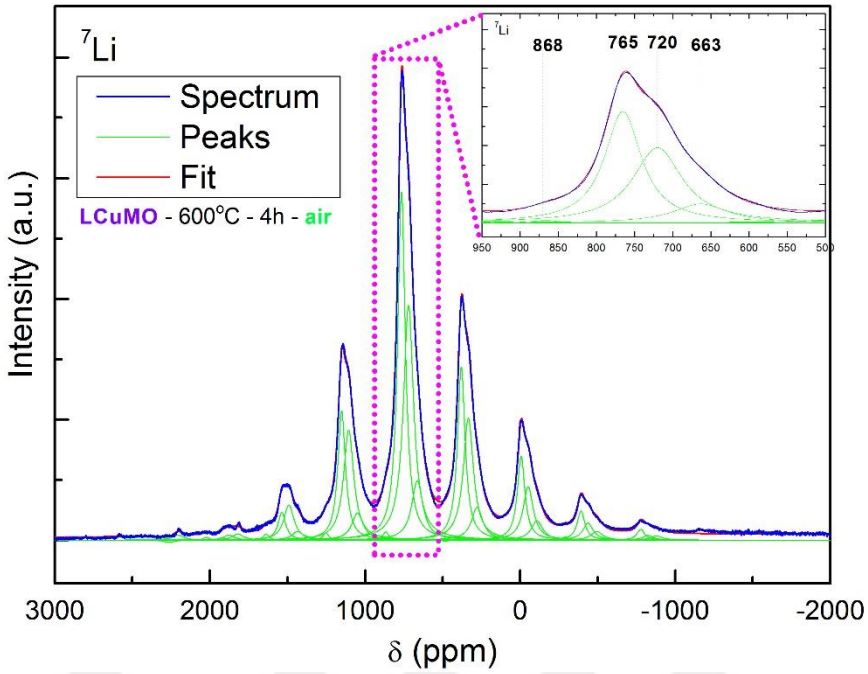

Figure 4.4 ^{7}Li MAS NMR spectra of the cathode material LCuMO annealed at 600 ^{o}C for 4 h in air with fit peaks

4.1.1.4 Morphology Studies on Influence of the Annealing Time

SEM images of LCuMO – precursor, the LCuMO annealed at 600 ^{o}C 4 h, 12 h and 24 h in air powders are presented in Figure 4.5. The images were taken in secondary electron mode with an acceleration voltage of 10 kV. Different shape of particles are seen and the particle size of the powders is in the range of 500 nm and bigger. Furthermore, the SEM images obtained show that the annealing time has only minor impact on the particle size and morphology.

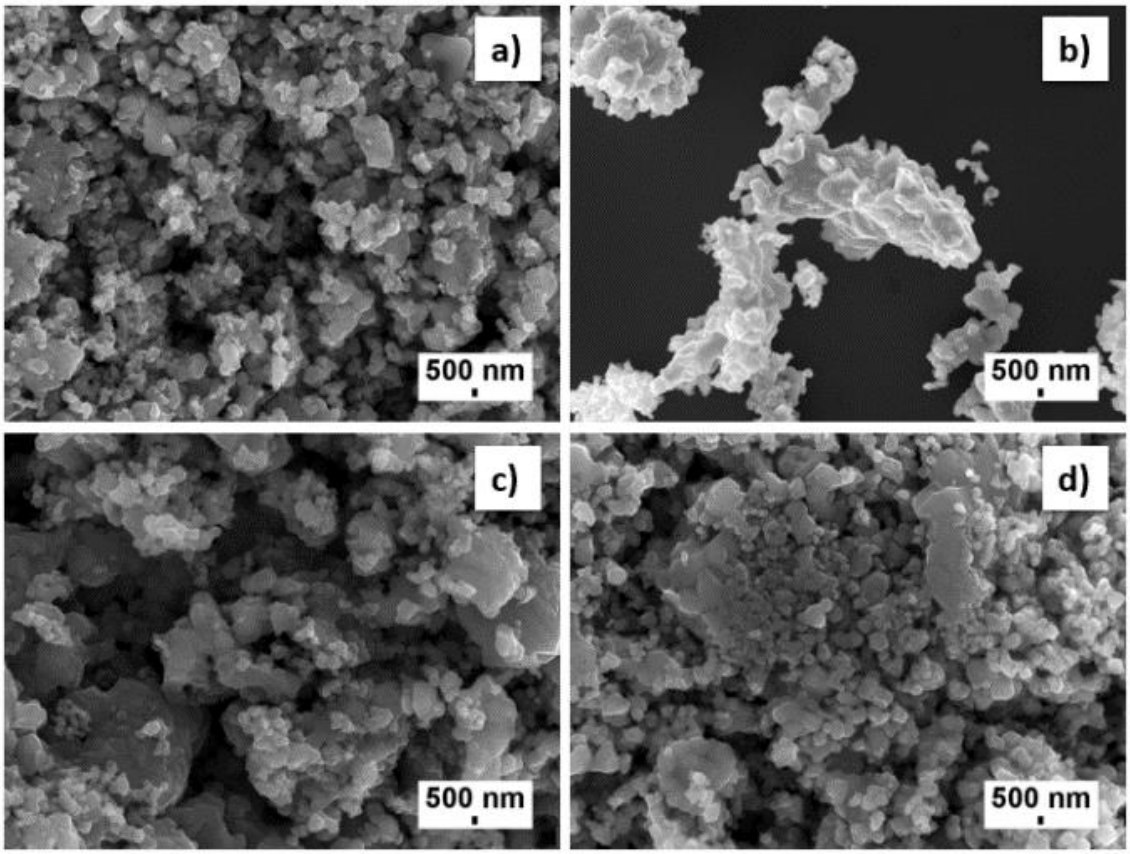

Figure 4.5 SEM images of a) LCuMO – precursor, b) the annealed LCuMO at 600°C 4 h in air, c) the annealed LCuMO at 600°C 12 h in air, d) the annealed LCuMO at 600°C 24 h in air

4.1.1.5 Cycling Voltammetry

The electrochemical test cell with cathode material LCuMO annealed at 600 ^{o}C for 4 h in air was cycled between the voltage range 3–5.3 V with a scan rate of 0.15 mVs^{-1}. The cycling voltammogram of 1st and 5th cycles of the testing material is shown in Figure 4.6. According to that voltammogram, there are two reversible electrochemical reactions in the cell at around 4 and 5 V. The reversible electrochemical activity at around 4 V is attributed to the Mn^{3+} / Mn^{4+} redox couple [15, 16], which is still present after 5 cycles. At around 5 V another reversible electrochemical activity is attributed to the Cu^{2+} / Cu^{3+} redox couple [15, 16], which is also still present after 5 cycles. The onset of the electrolyte oxidation was noted at 5.15 V.

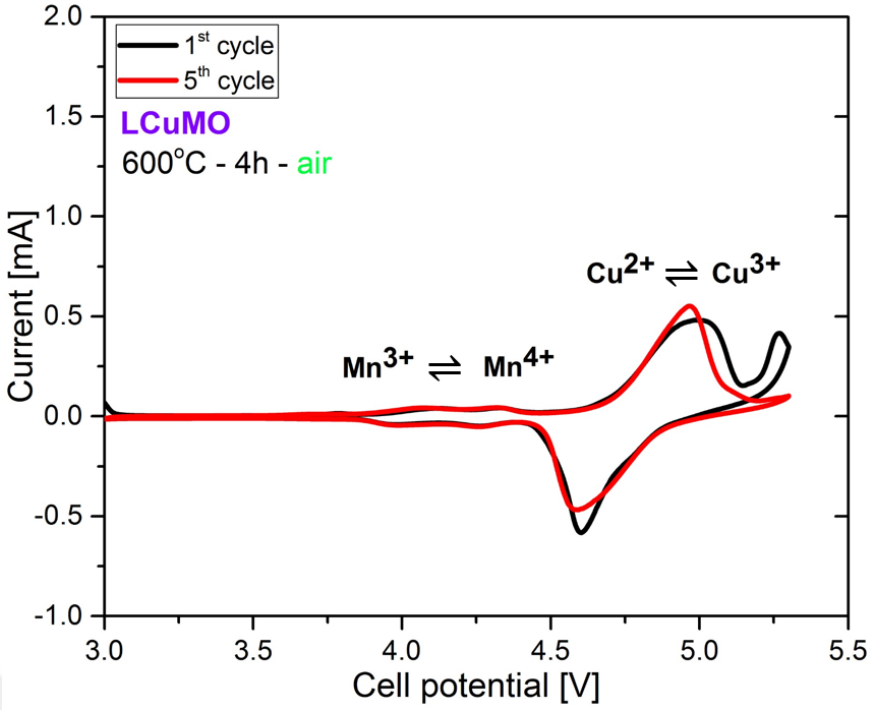

Figure 4.6 The Cycling voltammogram of 1st and 5th cycles of the cathode material LCuMO annealed at 600 °C for 4 h at a scan rate of 0.15 mV s^{-1} in a voltage range 3 – 5.3 V

4.1.1.6 The Influence of Annealing Time on the Cycling Stability and Electrochemical Characterization

The voltage profiles of the LCuMO annealed at 600 °C in air for 4, 12 and 24 h cycled at C / 3.5 charge – discharge rate for the 1st cycle are shown in Figure 4.7. The sample annealed for 4 h exhibits lower electrochemical activity at 4 V region than the others as revealed from the smaller plateau obtained at 3.75 – 4.25 V voltage region. Electrochemical activity at 4 V directly correlates to the amount of Mn^{3+} in the sample [1]. The Mn^{3+} contents in the LCuMO annealed at 600 °C in air for 4, 12 and 24 h, which are calculated from the capacity obtained at the 4 V region, are 0.211, 0.279 and 0.260 moles, respectively. Moreover, the Cu^{2+} contents in the sample annealed for 4, 12 and 24 h, which are calculated from the capacity obtained at the 5 V region, are 0.291, 0.395 and 0.376 moles, respectively.

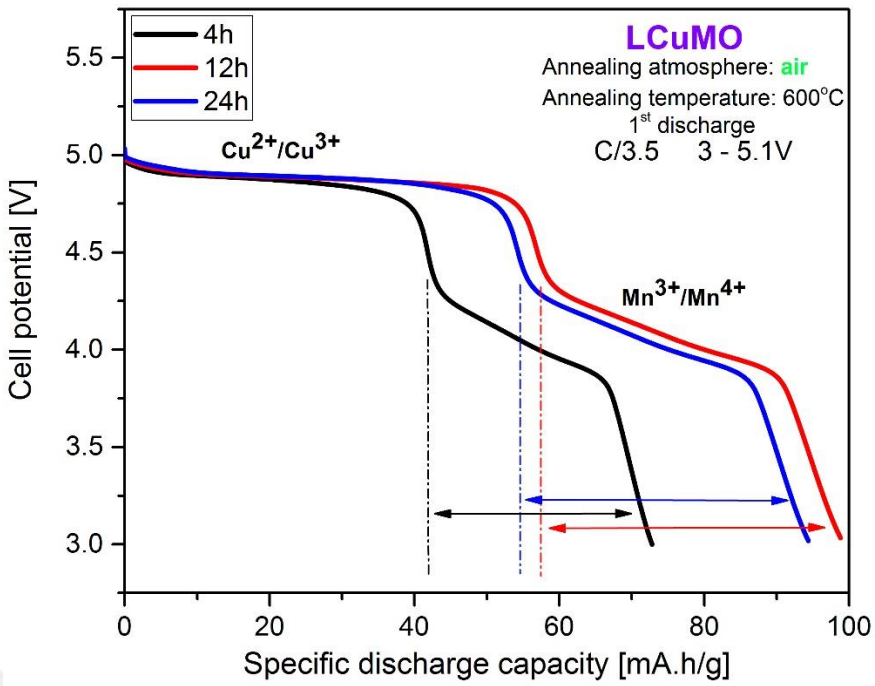

Figure 4.7 Cell potential vs. specific discharge capacity curves of 1st discharge of the cathode materials LCuMO annealed at 600 °C in air for 4 h (black), 12 h (red) and 24 h (blue)

Curves of the cell voltage vs. Li content in the material for the LCuMO annealed at 600 °C in air for 4, 12 and 24 h cycle at C / 3.5 charge – discharge rate for the 1st cycle are shown in Figure 4.8. At the end of the 1st charge, Li contents of the materials annealed for 4, 12 and 24 h materials are 0.38, 0.41 and 0.40 and at the end of the 1st cycle, the fade ratio of the Li content in the materials are 12, 9 and 8 %, respectively.

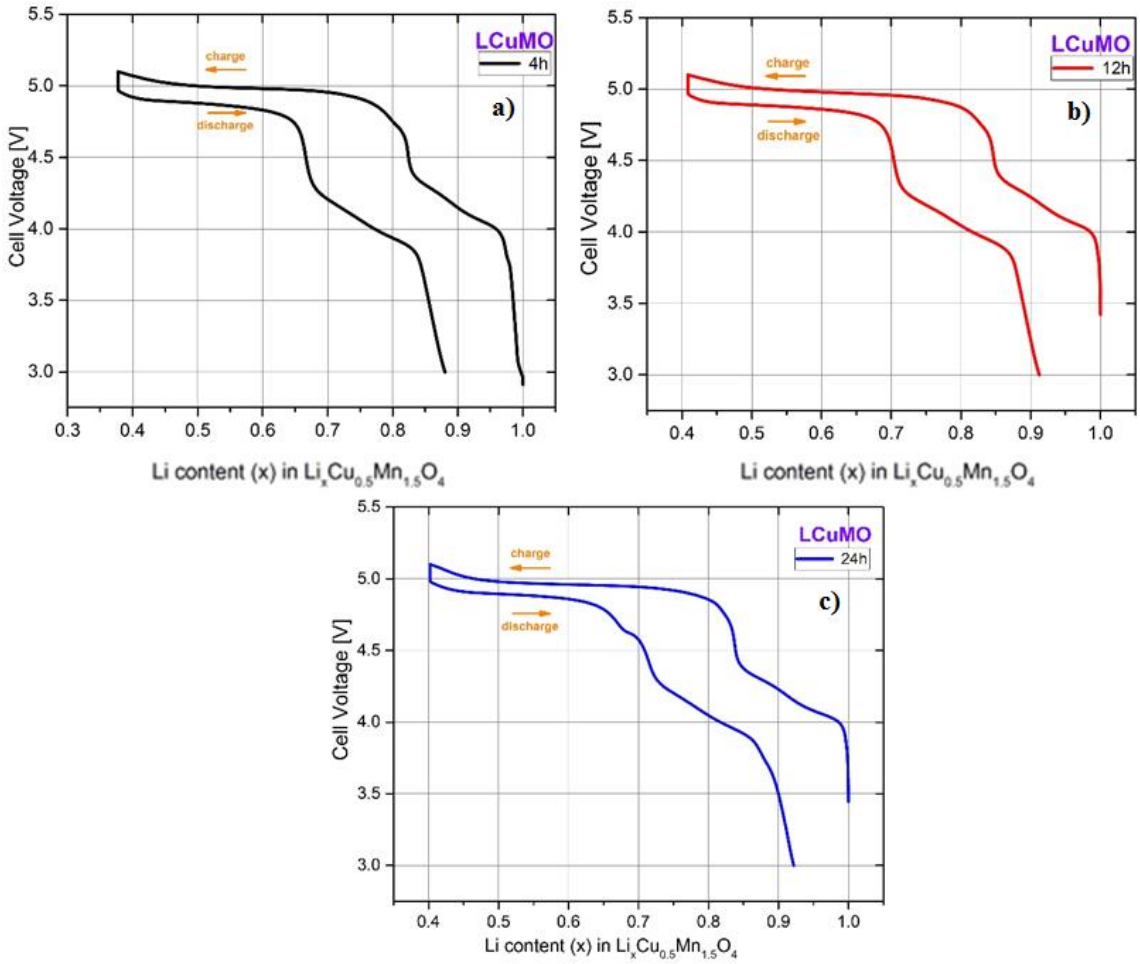

Figure 4.8 Cell voltage vs. Li content in the material curves of 1st cycle of the cathode materials LCuMO annealed at 600 °C in air of as prepared a) 4 h, b) 12 h and c) 24 h

The cycling stability results for the first 100 cycles of the LCuMO annealed at 600 °C in air for 4, 12 and 24 h cycled at C / 3.5 charge – discharge rate in the voltage interval 3 – 5.1 V are shown in Figure 4.9. Although the cathode material LCuMO annealed for 12 h has the highest first discharge capacity, it has the same capacity fading ratio (39.7 %) with the other materials which were annealed for 12 and 24 h.

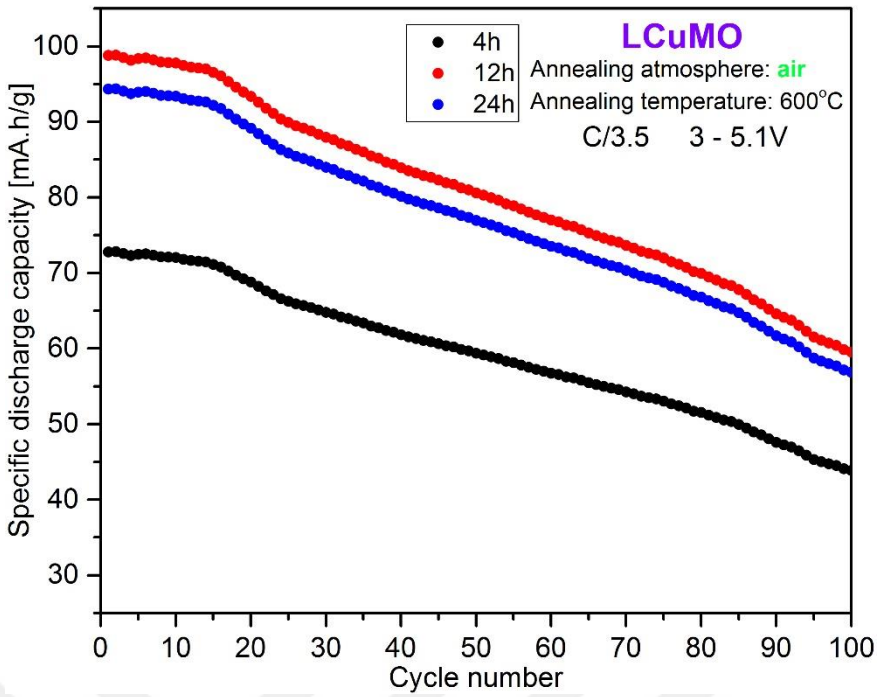

Figure 4.9 Specific discharge capacity vs. cycle number plots of the cathode materials LCuMO annealed at 600 °C in air for 4, 12 and 24 h

4.1.1.7 In Situ Investigations

The structural evolutions of the cathode material LCuMO, annealed at 600 °C for 4 h in air, during electrochemical cycling using synchrotron diffraction were studied.

The cell was cycled at a charge / discharge rate of C / 5 in the voltage range 2 – 5 V vs Li / Li^+. In the second cycle the cell was charged up to 4 V vs Li / Li^+ only. The voltage profile of this cathode material contains two flat plateaus in 5 V and 3 V regions, respectively. Moreover, the charge – discharge plateaus in 4 V region, which are usually attributed to the reaction Mn^{3+} / Mn^{4+} are visible. Whereas the plateau in the 5 V region results from the lithium extraction / insertion from / into the $LiCu_{0.5}Mn_{1.5}O_4$, the 3 V discharge plateau should be attributed to the insertion of the second Li into $LiCu_{0.5}Mn_{1.5}O_4$. Li content (which is denoted by x) in the $Li_xCu_{0.5}Mn_{1.5}O_4$ vs. cell voltage graph, which is shown inset of Figure 4.12, verifies the second lithium intercalation. Li contents in the cathode material at the beginning of 3 V region and at the end of discharge are determined as 0.8 and 1.74 moles, respectively.

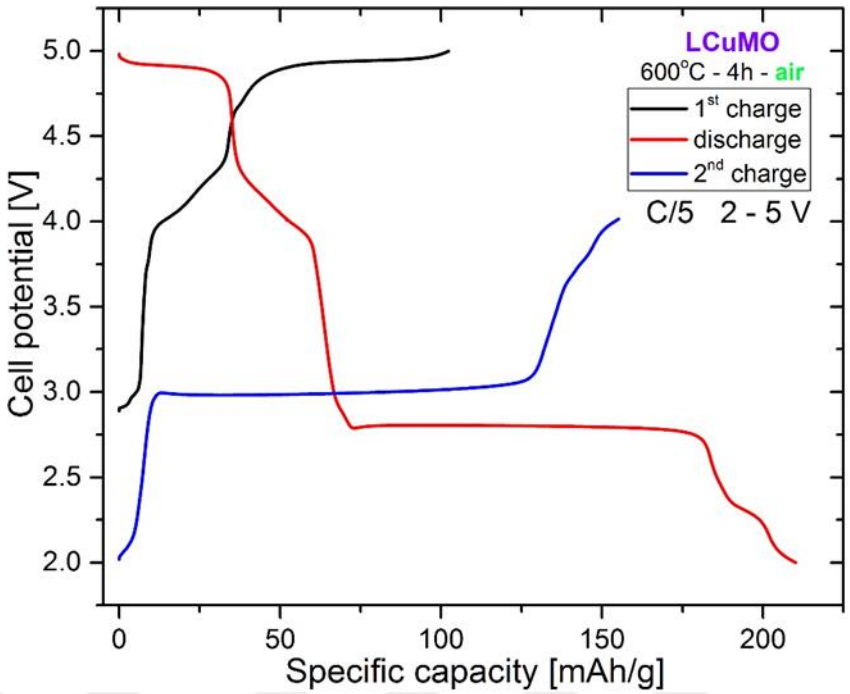

Figure 4.10 Voltage profile corresponding to the in situ synchrotron diffraction patterns for the cathode material LCuMO annealed at 600 °C for 4 h in air between 2 – 5 V cycled at C/5 charge – discharge rate

The structural evolution during electrochemical cycling process for the cathode material LCuMO annealed at 600 °C for 4 h in air are presented in Figure 4.11 for selected 2θ regions, where black, red and blue lines correspond to the 1st charge, discharge and 2nd charge, respectively. In the Figure 4.11, the reflections of the initial LCuMO (SG $Fd\bar{3}m$) cathode material appear at 9.61 and 10.04°. During charging the cell, the reflections shift to higher 2θ values, in accordance with a shrinkage of a unit cell upon lithium extraction (up to x = 0.29). After starting the discharge process, the reflections shift to lower 2θ values, in accordance with an expansion of a unit cell upon lithium insertion (up to x = 0.79) and afterwards the intensities of the reflections decrease and disappear (up to x = 1.55).

The presence of the second Li intercalation plateau at around 3 V region during discharge is associated with the first order transition ($LiCu_{0.5}Mn_{1.5}O_4 + Li^+ + e^- \rightleftharpoons Li_2Cu_{0.5}Mn_{1.5}O_4$), i.e. two phase reaction. Li insertion in to $LiCu_{0.5}Mn_{1.5}O_4$ results in a phase transformation from the cubic to tetragonal structure (called Jahn – Teller distortion), where Li ions occupy the 16c sites [20]. At the higher degree of lithiation (x = 1.38), the second $Li_2Cu_{0.5}Mn_{1.5}O_4$ phase appears with the $I4_1/amd$ space group.

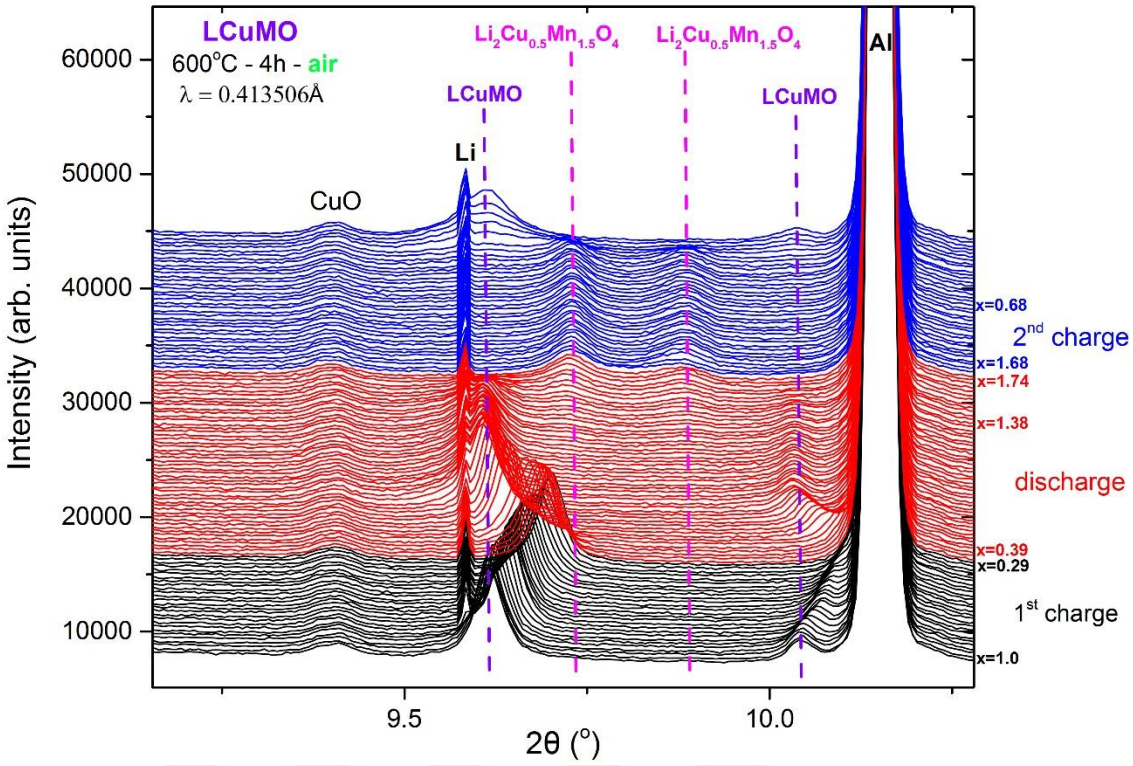

Figure 4.11 Selected 2θ regions of in situ synchrotron diffraction patterns of the cathode material LCuMO annealed at 600 °C for 4h in air

Rietveld refinement was carried out for the initial LCuMO cathode material, the last in situ diffraction pattern of the 1st charge and the first in situ diffraction pattern of the discharge and the results of the refinement with Li contents in the materials are presented in Table 4.3.

Table 4.3 Rietveld refinement results based on in situ synchrotron diffraction of the LCuMO annealed at 600 °C for 4 h in air cathode material

	Phase	Li content (x)	Cell parameter(s) [Å]
Initial	$Li_xCu_{0.5}Mn_{1.5}O_4$ $Cubic\ (Fd\bar{3}m)$	1	a = 8.1810(3)
End of 1st charge	$Li_xCu_{0.5}Mn_{1.5}O_4$ $Cubic\ (Fd\bar{3}m)$	0.29	a = 8.0755(2)
End of discharge	$Li_xCu_{0.5}Mn_{1.5}O_4$ $Tetragonal\ (I4_1/amd)$	1.74	a = 5.6890(5) c = 9.2581(5)

The shrinkage of the unit cell of the cubic phase at the end of the first charge is 0.97 % and the lattice expansion of the unit cell of the cubic phase during the discharge is 1.26 %.

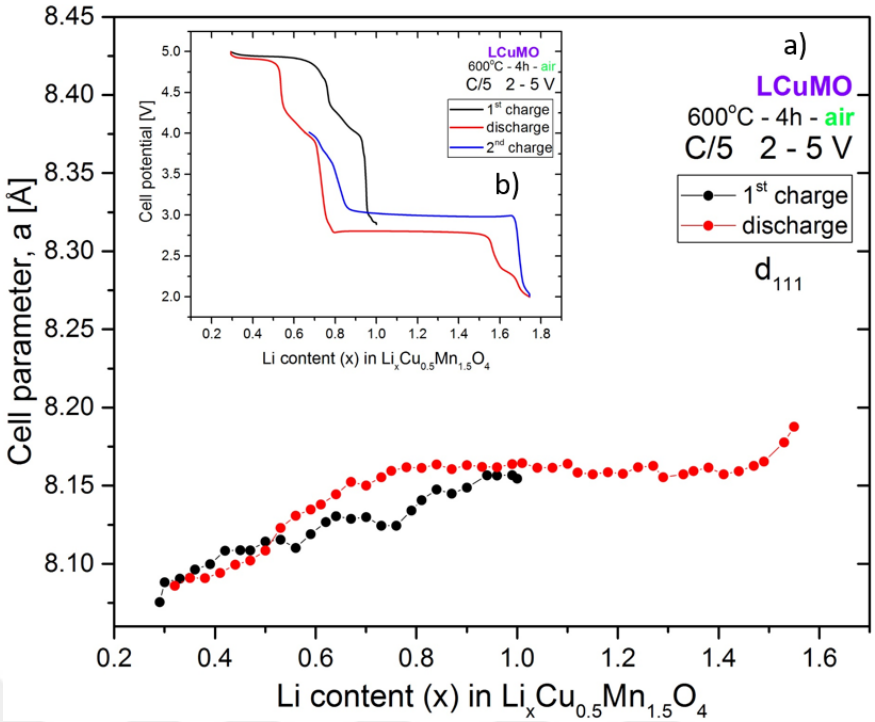

Figure 4.12 a) Cell parameters of the cubic spinel system vs. Li content in the cathode material LCuMO annealed at 600 °C 4 h in air, b) Cell potential vs. Li content in the cathode material cycled at the charge – discharge rate of C / 5 in a voltage range 2 – 5 V

4.1.1.8 The Influence of Annealing Temperature on Structural Characteristic

Figure 4.13 shows the XRD patterns for the LCuMO samples annealed at 600 °C, 750 °C and 900 °C for 4 h in air which are denoted by LCuMO–600°C–air, LCuMO–750°C–air and LCuMO–900°C–air, respectively. In addition to the main phase spinel structure (SG *Fd$\bar{3}$m*), the samples contain different ratios of CuO (SG *C12/c1*) respectively, fractions of CuO phase are 7.2, 6 and 5.7 % obtained at 600 °C, 750 °C and 900 °C. However, the materials annealed at 750 °C and 900 °C contain Li_2MnO_3 (SG *C12/m1*) admixture (respectively, 4.5 and 11.4 %). The integrated intensity ratio of the 400 / 311 reflections of the spinel phase decreases with increasing temperature. This decrease indicates increased amount of transition metal ions on the tetrahedral site (8a) [17].

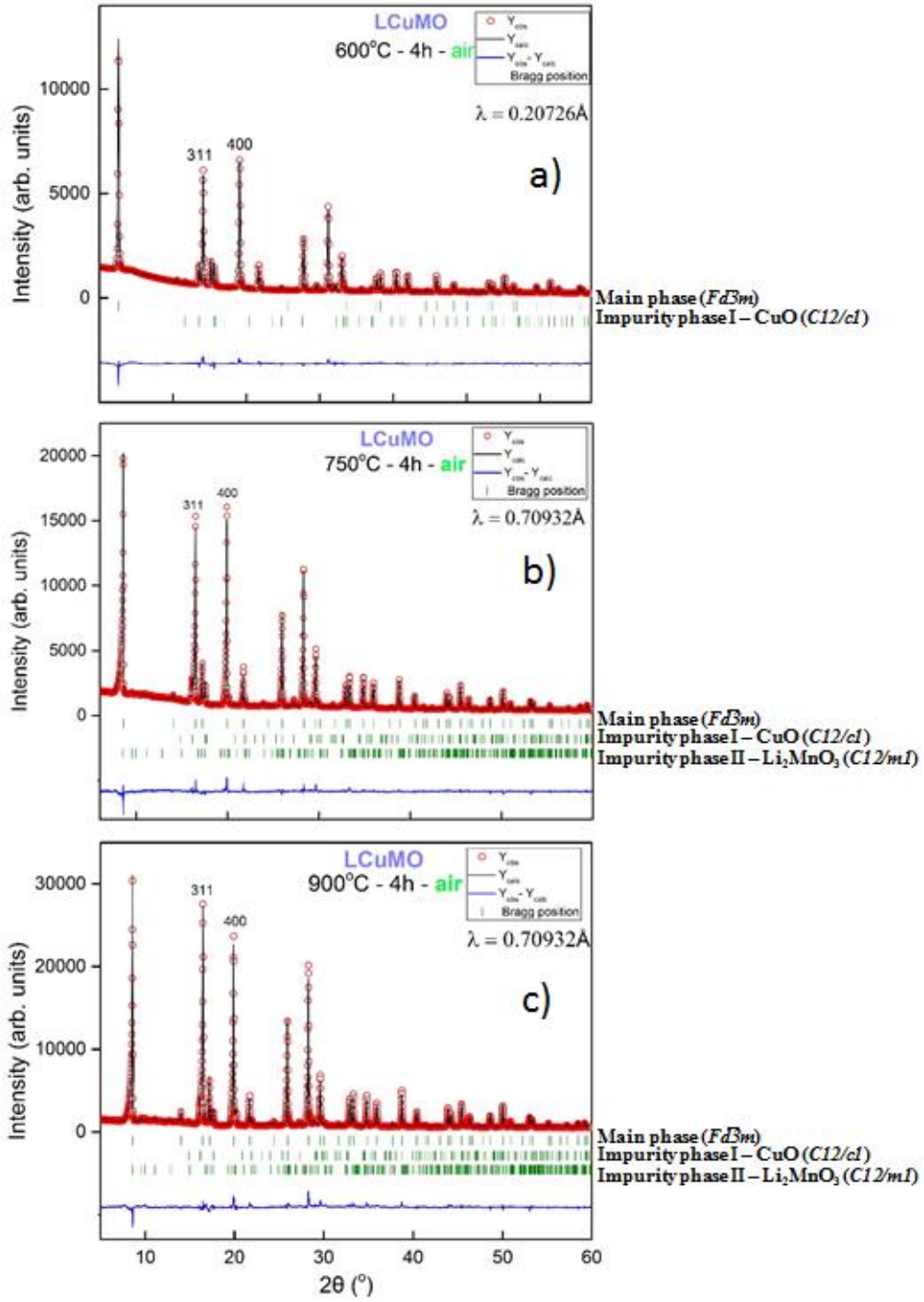

Figure 4.13 Rietveld refinement of diffraction patterns of as prepared a) LCuMO–600°C–air, b) LCuMO–750°C–air and c) LCuMO–900°C–air samples measured in 0.5 mm capillaries

The Rietveld refinement results of LCuMO–600°C–air, LCuMO–750°C–air and LCuMO–900°C–air samples are shown in Table 4.4. The amount of impurity phases in the samples and the amount of Cu on the tetrahedral site increase with the increasing annealing temperature. Furthermore, the unit cell of the spinel phase in the LCuMO–750°C–air sample has the smallest lattice parameter value.

Table 4.4 Rietveld refinement results of LCuMO–600°C–air, LCuMO–750°C–air and LCuMO–900°C–air samples

Annealing temperature of samples [°C]	Atomic site	x=y=z	a [Å]	Volume [Å^3]	Fraction of impurity phase [%]	Cu on the tetrahedral site (8a) [%]	Overall temperature factor (B_{ov})	R_{wp} [%]
600	Li_{8a} Cu_{8a} Mn_{16d} Cu_{16d} Li_{16d} O_{32e}	0.125 0.125 0.500 0.500 0.500 0.2636(5)	8.1810(3)	547(3)	7.2	3.6	0.70	7.9
750	Li_{8a} Cu_{8a} Mn_{16d} Cu_{16d} Li_{16d} O_{32e}	0.125 0.125 0.500 0.500 0.500 0.2630(1)	8.1955(2)	550(2)	10.5	7.1	0.25	10.3
900	Li_{8a} Cu_{8a} Mn_{16d} Cu_{16d} Li_{16d} O_{32e}	0.125 0.125 0.500 0.500 0.500 0.2620(3)	8.2152(1)	554(1)	17.1	17.5	0.20	11.6

4.1.1.9 The Influence of Annealing Temperature on the Cycling Stability and Electrochemical Characterization

The voltage profiles of LCuMO–600°C–air, LCuMO–750°C–air and LCuMO–900°C–air samples cycled at C / 3.5 charge – discharge rate for the 1st discharge are presented in Figure 4.14. The LCuMO–750°C–air exhibits the highest 1st discharge specific capacity. The Cu^{2+} contents in the LCuMO annealed at 600 °C, 750 °C and 900 °C, which are calculated from the capacity obtained in 5V region, are 0.291, 0.345 and 0.319 moles, respectively. Moreover, the Mn^{3+} content in the LCuMO annealed at 600 °C, 750 °C and 900 °C, which are calculated from the capacity obtained in 4V region, are 0.211, 0.244 and 0.227 moles, respectively.

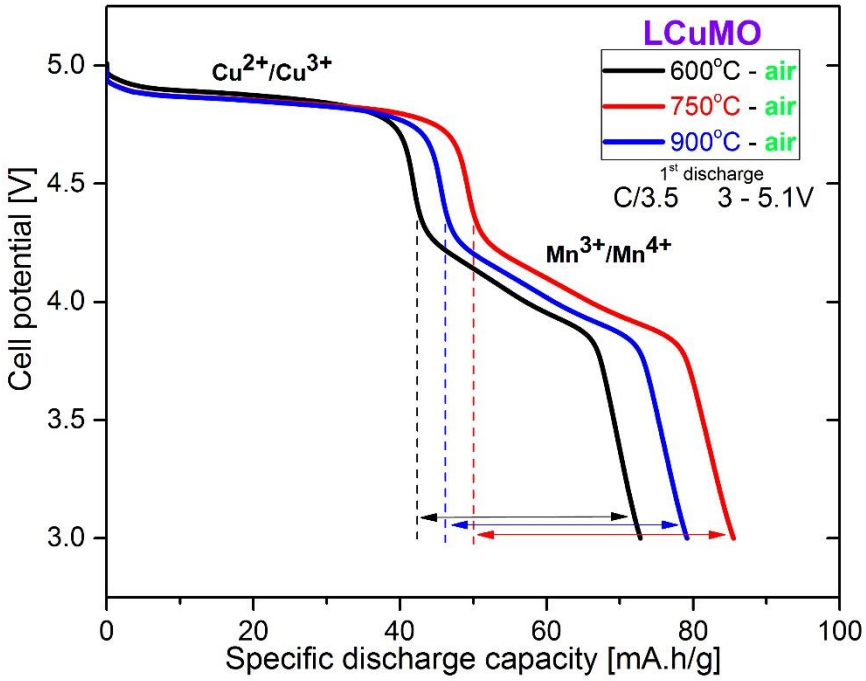

Figure 4.14 Cell potential vs. specific discharge capacity of 1st discharge of cathode materials LCuMO–600°C–air, LCuMO–750°C–air and LCuMO–900°C–air

The cycling stability results of the first 100 cycles of LCuMO–600°C–air, LCuMO–750°C–air and LCuMO–900°C–air samples cycled at C / 3.5 charge – discharge rate in the voltage window 3 – 5.1 V are shown in Figure 4.15 a). The capacity fading of all three materials is 39.7 % after 100 cycles.

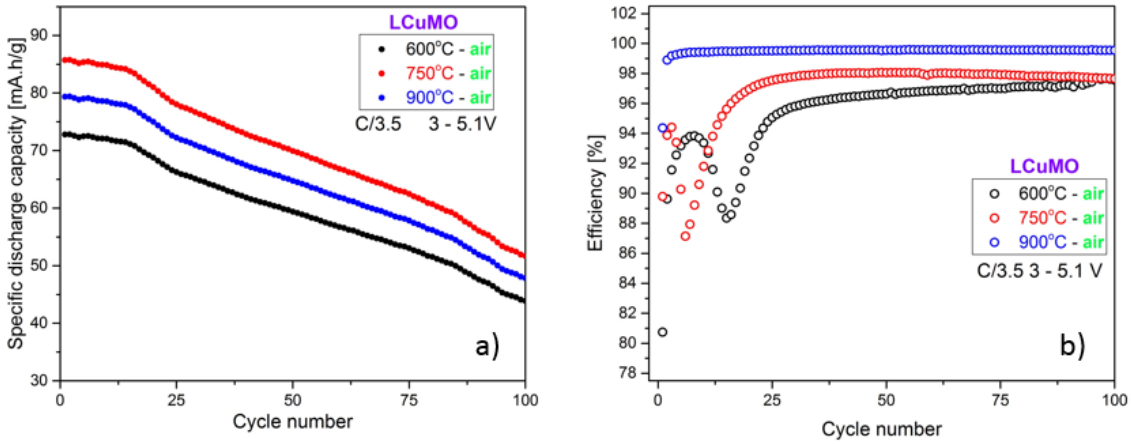

Figure 4.15 a) Specific discharge capacity vs. cycle number plots of cathode materials LCuMO–600°C–air, LCuMO–750°C–air and LCuMO–900°C–air cycled at C/3.5 rate between 3 – 5.1 V, b) Coulombic efficiencies vs. cycle number plots for the cycling mentioned in a)

Figure 4.15 b) shows the coulombic efficiencies of LCuMO–600°C–air, LCuMO–750°C–air and LCuMO–900°C–air samples. The LCuMO–900°C–air sample has the highest first

cycle coulombic efficiency and there is also that the coulombic efficiency of this material increases and reaches ~99.5 % during the following cycles.

4.1.1.10 X – Ray Absorption Near Edge Structure (XANES) Analysis of the Annealed LCuMO at Varying Temperature

To study the influence of annealing temperature on the oxidation state of Mn and Cu, X – ray absorption near edge (XANES) spectra were analyzed for LCuMO–600°C–air, LCuMO–750°C–air and LCuMO–900°C–air samples. By comparing the XANES region of the Mn K – edge of all three samples with the standard MnO_2, it might be concluded that the Mn in all three systems predominantly exists as Mn^{4+} (see Figure 4.16).

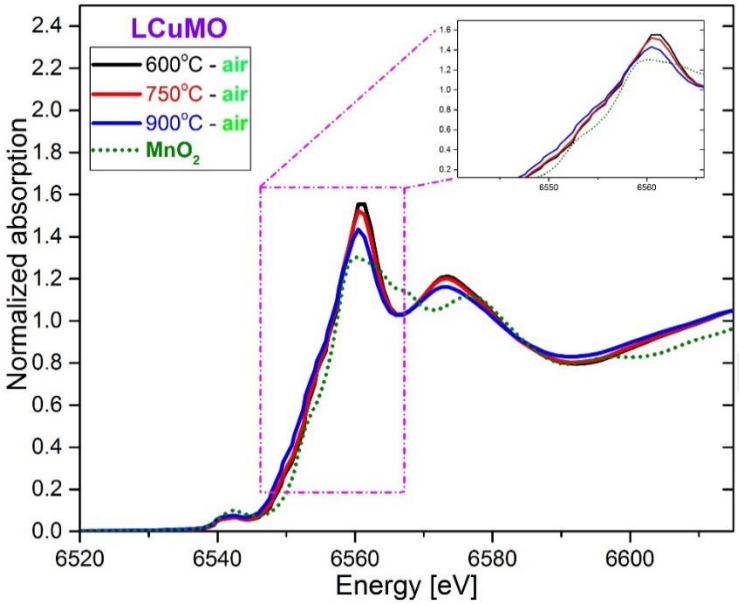

Figure 4.16 XANES of Mn K – edge, for LCuMO–600°C–air, LCuMO–750°C–air and LCuMO–900°C–air samples, as well as for the reference material MnO_2

XANES of Cu K – edge plots of LCuMO–600°C–air, LCuMO–750°C–air and LCuMO–900°C–air samples with the references materials (Cu_2O and CuO) are shown in Figure 4.17. By comparing the XANES region of the Cu K – edge of all three samples with the references, it might be concluded that the Cu in all three systems predominantly exists as Cu^{2+} (see Figure 4.17).

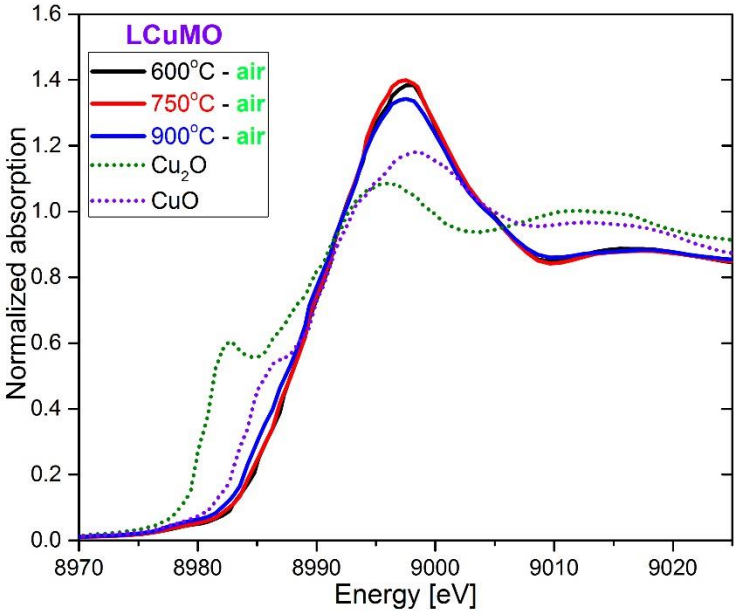

Figure 4.17 XANES of Cu K – edge, for LCuMO–600°C–air, LCuMO–750°C–air and LCuMO–900°C–air samples, as well as for the reference materials Cu_2O and CuO

4.1.2 Results of Annealed $LiCu_{0.5}Mn_{1.5}O_4$ under O_2 Cathode Materials

In this study, the $LiCu_{0.5}Mn_{1.5}O_4$ (LCuMO) precursors obtained were annealed at the different temperatures which were 600 °C, 750 °C and 900 °C under O_2 atmosphere. The results obtained for the cathode materials are discussed in the following sections.

4.1.2.1 Structural Characterization

Figure 4.18 shows XRD patterns for the LCuMO samples annealed at 600 °C, 750 °C and 900 °C for 4 h under O_2 which are denoted by LCuMO–600°C–O_2, LCuMO–750°C–O_2 and LCuMO–900°C–O_2, respectively. In addition the main phase spinel structure (SG $Fd\bar{3}m$), the LCuMO–600°C–O_2, LCuMO–750°C–O_2 and LCuMO–900°C–O_2 samples contain different ratio of CuO (6.6, 5.6 and 5.3 %, respectively) and Li_2MnO_3 (1.1, 2.6 and 3.8 %, respectively). The integrated intensity ratio of 400 / 311 reflection of the spinel phase and the amount of transition metal ions on the tetrahedral site are in inverse proportion. In Figure 4.18, the ratio of 400 / 311 reflection decreases with the increasing annealing temperature, hence the number of Cu ions on the tetrahedral site increase.

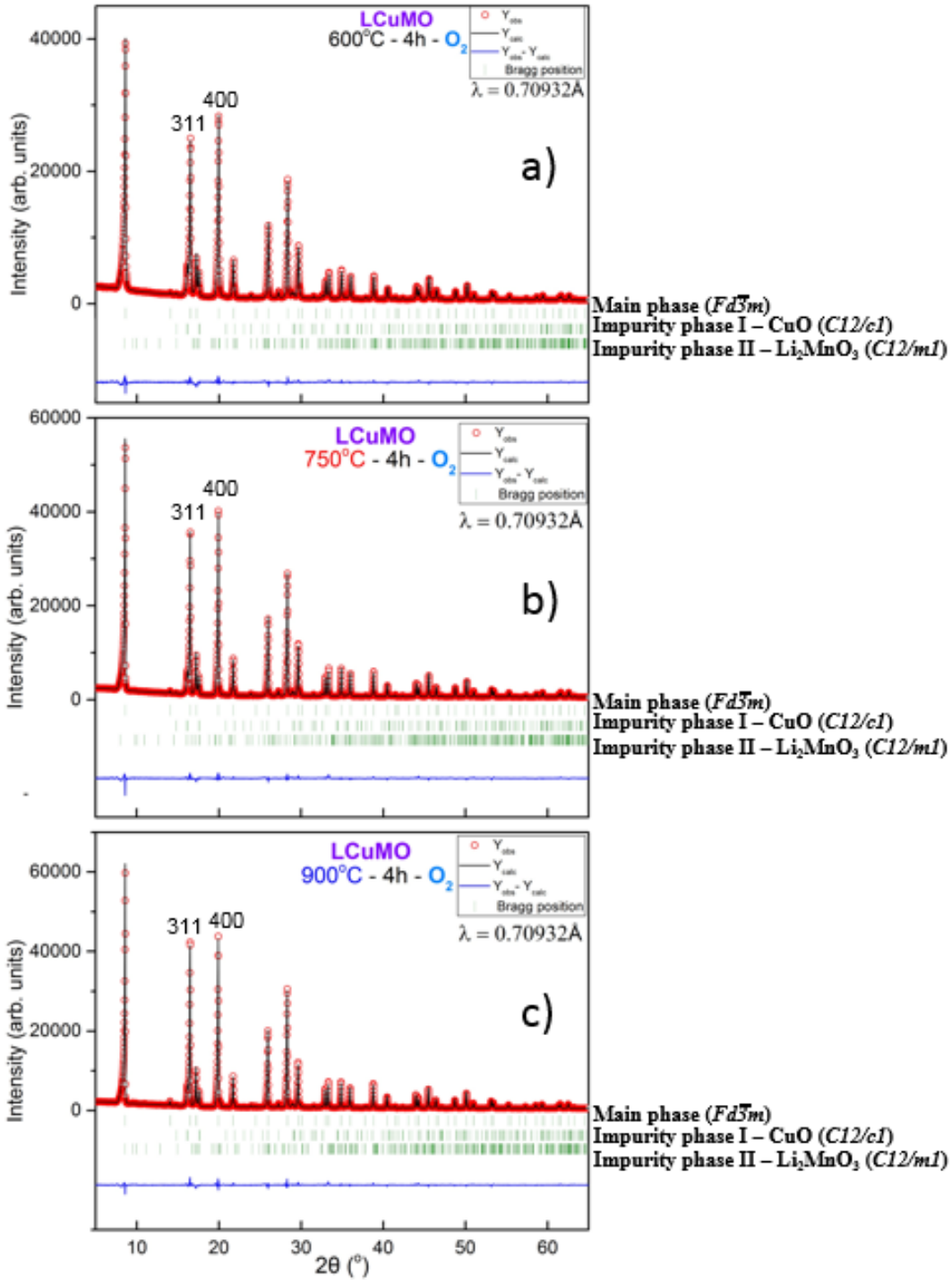

Figure 4.18 Rietveld refinement of diffraction patterns of as prepared a) LCuMO–600°C–O_2, b) LCuMO–750°C–O_2 and c) LCuMO–900°C–O_2 samples measured in 0.5 mm capillaries

Rietveld refinement results of LCuMO–600°C–O_2, LCuMO–750°C–O_2 and LCuMO–900°C–O_2 samples are shown in Table 4.5. The lattice parameter value of the spinel phase, the impurity phase fraction in the samples and the occupation ratio of Cu on the tetrahedral site increase with the increasing annealing temperature.

Table 4.5 Rietveld refinement results of LCuMO–600°C–O_2, LCuMO–750°C– O_2 and LCuMO–900°C–O_2 samples

Annealing temperature of samples [°C]	Atomic site	x=y=z	a [Å]	Volume [Å^3]	Fraction of impurity phase [%]	Cu on the tetrahedral site (8a) [%]	Overall temperature factor (B_{ov})	R_{wp} [%]
600	Li_{8a} Cu_{8a} Mn_{16d} Cu_{16d} Li_{16d} O_{32e}	0.125 0.125 0.500 0.500 0.500 0.2636(2)	8.1871(1)	548(1)	7.7	1.6	0.39	7.16
750	Li_{8a} Cu_{8a} Mn_{16d} Cu_{16d} Li_{16d} O_{32e}	0.125 0.125 0.500 0.500 0.500 0.2638(1)	8.1926(1)	549(1)	8.2	3.2	0.36	7.47
900	Li_{8a} Cu_{8a} Mn_{16d} Cu_{16d} Li_{16d} O_{32e}	0.125 0.125 0.500 0.500 0.500 0.2640(1)	8.2008(3)	551(3)	9.1	7.5	0.33	7.85

4.1.2.2 Electrochemical Characterization

Voltage profiles of LCuMO–600°C–O_2, LCuMO–750°C–O_2 and LCuMO–900°C–O_2 samples cycled at C / 3.5 rate between 3 – 5.1 V for the 1st discharge are shown in Figure 4.19. The LCuMO–900°C–O_2 sample exhibits the highest 1st specific discharge capacity. The Mn^{3+} content in the LCuMO annealed at 600 °C, 750 °C and 900 °C under O_2 samples, which are calculated from the capacity obtained in 4 V region, are 0.189, 0.140 and 0.201 moles, repectively.

The cell voltage vs. Li content in the material curves of LCuMO–600°C–O_2, LCuMO–750°C–O_2 and LCuMO–900°C–O_2 samples cycled at C / 3.5 rate between 3 – 5.1 V for the 1st cycle are presented in Figure 4.20. At the end of the 1st charge, Li contents of the annealed 600 °C, 750 °C and 900 °C materials are 0.43, 0.44 and 0.45 and at the end of the fist cycle, the ratio of the Li content fades from the materials are 8, 7 and 7 %, respectively.

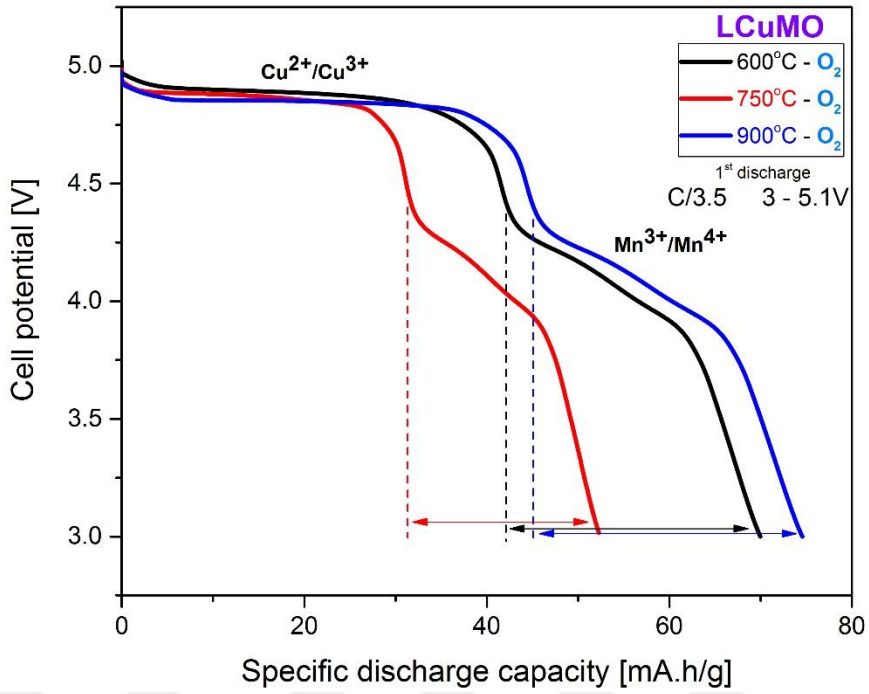

Figure 4.19 Cell potential vs. specific discharge capacity of 1st discharge of cathode materials LCuMO–600°C–O_2, LCuMO–750°C–O_2 and LCuMO–900°C–O_2

The cycling stability results of the first 100 cycles of LCuMO–600°C–O_2, LCuMO–750°C–O_2 and LCuMO–900°C–O_2 samples are shown in Figure 4.21 a). The cycling stability results show that the capacity fading of all three samples is 33.2 % after 100 cycles.

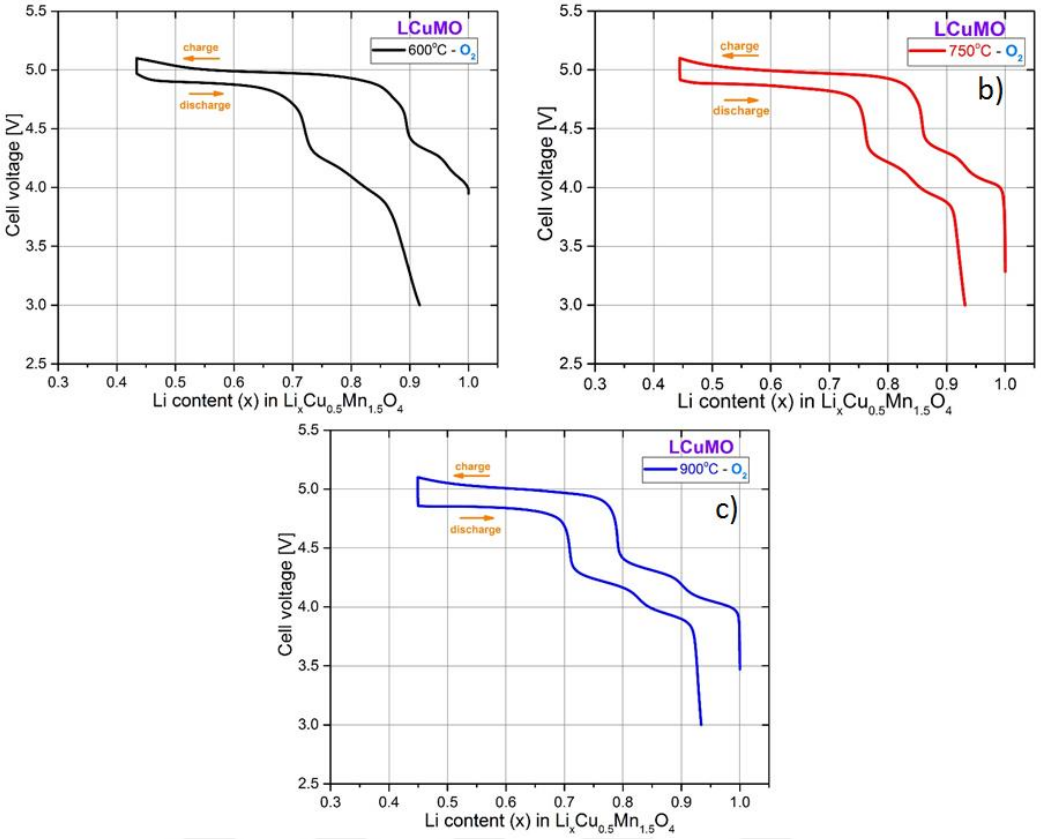

Figure 4.20 Cell voltage vs. Li content in the material curves of 1st cycle of as prepared a) LCuMO–600°C–O_2, b) LCuMO–750°C–O_2 and c) LCuMO–900°C–O_2

Figure 4.21 b) shows that the LCuMO–900°C–O_2 sample has the highest first coulombic efficiency. The coulombic effiencies of LCuMO–600°C–O_2, LCuMO–750°C–O_2 and LCuMO–900°C–O_2 samples increse and reach ~97.7, 97 and 97.6 %, respectively, during the following cycles.

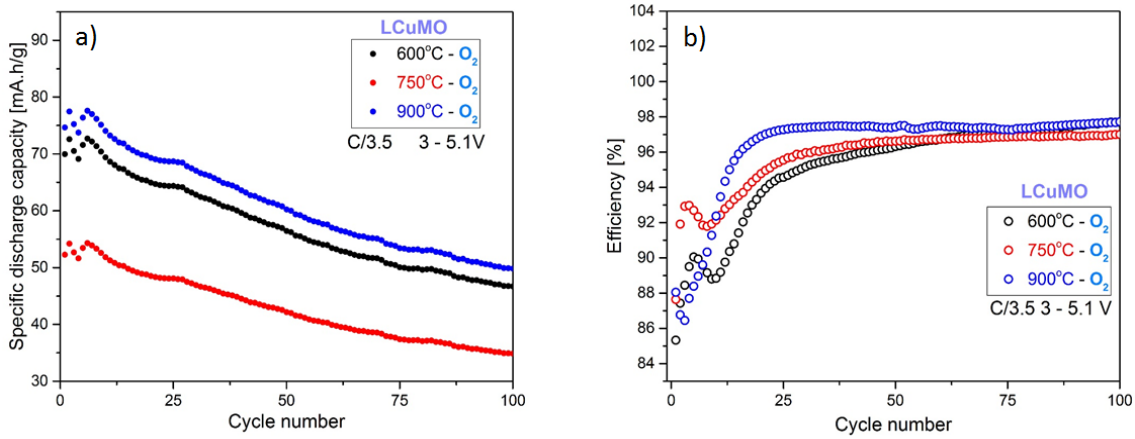

Figure 4.21 a) Specific discharge capacity vs. cycle number plots of LCuMO–600°C–O_2, LCuMO–750°C–O_2 and LCuMO–900°C–O_2 cathode materials cycled at C/3.5 rate between 3 – 5.1 V, b) Coulombic efficiencies vs. cycle number plots for cycling mentioned in a)

4.1.3 Structural Characterization of the $LiCu_{0.5}Mn_{1.5}O_4$ Samples Annealed under Argon

In this study, the $LiCu_{0.5}Mn_{1.5}O_4$ (LCuMO) precursors obtained were annealed at different temperatures which were 600 ^{o}C, 750 ^{o}C and 900 ^{o}C under Argon atmosphere.

Table 4.6 Rietveld refinement result of the LCuMO annealed at 600 ^{o}C for 4 h under Argon atmosphere cathode material

Annealing temperature of samples [^{o}C]	Atomic site	x=y=z	a [Å]	Volume [Å^3]	Fraction of impurity phase [%]	Cu on the tetrahedral site (8a) [%]	Overall temperature factor (B_{ov})	R_{wp} [%]
600	Li_{8a} Cu_{8a} Mn_{16d} Cu_{16d} Li_{16d} O_{32e}	0.125 0.125 0.500 0.500 0.500 0.2630(2)	8.2288(4)	557(4)	14.5	11.8	0.28	7.59

XRD patterns of the LCuMO annealed at 600 ^{o}C, 750 ^{o}C and 900 ^{o}C for 4 h under Argon atmosphere cathode materials are shown in Figure 4.22 which includes the Bragg positons (as vertical green mark) of the main phase LCuMO (SG $Fd\bar{3}m$), one of the impurity phase Li_2MnO_3 (SG *C12/m1*) and the second impurity phase CuO (SG *C12/c1*). The characteristic reflections of the main phase (i.e. the 111, 311, 400 reflections), which are emphasized in Figure 4.22, disappear with the increasing annealing temperature, hence, the Rietveld refinement analysis was carried out only for the cathode material LCuMO annealed at 600 ^{o}C for 4 h under Argon atmosphere (see Table 4.6 for additional details). The cell parameter for the spinel phase are much higher for Ar – annealed samples compared to the samples prepared in air and oxygen. This may indicate higher degree of oxygen deficiency, although in view of higher amount of the impurity phase the different stoichiometry of the spinel phase (Cu / Mn ratio) can not be excluded.

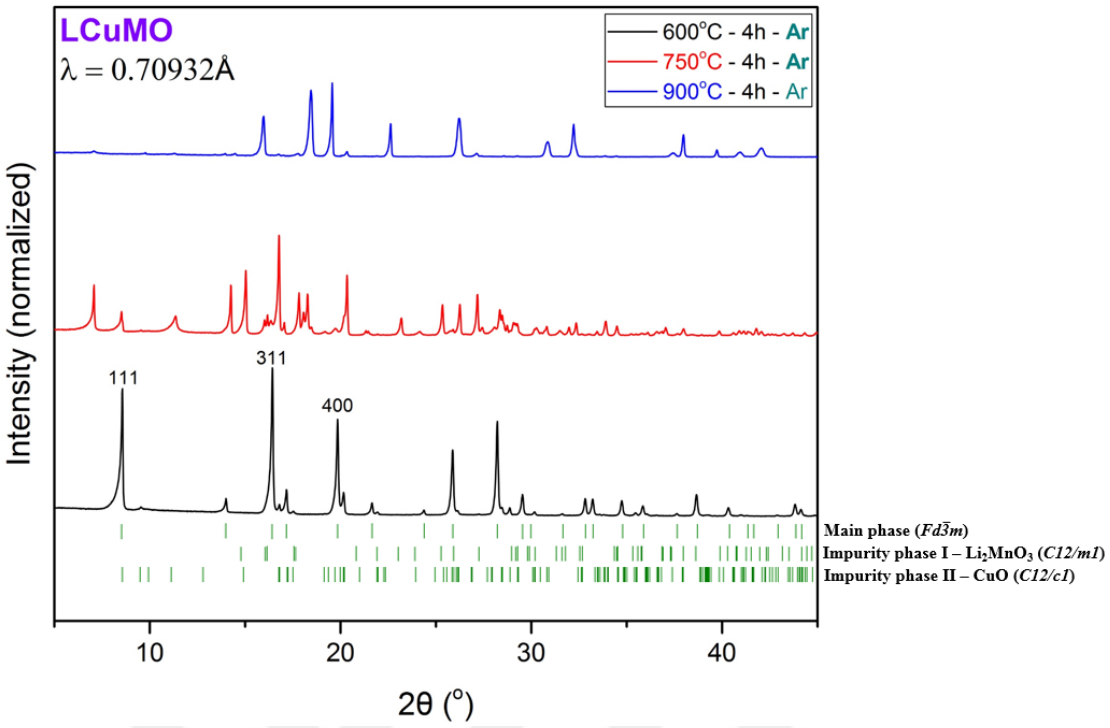

Figure 4.22 XRD patterns of the LCuMO annealed at 600 °C, 750 °C and 900 °C for 4 h under Argon atmosphere cathode materials

4.2 $LiNi_{0.25}Cu_{0.25}Mn_{1.5}O_4$ High Voltage Spinel Cathode Material

4.2.1 Results of Annealed $LiNi_{0.25}Cu_{0.25}Mn_{1.5}O_4$ in Air Cathode Materials

In this study, the $LiNi_{0.25}Cu_{0.25}Mn_{1.5}O_4$ (LNCuMO) precursors obtained were annealed at different temperatures which were 600 °C, 750 °C and 900 °C in air. Detailed discussions will be given in the following sections.

4.2.1.1 Structural Characterization

Figure 4.23 shows the Rietveld refinement of diffraction patterns for the LNCuMO annealed at 600 °C, 750 °C and 900 °C for 4 h in air samples which are denoted by LNCuMO–600°C–air, LNCuMO–750°C–air and LNCuMO–900°C–air, respectively. In addition to the main phase (SG $Fd\bar{3}m$), the samples involve different ratios of CuO (6.6, 5.6 and 5.3 %, respectively) and Li_2MnO_3 (1.1, 2.6 and 3.8, respectively). Moreover, according to the integrated intensity ratio of the 400 / 311 reflections of the main phase, the number of the transition metal ions (i.e. Cu ions) on the tetrahedral site increases with the increasing annealing temperature.

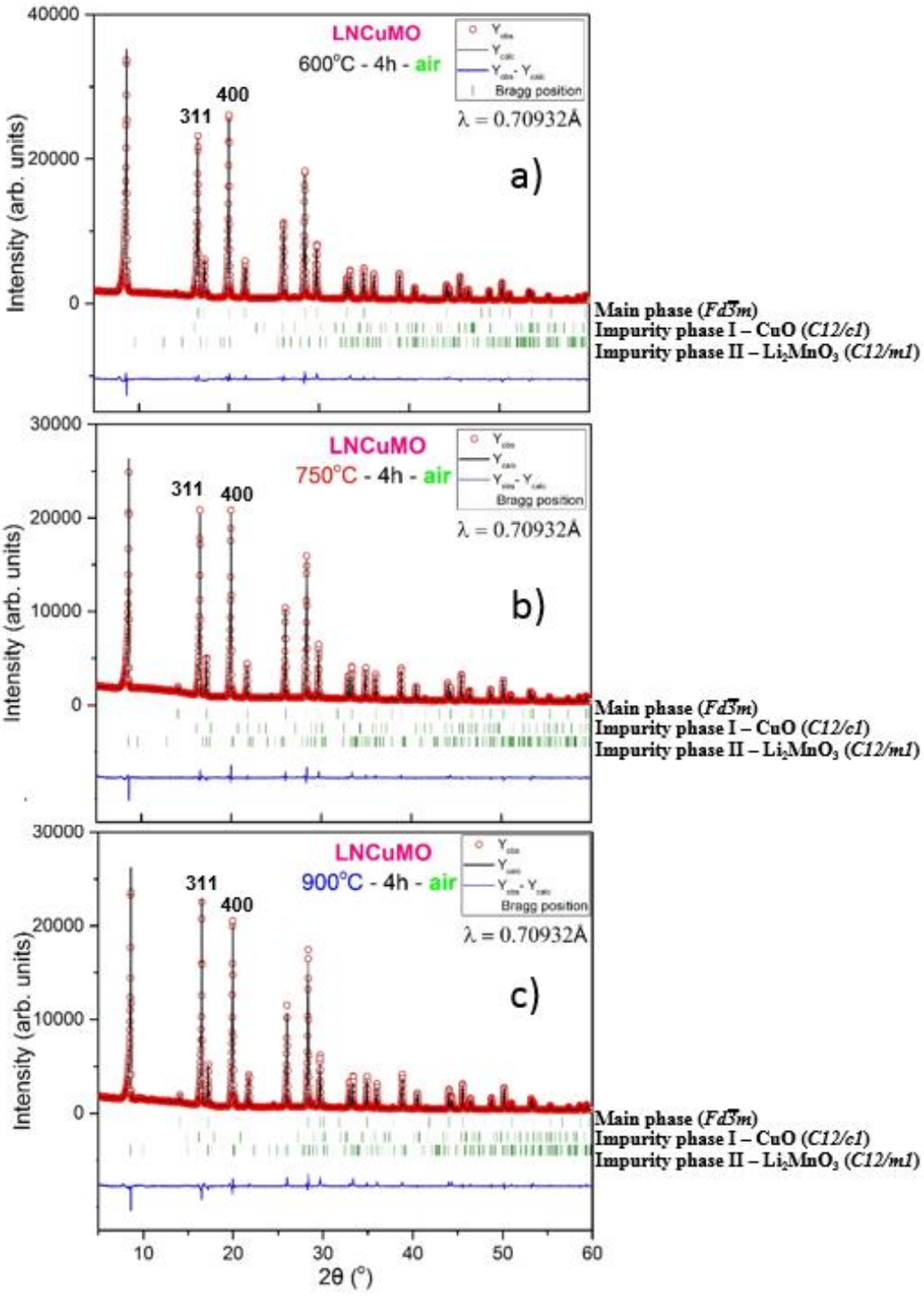

Figure 4.23 Rietveld refinement of diffraction patterns of as prepared cathode materials a) LNCuMO–600°C–air, b) LNCuMO–750°C–air and c) LNCuMO–900°C–air measured in 0.5 mm capillaries

Table 4.7 shows the additional details about the Rietveld refinement results of LNCuMO–600°C–air, LNCuMO–750°C–air and LNCuMO–900°C–air samples. The lattice parameter value of the main phase, the impurity phase ratio in the samples and the

occupation of Cu on the tetrahedral site increase with the increasing annealing temperature.

Table 4.7 Rietveld refinement results of LNCuMO–600°C–air, LNCuMO–750°C–air and LNCuMO–900°C–air samples

Annealing temperature of samples [°C]	Atomic site	x=y=z	a [Å]	Volume [Å^3]	Fraction of impurity phase [%]	Cu on the tetrahedral site (8a) [%]	Overall temperature factor (B_{ov})	R_{wp} [%]
600	Li_{8a} Cu_{8a} Mn_{16d} Ni_{16d} Cu_{16d} Li_{16d} O_{32e}	0.125 0.125 0.500 0.500 0.500 0.500 0.2633(2)	8.1741(1)	546(1)	7.7	1.6	0.15	8.63
750	Li_{8a} Cu_{8a} Mn_{16d} Ni_{16d} Cu_{16d} Li_{16d} O_{32e}	0.125 0.125 0.500 0.500 0.500 0.500 0.2630(2)	8.1850(1)	548(1)	8.2	3.2	0.11	9.93
900	Li_{8a} Cu_{8a} Mn_{16d} Ni_{16d} Cu_{16d} Li_{16d} O_{32e}	0.125 0.125 0.500 0.500 0.500 0.500 0.2620(2)	8.1946(4)	550(4)	9.1	7.5	0.15	12.1

4.2.1.2 Morphology Studies

SEM images of LNCuMO–precursor, powders of LNCuMO–600°C–air and LNCuMO–750°C–air are presented in Figure 4.24. The images were taken in secondary electron mode with an acceleration voltage of 10 kV. In contrast to the LNCuMO–precursor (a) and LNCuMO–600°C–air (b), LNCuMO–750°C–air (c) sample exhibits much bigger particle size, hence, it can be concluded that the increasing annealing temperature beyond 600 °C enlarges the particle size of LNCuMO material.

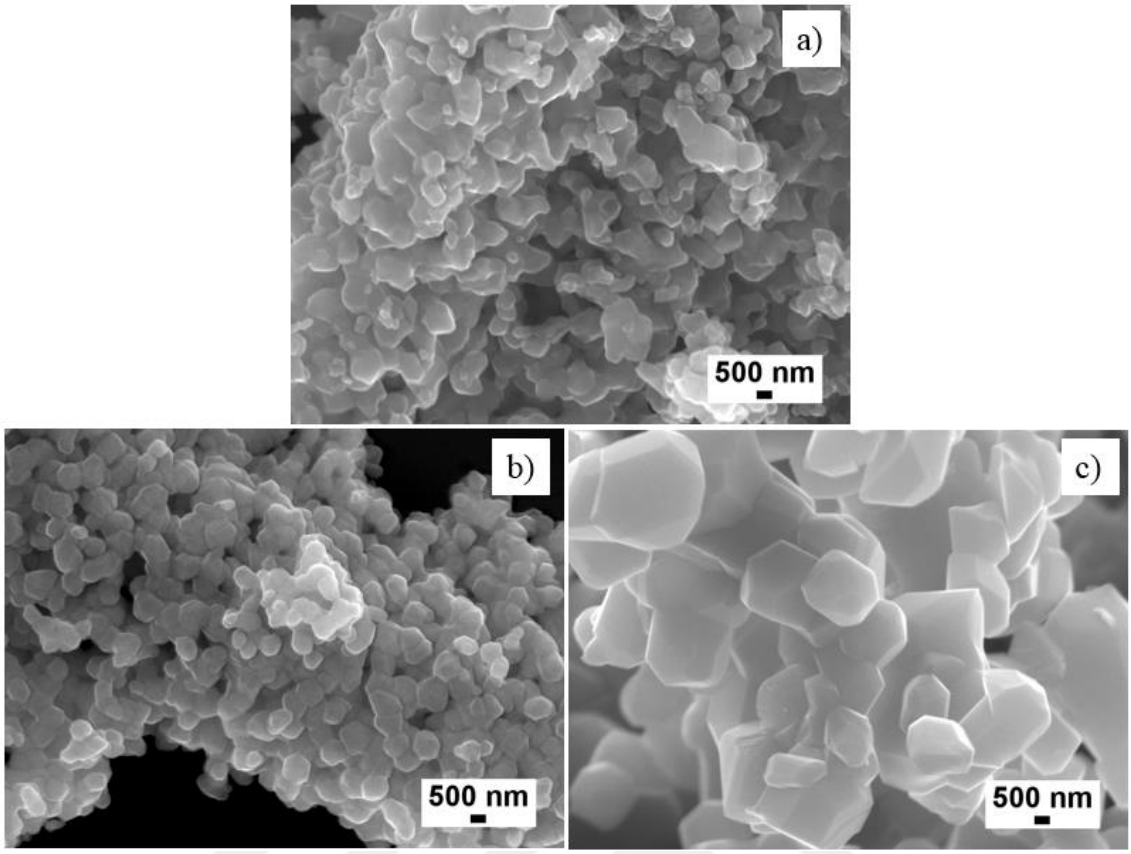

Figure 4.24 SEM images of as prepared powders a) LNCuMO–precursor, b) LNCuMO–600°C–air and c) LNCuMO–750°C–air

4.2.1.3 Cycling Voltammetry

Figure 4.25 shows that the cycling voltammograms of 1st and 5th cycles of the LNCuMO annealed at 600 ^{o}C for 4 h in air cycled between 3 – 5.3 V with a scan rate of 0.15 mVs^{-1}. The larger electrochemical activity during discharge at around 4 V which is attributed to the Mn^{3+} / Mn^{4+} redox couple. The two peaks in the region 4.4 – 5 V during oxidation and reduction are related to the Ni^{2+} / Ni^{4+} and Cu^{2+} / Cu^{3+} redox couples [25]. The onset of the electrolyte oxidation was noted at 5.15 V.

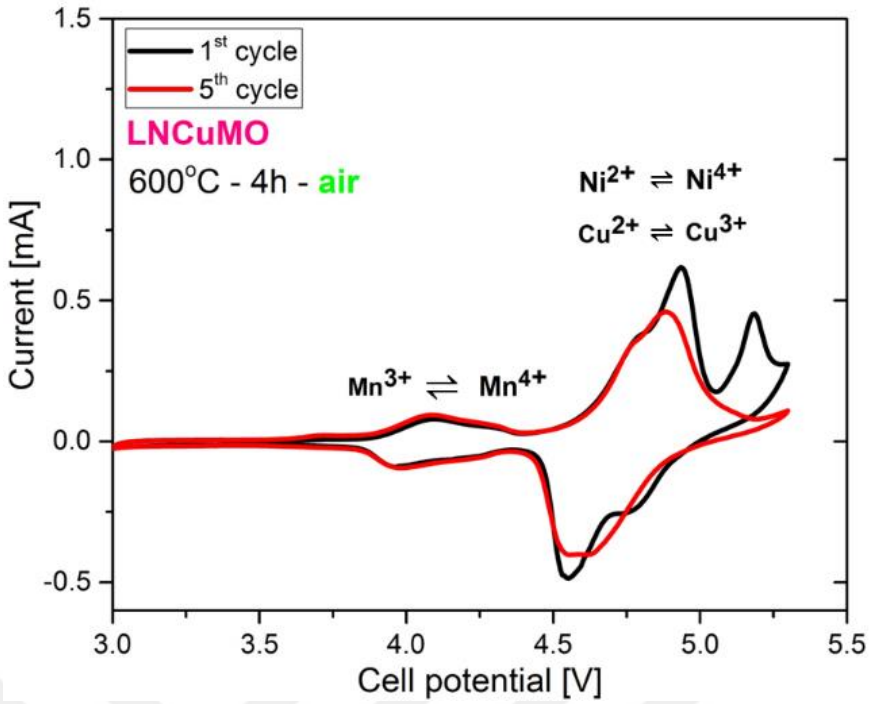

Figure 4.25 Cycling voltammograms of 1st and 5th cycles of cathode material LNCuMO–600°C–air with the scan rate of 0.15 mVs^{-1} in a voltage range 3 – 5.3 V

4.2.1.4 Electrochemical Characterization

Figure 4.26 shows the voltage profile of the LNCuMO samples annealed at 600 °C, 750 °C and 900 °C for 4 h in air which are denoted by LNCuMO–600°C–air, LNCuMO–750°C–air and LNCuMO–900°C–air, respectively. The materials were cycled at C / 3.5 rate between 3 – 5.1 V. The highest specific discharge capacity of 1st discharge belongs to LNCuMO–750°C–air sample. The Mn^{3+} content in the LNCuMO annealed at 600 °C, 750 °C and 900 °C, which are calculated from the capacity obtained 4 V region, are 0.173, 0.182 and 0.146 moles, respectively.

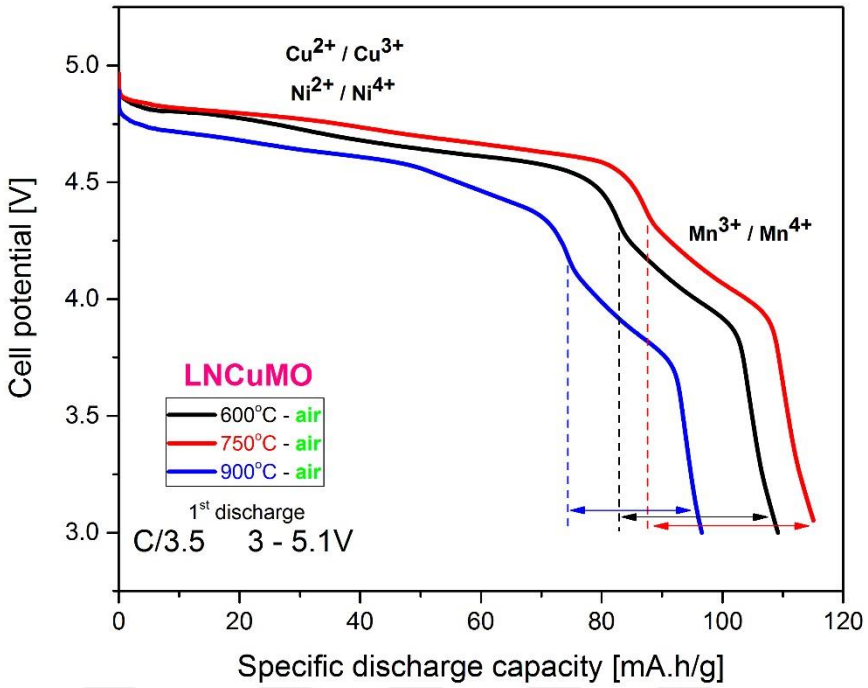

Figure 4.26 Cell voltage vs. specific discharge capacity of 1st discharge of cathode materials LNCuMO– 600°C–air, LNCuMO– 750°C–air and LNCuMO– 900°C–air

Figure 4.27 presents the sample curves of cell voltage vs. Li content in the material of LNCuMO–600°C–air, LNCuMO–750°C–air and LNCuMO–900°C–air cycled at C / 3.5 charge – discharge rate between 3 – 5.1 V for the 1st cycle. Although LNCuMO–600°C–air sample succeeds to transfer all Li content from its structure at the end of 1st charge, it succeeds to withdraw 72 % of the Li content. Furthermore, at the end of 1st discharge the Li contents of the LNCuMO samples annealed at 750 °C and 900 °C are 0.14 and 0.25 and at the end of first cycle, the ratio of the Li content of the materials are 8 and 7 %, respectively.

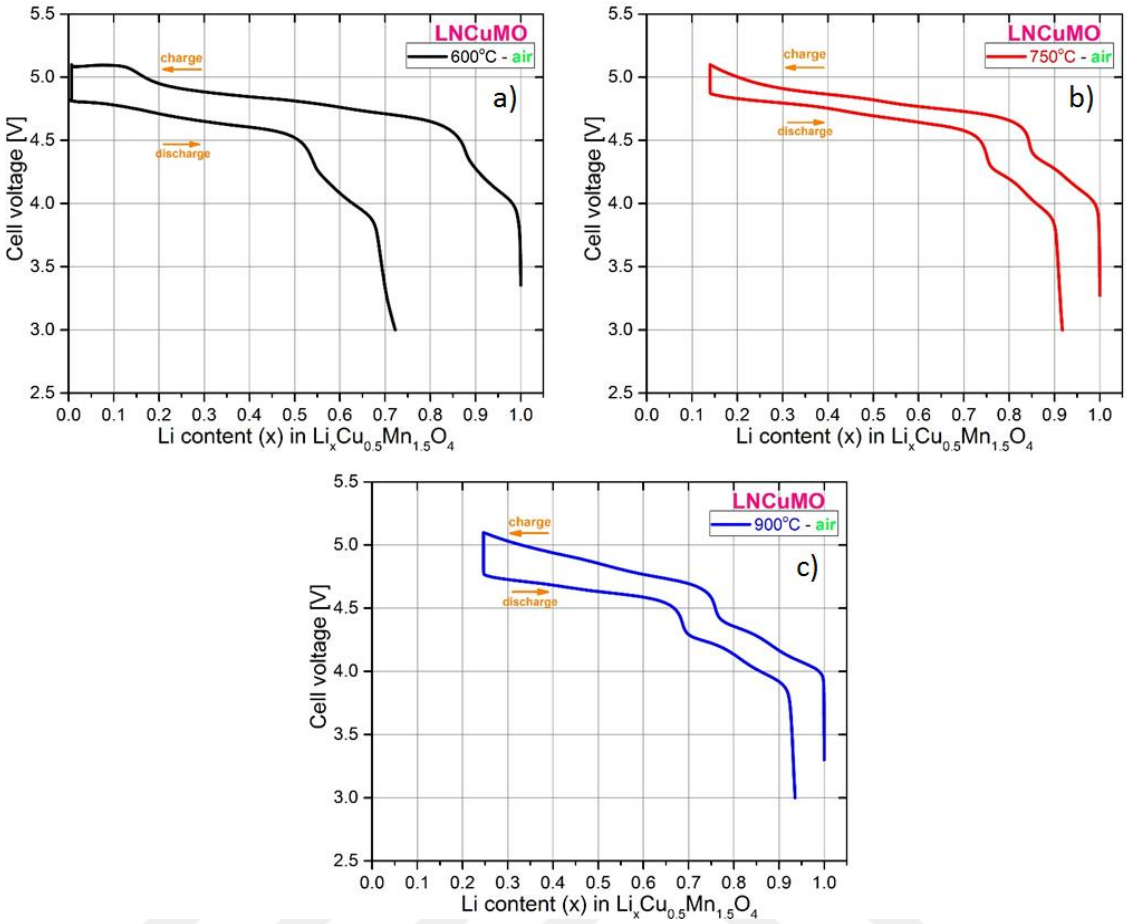

Figure 4.27 Cell voltage vs. Li content in the material curves of 1st cycle of as prepared a) LNCuMO–600°C–air, b) LNCuMO–750°C–air and c) LNCuMO–900°C–air

The cycling stability results of the first 100 cycles of the samples LNCu<<MO–600°C–air, LNCuMO–750°C–air and LNCuMO–900°C–air are presented in Figure 4.28 a). Corresponding to the cycling stability results, the capacity fading of all three samples is 56.3 %.

Figure 4.28 b) shows that the LNCuMO–900°C–air sample has the highest first coulombic efficiency. The coulombic efficiencies of samples LNCuMO–600°C–air, LNCuMO–750°C–air and LNCuMO–900°C–air increase and reach ~98.3, 97.7 and 98.5 %, respectively, during the following cycles.

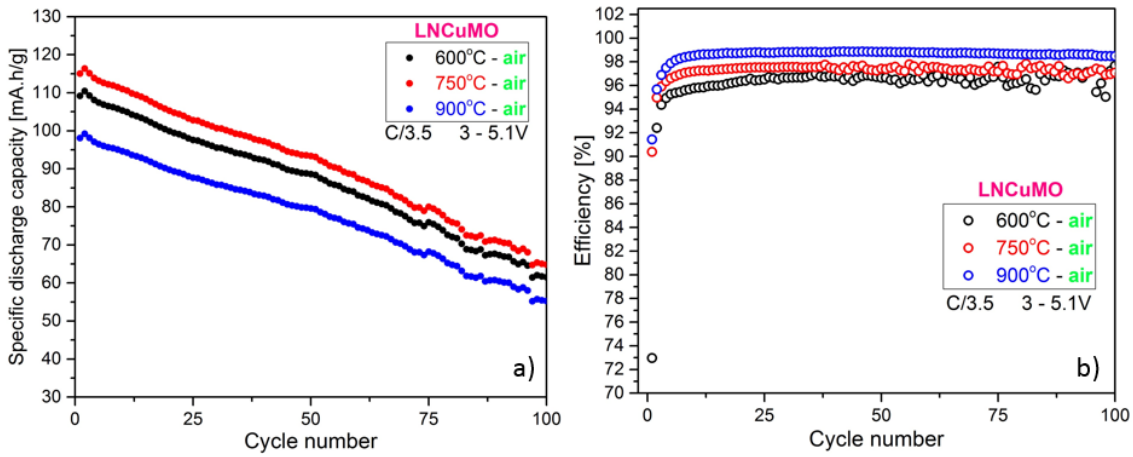

Figure 4.28 a) Specific discharge capacity vs. cycle number plots of cathode materials LNCuMO–600°C–air, LNCuMO–750°C–air and LNCuMO–900°C–air cycled at C / 3.5 rate between 3 – 5.1 V, b) Coulombic efficiency vs. cycle number plots for cycling mentioned in a)

4.2.2 Results of Annealed $LiNi_{0.25}Cu_{0.25}Mn_{1.5}O_4$ under O_2 Cathode Materials

In this study, the $LiNi_{0.25}Cu_{0.25}Mn_{1.5}O_4$ (LNCuMO) precursors obtained were annealed at different temperatures (600 °C, 750 °C and 900 °C) under O_2 which are denoted by LNCuMO–600°C–O_2, LNCuMO–750°C–O_2 and LNCuMO–900°C–O_2, respectively. Detailed discussions about the structural and the electrochemical characterization of the materials obtained will be given the following sections.

4.2.2.1 Structural Characterization

According to the Rietveld refinement of diffraction patterns of cathode materials LNCuMO–600°C–O_2, LNCuMO–750°C–O_2 and LNCuMO–900°C–O_2 (see Figure 4.29), in addition to the main phase which has cubic spinel structure, the samples include different ratios of CuO (2.1, 0.3 and 2.6 %, respectively). In addition to this, LNCuMO–750°C–O_2 and LNCuMO–900°C–O_2 cathode materials contain Li_2MnO_3 monoclinic impurity phase (respectively, 0.9 and 3.6 %).

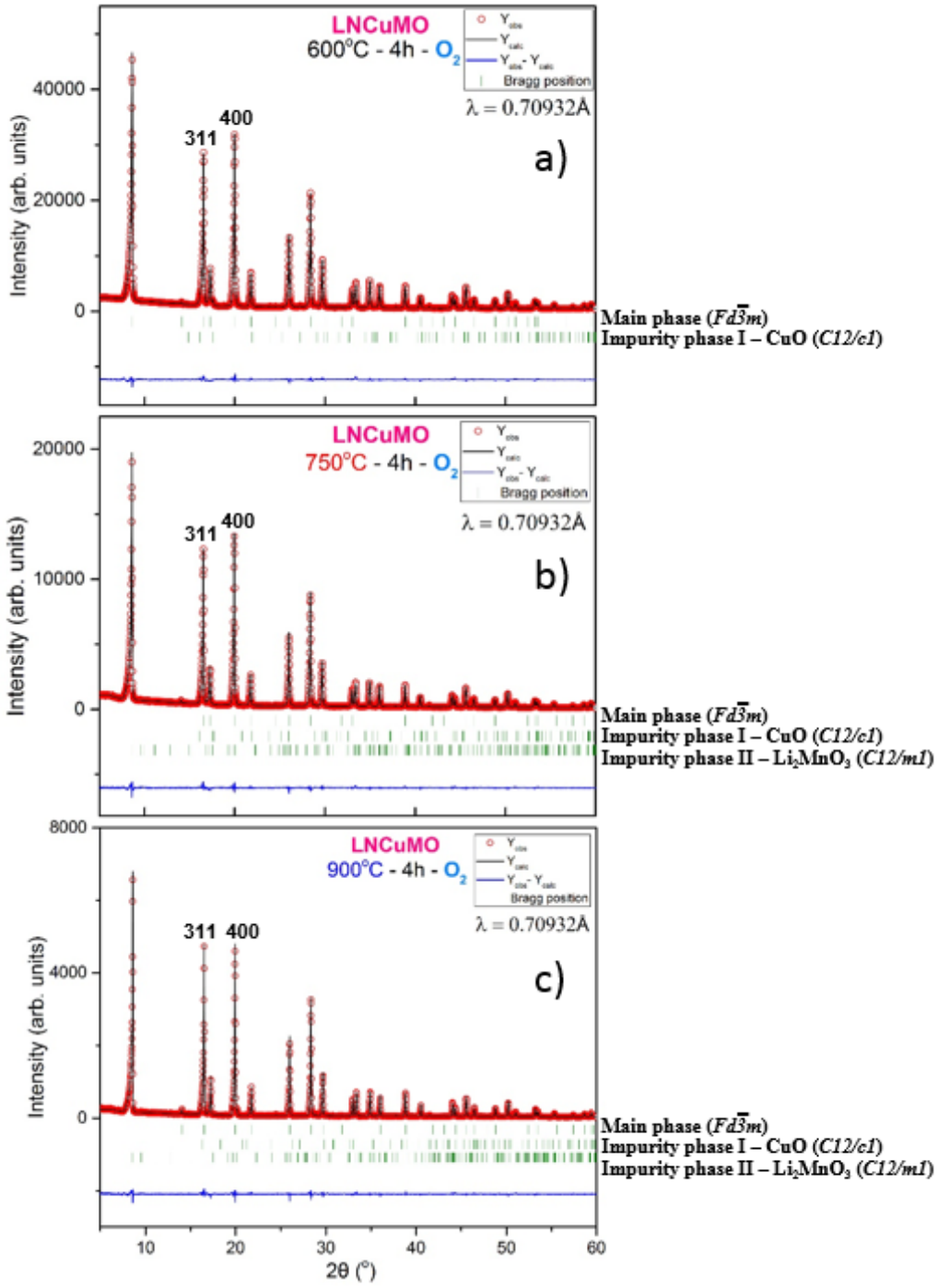

Figure 4.29 Rietveld refinement of diffraction patterns of as prepared cathode materials a) LNCuMO–600°C–O_2, b) LNCuMO–750°C–O_2 and c) LNCuMO–900°C–O_2 measured in 0.5 mm capillaries

The integrated intensity ratio of 400 / 311 reflections of the main phase decreases with increasing annealing temperature, which shows that the number of the transition metal ions on the tetrahedral site increases.

Table 4.8 Rietveld refinement results of LNCuMO–600°C–O_2, LNCuMO–750°C–O_2 and LNCuMO–900°C–O_2 samples

Annealing temperature of samples [^{o}C]	Atomic site	x=y=z	a [Å]	Volume [Å^3]	Fraction of impurity phase [%]	Cu on the tetrahedral site (8a) [%]	Overall temperature factor (B_{ov})	R_{wp} [%]
600	Li_{8a} Cu_{8a} Mn_{16d} Ni_{16d} Cu_{16d} Li_{16d} O_{32e}	0.125 0.125 0.500 0.500 0.500 0.500 0.2634(6)	8.1792(3)	547(3)	2.1	2.4	0.25	6.10
750	Li_{8a} Cu_{8a} Mn_{16d} Ni_{16d} Cu_{16d} Li_{16d} O_{32e}	0.125 0.125 0.500 0.500 0.500 0.500 0.2638(8)	8.1820(3)	548(3)	1.2	4.2	0.40	7.98
900	Li_{8a} Cu_{8a} Mn_{16d} Ni_{16d} Cu_{16d} Li_{16d} O_{32e}	0.125 0.125 0.500 0.500 0.500 0.500 0.2641(3)	8.1894(4)	549(4)	6.2	8.1	0.39	12.2

The additional details about the Rietveld refinement results of cathode materials LNCuMO–600°C–O_2, LNCuMO–750°C–O_2 and LNCuMO–900°C–O_2 are presented in Table 4.8. The lattice parameter of the spinel and the impurity phase amount in the samples increase with increasing annealing temperature.

4.2.2.2 Electrochemical Characterization

Figure 4.30 shows the voltage profile of the LNCuMO–600°C–O_2, LNCuMO–750°C–O_2 and LNCuMO–900°C–O_2 samples cycled at C / 3.5 charge – discharge rate between 3 – 5.1 V. The LNCuMO–600°C–O_2 has the highest specific discharge capacity of 1st discharge. The Mn^{3+} contents in the LNCuMO–600°C–O_2, LNCuMO–750°C–O_2 and LNCuMO–900°C–O_2 samples, which are calculated from the capacity obtained in 4 V region, are 0.169, 0.096 and 0.106 moles, respectively.

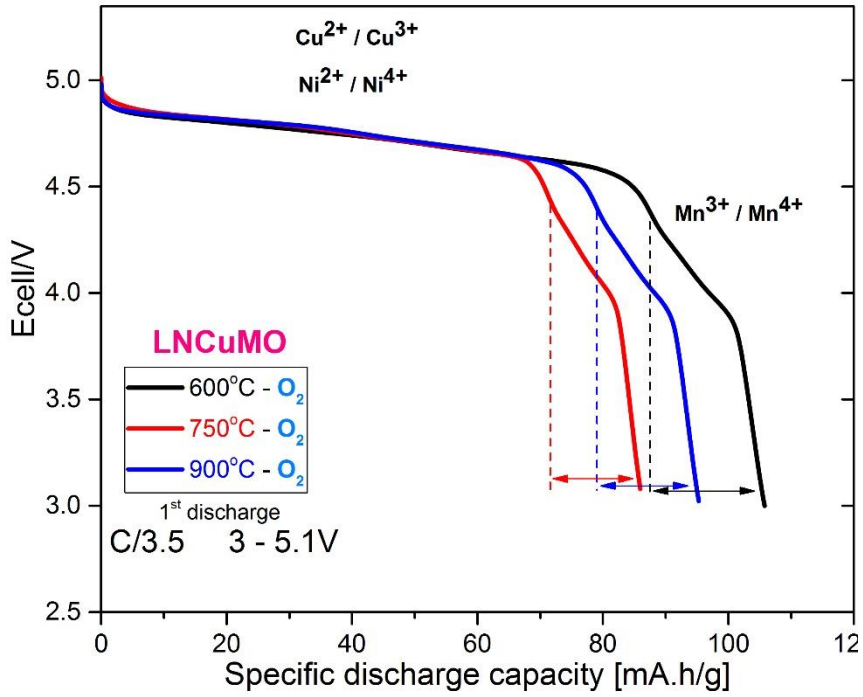

Figure 4.30 Cell voltage vs. specific discharge capacity of 1st discharge of cathode materials LNCuMO–600°C–O_2, LNCuMO–600°C–O_2 and LNCuMO–600°C–O_2

The cell voltage vs. Li content in the material curves of the LNCuMO–600°C–O_2, LNCuMO–750°C–O_2 and LNCuMO–900°C–O_2 samples cycled at C / 3.5 rate between 3 – 5.1 V for the 1st cycle are shown in Figure 4.31. At the end of the 1st cahrge, Li contents of the samples annealed at 600 °C, 750 °C and 900 °C are 0.10, 0.13 and 0.14. At the end of the 1st cycle, the ratios of the Li content fade from the samples are 17, 11 and 7 %, respectively.

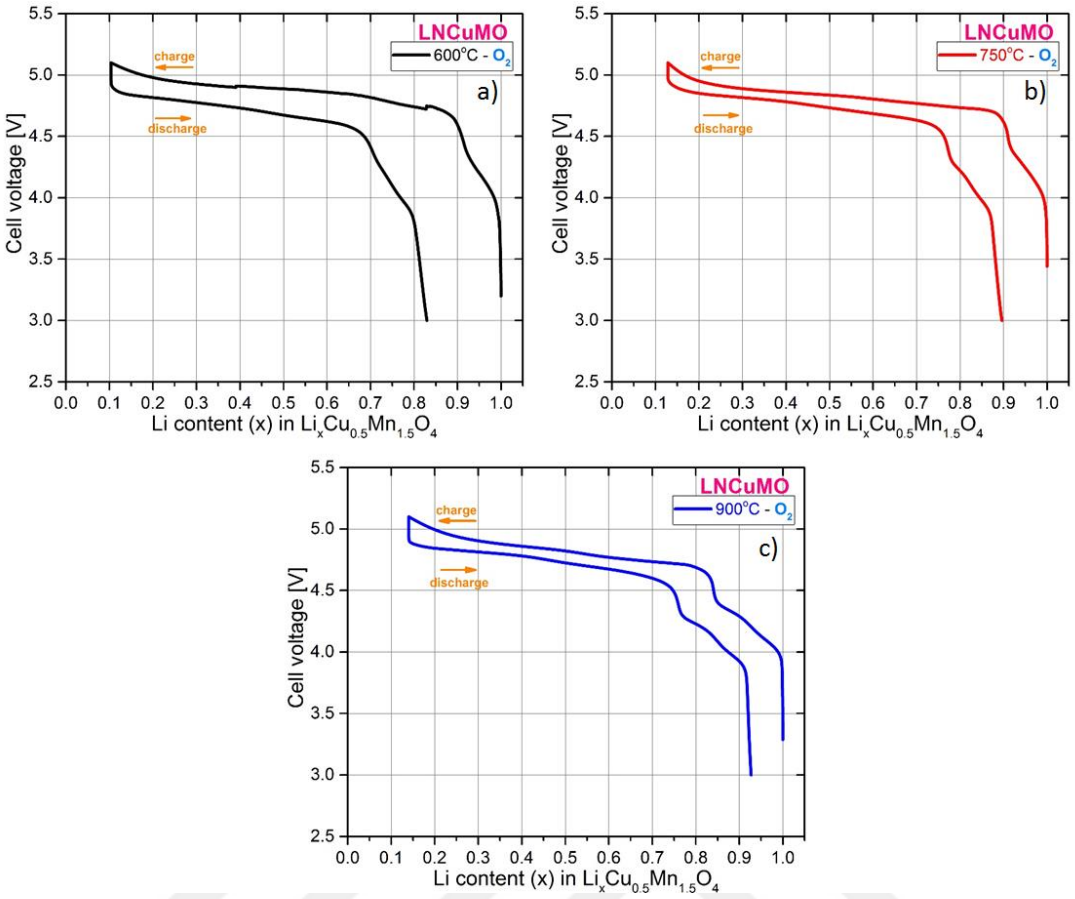

Figure 4.31 Cell voltage vs. Li content in the material curves of 1st cycle of as prepared a) LNCuMO–600°C–O_2, b) LNCuMO–750°C–O_2 and c) LNCuMO–900°C–O_2

Figure 4.32 a) shows the cycling stability results of the first 100 cycles of the LNCuMO–600°C–O_2, LNCuMO–750°C–O_2 and LNCuMO–900°C–O_2 samples. The capacity fading ratio for all three samples is 41.2 %.

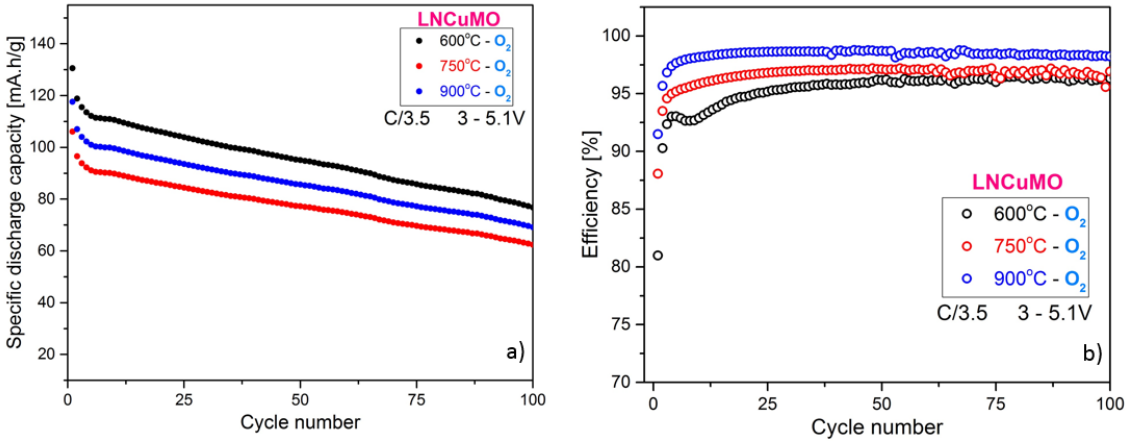

Figure 4.32 a) Specific discharge capacity vs. cycle number plots of cathode materials LNCuMO–600°C–O_2, LNCuMO–750°C–O_2 and LNCuMO–900°C–O_2 cycled at C / 3.5 rate between 3 – 5.1 V, b) Coulombic efficiency vs. cycle number plots for cycling mentioned in a)

Figure 4.32 b) shows that the LNCuMO–900°C–O_2 sample has the highest first coulombic effieciency. The coulombic efficiencies of LNCuMO–600°C–O_2, LNCuMO–750°C–O_2 and LNCuMO–900°C–O_2 samples increase and reach ~96.3, 96.9 and 98.2 %, respectively, during the following cycles.

4.2.3 Structural Characterization Studies on Annealed $LiNi_{0.25}Cu_{0.25}Mn_{1.5}O_4$ under Ar Cathode Materials

In this study, the $LiNi_{0.25}Cu_{0.25}Mn_{1.5}O_4$ (LNCuMO) precursors obtained were annealed at different temperatures which were 600 ^{o}C, 750 ^{o}C and 900 ^{o}C under Ar atmosphere.

XRD patterns of the LcuMO annealed at 600 ^{o}C, 750 ^{o}C and 900 ^{o}C for 4 h under Argon atmosphere cathode materials are shown in Figure 4.33 which involve the Bragg positions (as vertical green marks) of the main cubic phase, the first impurity phase Li_2MnO_3 and the second impurity phase CuO. The characteristic reflections of the main phase, which are emphasized in Figure 4.33, decrease and disappear with the increasing annealing temperature, hence, the Rietveld refinement analysis was performed only for the sample annealed at 600 ^{o}C (see Table 4.9 for additional details).

Table 4.9 Rietveld refinement result of the cathode material LNCuMO annealed at 600 ^{o}C for 4 h under Argon atmosphere

Annealing temperature of samples [^{o}C]	Atomic site	x=y=z	a [Å]	Volume [Å^3]	Fraction of impurity phase [%]	Cu on the tetrahedral site (8a) [%]	Overall temperature factor (B_{ov})	R_{wp} [%]
600	Li_{8a} Cu_{8a} Mn_{16d} Ni_{16d} Cu_{16d} Li_{16d} O_{32e}	0.125 0.125 0.500 0.500 0.500 0.500 0.2634(8)	8.2288(3)	557(3)	15.27	11.9	0.28	7.52

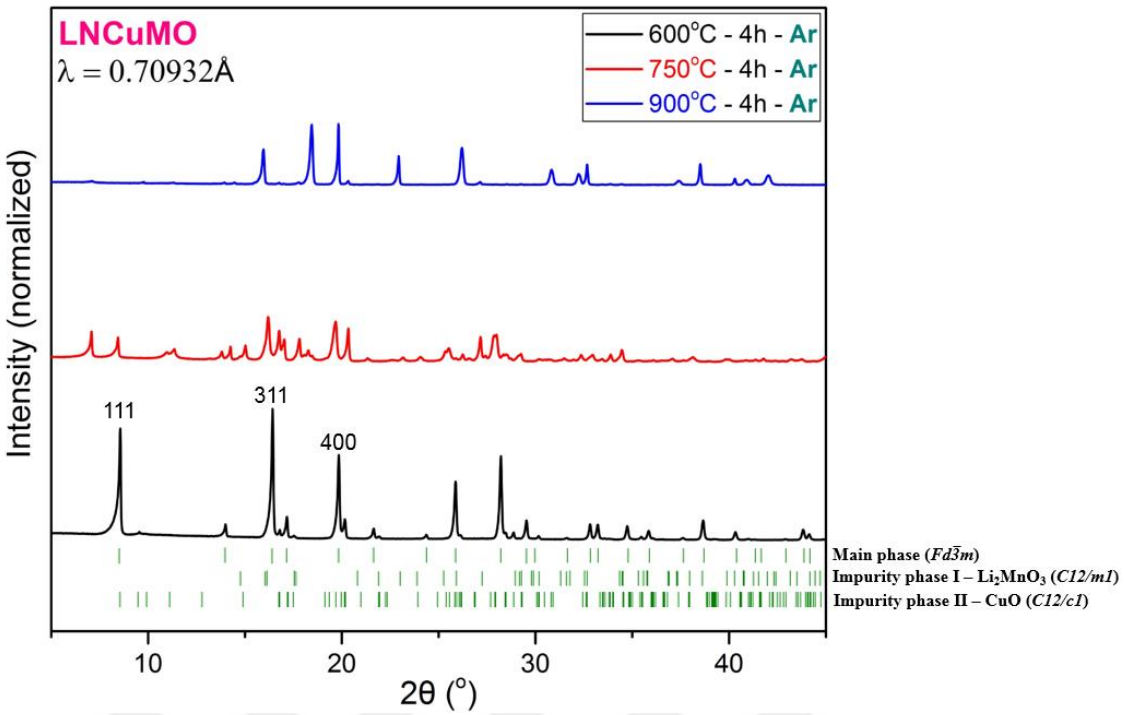

Figure 4.33 XRD patterns of the cathode materials LNCuMO annealed at 600 °C, 750 °C and 900 °C for 4 h under Argon atmosphere

CHAPTER 5

CONCLUSION

The aim of this work was the synthesis, characterization and study of the operation mechanism of high voltage $LiCu_{0.5}Mn_{1.5}O_4$ (LCuMO) and $LiNi_{0.25}Cu_{0.25}Mn_{1.5}O_4$ (LNCuMO) spinels as cathode materials for LIBs. These materials were successfully synthesized with a citric acid assisted Pechini sol – gel method. The obtained precursors were divided into eleven samples which were treated at different annealing temperature (600 ^{o}C, 750 ^{o}C and 900 ^{o}C), time and atmosphere (air, O_2 and Ar). ICP – OES analysis is in good agreement with the stoichiometric amounts of lithium, copper and manganese taken for the synthesis.

X – ray diffraction confirmed that all of the annealed LCuMO and LNCuMO in air and under O_2 samples have cubic spinel structure with $Fd\bar{3}m$ space group. The LCuMO and LNCuMO annealed at 600 ^{o}C under Ar atmosphere samples have also the same structure, but higher annealing temperature results in the decomposition of the spinel. In addition to that, depending on synthesis conditions, the samples contain different ratios of CuO and Li_2MnO_3 as impurities. The X – ray diffraction results revealed that the annealing temperature has a stronger influence on the phase purity than the annealing time.

^{7}Li MAS NMR inspections were performed for the LCuMO annealed at 600 ^{o}C in air sample and the results confirmed that the Cu ions were successfully incorporated into the spinel lattice of $LiMn_2O_4$.

SEM images revealed that the annealing time at 600 $^{\circ}$C has no impact on the particle size. However, the SEM images of the annealed LNCuMO in air showed that increasing the annealing temperature enlarges the particle size of the samples.

The results of XANES for the samples LCuMO annealed in air revealed that Cu and Mn in the samples predominantly exist as Cu^{2+} and Mn^{4+}.

Electrochemical characterization revealed activities at around 4 V and 5 V region for the samples LCuMO and LNCuMO annealed in air and under O_2, in the voltage range 3 – 5.1 V. The 4 V region activities were attributed to the Mn^{3+} / Mn^{4+} redox couple for all of these samples. For LCuMO samples, the 5 V region activities were attributed to the Cu^{2+} / Cu^{3+} redox couple. As for the LNCuMO samples, the 5 V region activities were related to Ni^{2+} / Ni^{4+} and Cu^{2+} / Cu^{3+} redox couples. The samples annealed in air atmosphere have batter capacity retention after 100 cycles at C / 3.5 (60.3 %) than all the other samples. The sample LCuMO annealed at 600 ^{o}C for 12 h in air has the highest amount of Mn^{3+} content in the material. Moreover, the coulombic efficiency increases with increasing annealing temperature.

In situ investigations for the sample LCuMO annealed at 600 ^{o}C for 4 h in air showed that the second Li intercalation plateau at around 3 V region during discharge process was associated with the two phase reaction. The cubic spinel structure transformed to the tetragonal structure in this plateau.

It can be concluded that the LCuMO high spinel cathode material is electrochemically more cycling stable than the LNCuMO high spinel cathode material.

REFERENCES

[1] Kızıltaş Yavuz, N., (2015). Influence of M – doping (M = Ru, Fe, La, Nd, Sm) on the Performance of Lithium Nickel – Manganese Spinels as High – Voltage Cathode Materials for Lithium Ion Batteries, PhD Thesis, Karlsruhe Institute of Technology – Faculty of Chemistry and Bioscience – Institute of Inorganic Chemistry, Karlsruhe.

[2] Bhaskar, A., Mikhailova, D., Kızıltaş – Yavuz, N., Nikolowski, K., Oswald, S., Bramnik, N.N. and Ehrenberg, H., (2014). "3d – Transition Metal Doped Spinels as High – Voltage Cathode Materials for Rechargable Lithium – Ion Batteries", Progress in Solid State Chemistry, 42:128-148.

[3] Linden, D. and Reddy, T.B., (2001). Handbook of Batteries, Third Edition, Mc Graw – Hill Book Co., New York.

[4] Zhang, Z. and Zhang, S.S., (2015). Rechargeable Batteries Materials, Technologies and New Trends, Springer, New York.

[5] Mizushima, K., Jones, P.C., Wiseman, P.J. and Goodenough, J.B., (1980). "Li_xCoO_2 ($0<x<-1$): A New Cathode Material for Batteries of High Energy Density", Materials Research Bulletin, 15(6):783-789.

[6] Deshpande, R.D., (2011). Understanding and Improving Lithium Ion Batteries Through Mathematical Modelling and Experiments, PhD Thesis, University of Kentucky – Chemical and Materials Engineering, Deshpande.

[7] Bhaskar, A., (2011). Investigations of $LiM_{0.5}Mn_{1.5}O_4$ (M = Fe, Co, Ni) Spinels as High – Volt Cathode Materials for Rechargeable Lithium – Ion Batteries, PhD Thesis, Technische Universität Darmstadt – Institute for Materials Science, Darmstadt.

[8] FIZ Karlsruhe, Neue Materialien für Lithium – Ionen – Batterien, http://images.google.de/imgres?imgurl=http%3A%2F%2Fforschung-energiespeicher.info%2Ffileadmin%2Fuser_upload%2Fprojektassets%2FKaLiPat%2FBMBF_5_KALIPAT_Nachwuchsgruppe_deu.jpg&imgrefurl=http%3A%2F%2Fforschung-energiespeicher.info%2Fbatterie-im-netz%2Fprojektliste%2Fprojekt-einzelansicht%2F104%2FNeue_Materialien_fuer_Lithium_Ionen_Batterien%2F&h=545&w=850&tbnid=92nB5ylNDdMTEM%3A&docid=KgCPqvcUD1Vc6M&ei=dYdeV4XHBourabf0hLAJ&tbm=isch&iact=rc&uact=3&page=1&start=0&ndsp=36&ved=0ahUKEwjF1aqz4qTNAhWLVRoKHTc6AZYQMwgeKAAwAA&bih=868&biw=1760, 10 May 2016.

[9] Bramnik, N.N., Nikolowski, K., Trots, D.M. and Ehrenberg, H., (2008). "Thermal Stability of $LiCMnoPO_4$ Cathodes", Electrochem. Solid – State Lett., 11:89-93.

[10] Ohzuku, T. and Ueda, A., (1994). "Solid – State Redox Reactions of $LiCoO_2$ ($R\bar{3}m$) for 4 Volt Secondary Lithium Cells", J. Electrochem. Soc., 141:2972-2977.

[11] Thackeray, M.M., (1999). "Spinel Electrodes for Lithium Batteries", J. Am. Ceram. Soc., 82(12):3347-3354.

[12] Erikson, T., (2001). $LiMn_2O_4$ as a Li – Ion Battery Cathode, PhD Thesis, Acta Universitatis Upsaliensis – Faculty of Science and Technology, Uppsala.

[13] Kızıltaş – Yavuz, N., (2011). "Investigation and Characterization of Functional Oxide Materials for High – Energy Li –Ion Batteries", Master Thesis, Leibniz Institute for Solid State and Materials Research Dresden (IFW), Dresden.

[14] Taniguchi, I., Lim, C.K., Song, D. and Wakihara, M., (2002). "Particle Morphology and Electrochemical Performances of Spinel $LiMn_2O_4$ Powders Synthesized Using Ultrasonic Spray Pyrolysis", Solid State Ionics, 146:293-247.

[15] Ein – Eli, Y., and Howard, W.F., (1997). "$LiCu_x^{II}Cu_y^{III}Mn_{[2-(x+y)]}^{III,IV}O_4$: 5 V Cathode Material", J. Electrochem. Soc., 144(8):205-207.

[16] Ein – Eli, Y., Lu, S.H., Rzeeznik, M.A., Vaughey, J.T. and Thackeray, M., (1998). "$LiCu_xMn_{2-x}O_4$ ($0.1 \leq x \leq 0.5$): A New Class of Cathode Metarials for Li Batteries", J. Electrochem. Soc., 145(10):3383-3386

[17] Ebin, B., Gürmen, S. and Lindbergh, G., (2012). "Electrochemical properties of Nanocrystalline $LiCu_xMn_{2-x}O_4$ (x = 0.2 – 0.6) Particles Prepared by Ultrasonic Spray Pyrolysis Method", Material Chemistry and Physics, 136:424-430.

[18] Caballero, A., Cruz, M., Hernan, L., Melero, M., Molares, J. and Castellon, E.R., (2005). "Oxygen Deficiency as the Origin of the Dispate Behavior of $LiM_{0.5}Mn_{1.5}O_4$ (M = Ni, Cu) Nanospinels in Lithium Cells", Journal of THE Electrochemical Soc., 152(3):552-559.

[19] Ein – Eli, Y., Vaughey, J.T., Thackeray, M.M., Mukerjee, S., Yang, X.Q. and McBreen J. (1999). "$LiNi_xCu_{0.5-x}Mn_{1.5}O_4$ Spinel Electrodes, Superior High – Potential Cathode Materials for Li Batteries", Journal of the Electrochemical Society, 146(3):908-913.

[20] Milewska, A., Kondracki, L., Molenda, M., Bakierska, M. and Molenda, J., (2014). "Structural, Transport and Electrochemical Properties of $LiNi_{0.5-y}Cu_yMn_{1.5}O_{4-\delta}$ Spinel Cathode Materials", Solid State Ionics, 267:27-31.

[21] Liu, W., Farrington, G.C., Chaput, F. and Dunn, B., (1996). "Synthesis and Electrochemical Studies of Spinel Phase $LiMn_2O_4$ Cathode Materials Prepared by the Pechini Process", J. Electrochem. Soc., 143(3):879-884.

[22] Ermrich, M. and Detlef, O., (2011). X – Ray Powder Diffraction, PANalytical, Kassel.

[23] Ravel, B. and Newville, M., (2005). "Athene, Artemis, Hephaestus: Data Analysis for X – ray Absorption Spectroscopy Using IFEFFIT", Journal of Synchrotron Radiation, 12(4):537-541.

[24] Dixon, D., (2012). Spatially Resovled Studies in Direct Methanol Fuel Cells, PhD Thesis, Teschische Universität Darmstadt – Institute of Materials Science, Darmstadt.

[25] Arun, N., Aravindan, V., Jayaraman, S. and Madhavi, S., (2015). "Unveiling the Fabrication of `Rocking Chair` Type 3.2 and 1.2 V Class Cells Using Spinel $LiNi_{0.5}Mn_{1.5}O_4$ as Cathode with $Li_4Ti_5O_{12}$", J. Phys. Chem. C., 119(43):24332-24336.

CURRICULUM VITAE

PERSONAL INFORMATION

Name Surname : Öznil BUDAK

Date of birth and place : 05.07.1989 – Tekirdağ / Turkey

Foreign Languages : English, German

E-mail : oznilbudak@gmail.com

EDUCATION

Degree	**Department**	**University**	**Date of Graduation**
MSc.	Chemical Engineering	Yıldız Technical University	2016
Undergraduate	Chemical Engineering	Yıldız Technical University	2013
High School	Science – Mathematics	Kepirtepe Teachers Training High School	2007

WORK EXPERIENCE

Year	Corporation/Institute	Enrollment
2015 – 2016	Karlsruhe Institute of Technology Institute of Applied Materials – Energy Storage Systems (IAM-ESS)	Student assistant
2013 – 2014	Chamber of Chemical Engineering	Consultancy
2007 – 2008	Olimpiyat Computer Industrial Corporation	Sales consultant

PUBLISHMENT

Conference Paper

1. Budak, Ö., Bramnik, N., Bhaskar, A., Kızıltaş Yavuz, N., Ehrenberg, H. and Knapp, M., (2016). "$LiCu_{0.5}Mn_{1.5}O_4$ and $LiNi_{0.25}Cu_{0.25}Mn_{1.5}O_4$ Spinel Electrodes for Li-ion Batteries", 24th Annual Meeting of German Crystallographic Society Conference, 14-17 March 2016, Stuttgart.

Project

1. Defect Spinels as high – energy and performance materials for electrochemical energy storage (DESIREE), (2016). Federal Ministry of Education and Research, 03SF0477B, Karlsruhe.
2. Hydrogen Production from H_2S Decomposition in Micro – structured Proton – Conducting Solid Oxide Membrane Reators, (2015). BS – ERA.NET – TUBITAK-MAG, BS – ERA.NET:0.28 – 111M801, Istanbul.